INFORMATION TO USERS

This manuscript has been reproduced from the microfilm master. UMI films the text directly from the original or copy submitted. Thus, some thesis and dissertation copies are in typewriter face, while others may be from any type of computer printer.

The quality of this reproduction is dependent upon the quality of the copy submitted. Broken or indistinct print, colored or poor quality illustrations and photographs, print bleedthrough, substandard margins, and improper alignment can adversely affect reproduction.

In the unlikely event that the author did not send UMI a complete manuscript and there are missing pages, these will be noted. Also, if unauthorized copyright material had to be removed, a note will indicate the deletion.

Oversize materials (e.g., maps, drawings, charts) are reproduced by sectioning the original, beginning at the upper left-hand corner and continuing from left to right in equal sections with small overlaps. Each original is also photographed in one exposure and is included in reduced form at the back of the book.

Photographs included in the original manuscript have been reproduced xerographically in this copy. Higher quality 6" x 9" black and white photographic prints are available for any photographs or illustrations appearing in this copy for an additional charge. Contact UMI directly to order.

UMI

A Bell & Howell Information Company
300 North Zeeb Road, Ann Arbor, MI 48106-1346 USA
313/761-4700 800/521-0600

UMI Number: 9525739

UMI
300 North Zeeb Road
Ann Arbor, MI 48103

THEORY, DESIGN AND APPLICATIONS OF LINEAR TRANSFORMS FOR INFORMATION TRANSMISSION

by
Adil Benyassine

A Dissertation
Submitted to the Faculty of
New Jersey Institute of Technology
in Partial Fulfillment of the Requirements for the Degree of
Doctor of Philosophy

Department of Electrical and Computer Engineering

January 1995

ABSTRACT

THEORY, DESIGN AND APPLICATIONS OF LINEAR TRANSFORMS FOR INFORMATION TRANSMISSION

by
Adil Benyassine

The aim of this dissertation is to study the common features of block transforms, subband filter banks, and wavelets, and demonstrate how discrete uncertainty can be applied to evaluate these different decomposition techniques. In particular, we derive an uncertainty bound for discrete-time functions. It is shown that this bound is the same as that for continuous-time functions, if the discrete-time functions have a certain degree of regularity.

This dissertation also deals with spectral modeling in filter banks. It is shown, both theoretically and experimentally, that subspectral modeling is superior to full spectrum modeling if performed before the rate change. The price paid for this performance improvement is an increase of computations. A few different signal sources were considered in this study. It is shown that the performances of AR and ARMA modeling techniques are comparable in subspectral modeling. The first is desired because of its simplicity. As an application of AR modeling, a coding algorithm of speech, namely CELP embedded in a filter bank structure was also studied. We found that there were no improvements of subband CELP technique over the full band one. The theoretical reasonings of the experimental results are also given.

This dissertation also addresses the problems of what type of transform to be used and to what extent an image should be decomposed. To this aim, an objective and subjective evaluations of different transform bases were done.

We propose a smart algorithm for the decomposition of a channel into its sub-channels in the discrete multitone communications. This algorithm evaluates the unevenness and energy distribution of the channel spectrum in order to get its variable adaptive partitioning. It is shown that the proposed algorithm leads to a near optimal performance of the discrete multitone transceiver. This flexible splitting of the channel suffers less from the aliasing problem that exists in blind decompositions using fixed transforms. This dissertation extends the discrete multitone to the flexible multiband concept which brings significant performance improvements for digital communications.

APPROVAL PAGE

THEORY, DESIGN AND APPLICATIONS OF LINEAR TRANSFORMS FOR INFORMATION TRANSMISSION

Adil Benyassine

Dr. Ali N. Akansu, Dissertation Advisor — Date
Associate Professor of Electrical
and Computer Engineering, NJIT

Dr. Alexander Haimovich, Committee Member — Date
Associate Professor of Electrical
and Computer Engineering, NJIT

Dr. Zoran Siveski, Committee Member — Date
Assistant Professor of Electrical
and Computer Engineering, NJIT

Dr. Dennis Karvelas, Committee Member — Date
Assistant Professor of Computer Science
and Computer Engineering, NJIT

Dr. Russell Hsing, Committee Member — Date
District Research Manager, Bellcore, Morristown, NJ

BIOGRAPHICAL SKETCH

Author: Adil Benyassine

Degree: Doctor of Philosophy

Date: January 1995

Undergraduate and Graduate Education:

- Doctor of Philosophy in Electrical Engineering,
  New Jersey Institute of Technology, Newark, NJ, 1995
- Master of Science in Electrical Engineering,
  San Diego State University, San Diego, CA, 1991
- Bachelor of Science in Electrical Engineering,
  University of Texas at Austin, Austin, TX, 1987

Major: Electrical Engineering

Presentations and Publications:

A. Benyassine and A.N. Akansu, "Subspectral Modeling in Filter Banks," NJIT Symposium on Applications of Subbands and Wavelets, March 1994, Newark, NJ.

A. Benyassine and A.N. Akansu, "Evaluation of M-band Orthonormal Filter Banks: Hierarchical and Direct Structures," Visual Communications and Image Processing, Cambridge, MA., November 1993.

R.A. Haddad, A.N. Akansu and A. Benyassine, "Time Frequency Localizations in Transforms, Subbands and Wavelets: A Critical Review," Optical Engineering, July 1993.

This work is dedicated to
my family

ACKNOWLEDGMENT

I would like to express my deepest gratitude to Professor Ali Akansu, who not only served as my research advisor, constantly providing invaluable insights and intuitions, but also gave me support, encouragement, reassurance and help. Professor Akansu was more than an advisor and professor. He was like an older brother. Thanks a lot Ali. Very special thanks go to my labmates: Mehmet Tazebay, Nadir Sezgin, Dr. Raafat Kamel, and Michael Meyer, for their help and companionship.
I would like also to extend my thanks to Professor Alex Haimovich, Professor Zoran Siveski, Professor Dennis Karvelas, and Dr. Russell Hsing for taking some of their valuable time to read and to serve in my doctoral committee. My gratitude also goes to Brenda Walker and Lisa Fitton. I am deeply thankful to Professor Huseyin Abut of San Diego State University. He was very instrumental in introducing me to Professor Akansu. I am also grateful to Dr. Irving Kalet of AT &T Bell Labs. and Professor S.U. Pillai of Polytechnic University for their fruitful discussions. Last, but not least, I would like to thank my wonderful parents, my brothers, my sister, and my wife for their strong support, love and patience.

TABLE OF CONTENTS

Chapter Page

LIST OF TABLES

LIST OF FIGURES

Figure **Page**

CHAPTER 1

INTRODUCTION

In the last two decades, there has been an ever increasing demand for more information processing ability, larger storage capacity, and faster information transmission capabilities. This phenomenon had impacted the research community so much that a flurry of research activities was dedicated to novel signal representations, compression algorithms, and new standards for speech, image, and video coding.

Most of the new compression technologies and signal representation techniques make use of linear transforms. The popular transformations can be clustered into four main groups: block, overlapping block, subband, and more recently wavelet transforms. The first type involves mainly the Fourier transform and its extensions that have historically been the prime tool for signal representation. Since the early 1970's, the discrete cosine transform (DCT) emerged as a new block transform with real basis functions and good image coding performance. All of the current standard visual compression algorithms such as H.261, JPEG, MPEG I, and MPEG II incorporate the DCT as their signal decomposition tool. At very low bit rates, the coding performance of block transforms degrades significantly. This is due to the blockiness which results from independent coding of each sub-block and manifests itself as undesirable discontinuities at the boundaries. As a remedy to this annoying effect, lapped orthogonal transform (LOT) was proposed. This alternative transform to the fixed block ones, uses overlapping blocks to smooth out the discontinuities at the sub-block borders. The third widely used transform tool is the subband or filter banks . This transform removes the restrictions imposed on the durations of its basis functions which exists in the two previously cited transforms. Therefore, a better frequency tuning of the basis functions is possible within this category of transforms. Recently, the wavelet transform has been suggested as a new mathematical tool for signal representation of continuous-time signals at flexible time and frequency resolutions. The advantages of wavelet transform over the classical Fourier transform and short-time Fourier transform (STFT) were shown. The linkages and commonalities of the wavelet transform and discrete-time filter banks were also studied.

The time-frequency shaping of a basis set is of particular interest in practice. The trade-offs of the time and frequency domain behaviors have been well known for a single function. But, now the concept is extended to do time-frequency shaping of a set of functions which must be complete. While bandwidth compression of a signal, such as an image, requires transform operators with good frequency localization, spatial features such as edge preservation demand a high degree of localization in the time domain. These requirements compete with each other and one is secured at the expense of the other. The classical uncertainty principle in the continuous-time domain provides the back drop for this trade-off. The main thrust of this work is to study the common features of block transforms, subband filter banks, and wavelets, and demonstrate how discrete uncertainty can be applied to evaluate these different decomposition techniques. In particular, we evaluate the trade-off between localization in time and frequency for several proposed signal decomposition structures. Block transforms have the best localization in time as expected since they have the shortest duration functions. On the other hand, they exhibit the worst localization in frequency as predicted by the uncertainty principle. Filter bank structures have sharper frequency responses and their frequency spreads decreases at the expense of an increase in their time localizations due to their longer basis functions. Since the filter banks come in two flavors, direct and hierarchical, their products of the time and frequency spreads can be monitored depending on the structure used. We found that direct structures offer the best time-frequency spread product followed by hierarchical ones with the fixed block transforms trailing at the end. We also extended the original uncertainty principle in the analog domain to its discrete counterpart. In addition, we present several applications that make use of these popular linear transform techniques. In fact, the recent advances in the generalized linear transform (GLT) theory have opened new avenues for the joint treatment of the signal decomposition, spectral analysis and modeling problems. Among these applications, we used the subband transforms in subspectral source modeling, subband linear predictive coding (LPC) of speech, subband image coding, and finally the discrete multitone transceivers (DMT). In subspectral modeling application, a thorough analysis of the effects of multirate building blocks was done along with an assessment of the merits of subspectral modeling over conventional modeling techniques. We showed that subspectral modeling is superior to full spectrum modeling if performed before the rate change. The price paid for this performance improvement is an increase of computations. As an application of subspectral modeling, we studied the performance of an analysis-by-synthesis speech coder namely CELP in both a full band and subband environments. We found that there were no improvements of subband CELP technique over the full band one. The theoretical reasonings of the experimental results are also given in the thesis. We also studied the performance of the different subband structures as decomposition tools for an image codec. We observed that the hierarchical subband schemes outperform the direct structures in image coding. It is also shown that the dyadic tree subband codec outperforms the full-tree case for the image coding experiments performed in this study. As the last application, discrete multitone transceivers were evaluated using different basis functions as their modulator/demodulators. For this application, we proposed a smart technique for the partitioning of the channel into its sub-channels. This technique calls for a judicious selection of the basis functions for the modulation/demodulation functioning blocks. We also derived a distortion measure for the evaluation of the discrete multitone transceivers.

This dissertation is organized as follows. In Chapter 2, we start with the review of the fundamentals of multirate systems. We, then, link the theory of perfect reconstruction filter bank with that of the wavelet transform. We also give a design example of a multiplierless M-band PR filter bank. In Chapter 3, we address the concept of time-frequency localizations in linear transform. We give a proof on a lower bound of the discrete-time uncertainty principle. Chapter 4 gives a thorough analysis of the subspectral modeling. It is shown that there is a performance improvement in modeling subspectra of the signal over the full spectrum. A coding algorithm of speech namely CELP embedded in a filter bank structure was also studied. Following this, in Chapter 5, objective and subjective evaluations of different transform basis were done. Last, in Chapter 6, we address the implementation issues pertaining to the discrete multitone (DMT) transceivers.

CHAPTER 2

LINEAR TRANSFORMS

The goal of any aforementioned transforms is not only to represent a signal into its constituents, but also to decompose its correlated samples into a set of uncorrelated spectral coefficients in a compact fashion. In other words, these transformations should be able to concentrate the total energy of the signal in as few spectral coefficients as possible, if compression is the application at hand for example. Any of those transforms should satisfy certain characteristics depending on the application under consideration.

The block transforms, lapped orthogonal transforms(LOT) and filter banks are the most popular members of the linear transforms family employed in signal processing and related engineering applications[2]. It is commonly agreed that these once competing signal decomposition techniques are actually the variations of the same theory. The block transforms use the minimum possible time duration in their bases functions. On the other hand, the conventional LOT basis doubles the duration. The filter banks, in general, use arbitrary duration functions in their basis. The duality property of the time-frequency analysis defines the trade-offs of different bases with respect to their time and frequency domain characteristics. The block and overlapping linear transform theories, therefore, provide the foundations of orthonormal basis design for the applications considered. Additionally, the optimal filter bank concept has been forwarded lately to design the overlapping orthonormal sets based on the given criteria which is the extensions of optimal block transform, Karhunen-Loeve Transform(KLT).

2.1 Theory of Block and Lapped Transforms

Suppose we have a signal $x(n)$, $0 \leq n \leq N-1$. This signal can be easily expanded as a linear combination of a set of sequences $\{\phi_k(n)\}$ as

$$x(n) = \sum_{k=0}^{N-1} \theta_k \phi_k(n), \qquad 0 \leq n \leq N-1 \tag{2.1}$$

where $\{\theta_k\}$ are termed the spectral components of $x(n)$. On the other hand, we can obtain the coefficients as

$$\theta_s = \sum_{n=0}^{N-1} x(n)\phi_s^*(n), \qquad 0 \leq s \leq N-1 \tag{2.2}$$

The basis functions $\{\phi_k(n)\}$ has to satisfy the orthonormality, i.e.

$$\sum_{n=0}^{N-1} \phi_r(n)\phi_s^*(n) = \delta_{r-s} \tag{2.3}$$

where δ is the Dirac delta.

The basis $\{\phi_k(n)\}$ can be lumped together as a matrix Φ that satisfies the unitary condition

$$\Phi^{-1} = (\Phi^*)^T = \Phi^H \tag{2.4}$$

such that

$$\Phi\Phi^H = I \tag{2.5}$$

As an example of the Φ matrix, there is the DFT matrix. It consists of a set of orthogonal complex sinusoids namely

$$\phi_k(n) = e^{\frac{-j2\pi nk}{N}} \qquad k, n = 0, 1, 2, \cdot, N-1 \tag{2.6}$$

The corresponding transform matrix is therefore given as

$$\Phi = \left[W^{-nk}\right] \tag{2.7}$$

where $W = e^{\frac{-j2\pi}{N}}$. The inverse DFT (IDFT) matrix is given by Φ^* scaled by $\frac{1}{N}$ in order to satisfy the orthonormality condition. A second example is the well known discrete cosine transform (DCT). DCT, as alluded to in the beginning, is virtually the industry standard in image and speech transform coding because of its superior coding performance and the availability of its fast implementable realizations. The DCT basis functions are defined as

$$\begin{aligned} \Phi(r,n) = \Phi_r(n) &= (\frac{1}{c_r}) cos \frac{(2n+1)r\pi}{2N}, \; 0 \leq n, r \leq N-1 \\ c_r &= \begin{cases} \sqrt{N}, & r = 0 \\ \sqrt{N/2}, & r \neq 0 \end{cases} \end{aligned} \tag{2.8}$$

Both of these are called block transforms since they operate on a segment of samples at a time. This kind of transform offers good coding results at low and medium bit rate for both image and speech. However, their performance tends to degrade significantly at very low bit rates, causing a blocking effect as a result of independent coding of each sub-block.

Casserrau et al.[9] came up with an overlapping block transform called the Lapped Orthogonal Transform (LOT) which uses pixels in adjacent blocks to alleviate the blocking effects. Malvar and Staelin[27] proposed a new LOT structure that utilizes the basis functions of DCT for computational efficiency. Akansu and Wadas[5] extended the concept of efficient LOT by using other block transforms in the design of LOT bases.

Let $\{\underline{X}_0, \underline{X}_1, \cdots\cdots\cdots, \underline{X}_i, \cdots\cdots\cdots\}$ represent vectors of N contiguous samples each. We form a new vector $\underline{Y}_i$ of length $L > N$ obtained by extending the vector $\underline{X}_i$ from both the left and right sides by crossing over to borrow $\frac{N}{2}$ samples from $\underline{X}_{i-1}$ and $\underline{X}_{i+1}$ blocks respectively. The transform produces

$$\underline{\theta_i} = \underline{\Phi Y_i} \tag{2.9}$$

where $\underline{\theta_i}$ is $N \times 1$, Φ is $N \times L$, and $\underline{Y_i}$ is $L \times 1$. In this case the Φ matrix is no longer square and consequently it should obey different rules from its block counterpart in order to get perfect reconstruction. The basis functions $\{\phi_k(n)\}$ are now $1 \times L$ long.

They should satisfy the following requirements for perfect reconstruction (PR) [2]

$$\sum_k \phi_r(k)\phi_s(k+2n) = \delta(r-s)\delta(n) \tag{2.10}$$

2.2 Theory of Subband Filter Banks

The purpose of a filter bank is to decompose a signal spectrum into non-overlapping frequency bands before any further processing. This technique offers the advantage of allocating bits separately to each subband according to some perceptual criteria that are pertinent to that band for example in speech coding application.

2.2.1 Decimation and Interpolation in Multirate Filter Banks

The most basic operations taking place in a multirate signal processing are the decimation and interpolation. These two processing tools alter the clock rate at various points of the multirate system.

2.2.1.1 Decimation

The full spectrum signal occupying a bandwidth W is first filtered by an anti-aliasing filter (e.g. lowpass, bandpass, or highpass). If the resulting signal occupies a bandwidth $\frac{W}{M}$, we can throw away every other M samples of this new signal without loss of information in order to meet the Nyquist criterion[2][40]. What this criterion calls for is that any signal occupying a bandwidth W, only $2W$ samples per second are necessary to represent the signal perfectly. The process of filtering followed by the proper downsampling is called decimation in time. Fig. 2.1 shows such an operation. We can relate the signals at various points of the decimation process as

$$\begin{aligned} y(n) &= x(Mn) \quad &(2.11)\\ y(n) &= \sum_k h(Mn-k)u(k) \quad &(2.12) \end{aligned}$$

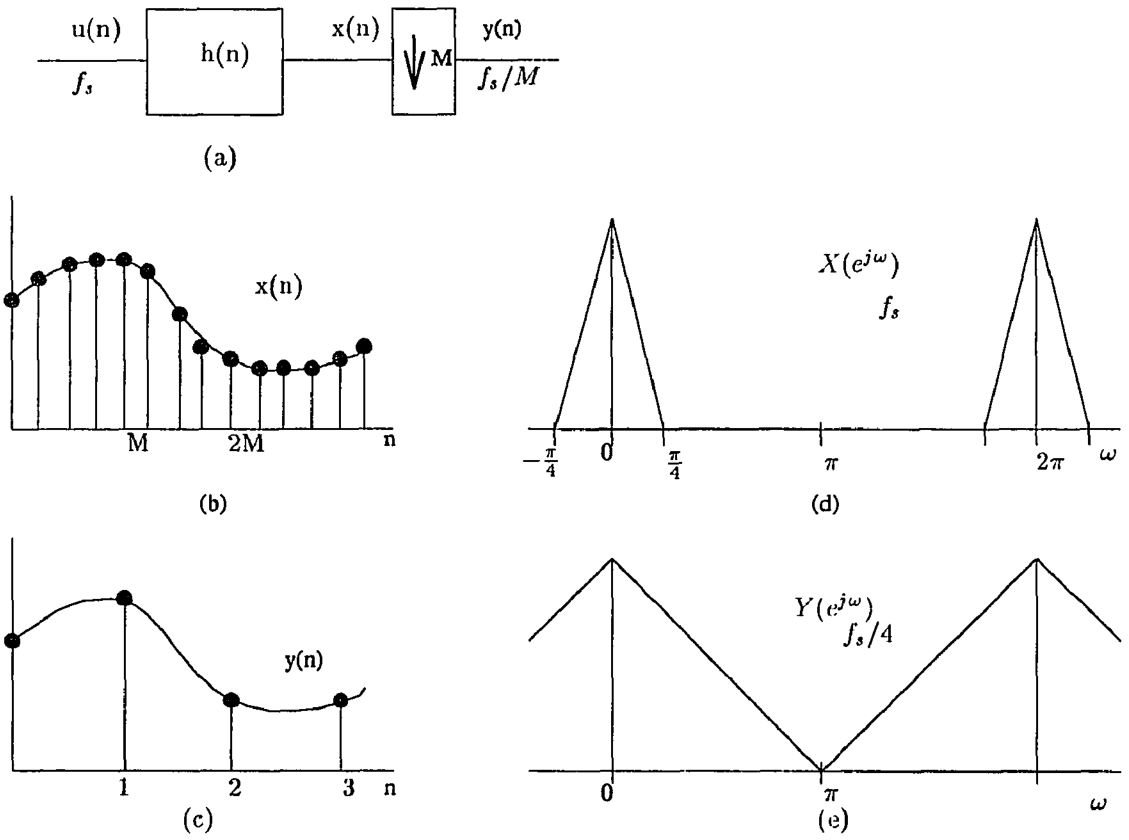

Figure 2.1 The decimation operation: (a) composite filter and downsampler, (b) filtered signal at fast clock rate, (c) downsampled signal at slow clock rate, (d) signal spectrum occupying $\frac{1}{4}$ of full band at fast clock rate f_s, (e) spectrum of signal downsampled by 4, occupies full band at $f_s/4$ clock rate

Clearly, decimation compresses the signal in time. This effect translates obviously into an expansion in the frequency domain. In fact, by taking the Z-transform of Eq. (2.11), it can be shown that[2][40]

$$Y(z) = \frac{1}{M}\sum_{k=0}^{M-1} X(z^{1/M}W^k), \qquad W = e^{-j2\pi/M} \tag{2.13}$$

or

$$Y(e^{j\omega}) = \frac{1}{M}\sum_{k=0}^{M-1} X(e^{j(\frac{\omega-2\pi k}{M})}) \tag{2.14}$$

Fig. 2.1 illustrates these two competing phenomena for the decimation case.

2.2.1.2 Interpolation

The counterpart of decimation is interpolation. This operation has the purpose of increasing the sampling rate of a signal by M. This is achieved by upsampling the signal by M through the insertion of M-1 zeros between the samples of the original signal and passing the obtained signal through an interpolation filter. The upsampling operation stretches the time axis and thus is accompanied by a compression of the signal in the frequency domain. This phenomenon translates into the introduction of high frequency components to the signal. These components are called imaging effects. The purpose of the interpolation filter is therefore to remove these high frequency components by smoothing the expanded signals. Fig. 2.2 depicts the interpolation operation. Likewise, we can relate the signals at various points of the interpolation process as

$$y(n) = \begin{cases} x(n/M), & n = 0, \pm M, \pm 2M, ... \\ 0, & otherwise \end{cases} \tag{2.15}$$

2.2.2 Polyphase Representation of a Filter

Polyphase representation of a filter is an efficient technique that finds a lot of applications in multirate systems. Let $H(z)$ be a filter such as

$$\begin{aligned} H(z) &= \sum_{k=0}^{N'-1} h(k) z^{-k} \\ &= h(0) + h(1)z^{-1} + \cdot + h(N'-1)z^{(N'-1)} \end{aligned} \tag{2.16}$$

where N' is the number of taps. $H(z)$ can be recast in a polyphase representation as

$$\begin{aligned} H(z) = & \sum_{k=0}^{N'-1} h(kM) z^{-kM} \\ & + z^{-1} \sum_{k=0}^{N'-1} h(kM+1) z^{-kM} \\ & \vdots \\ & + z^{-(M-1)} \sum_{k=0}^{N'-1} h(kM+M-1) z^{-kM} \end{aligned} \tag{2.17}$$

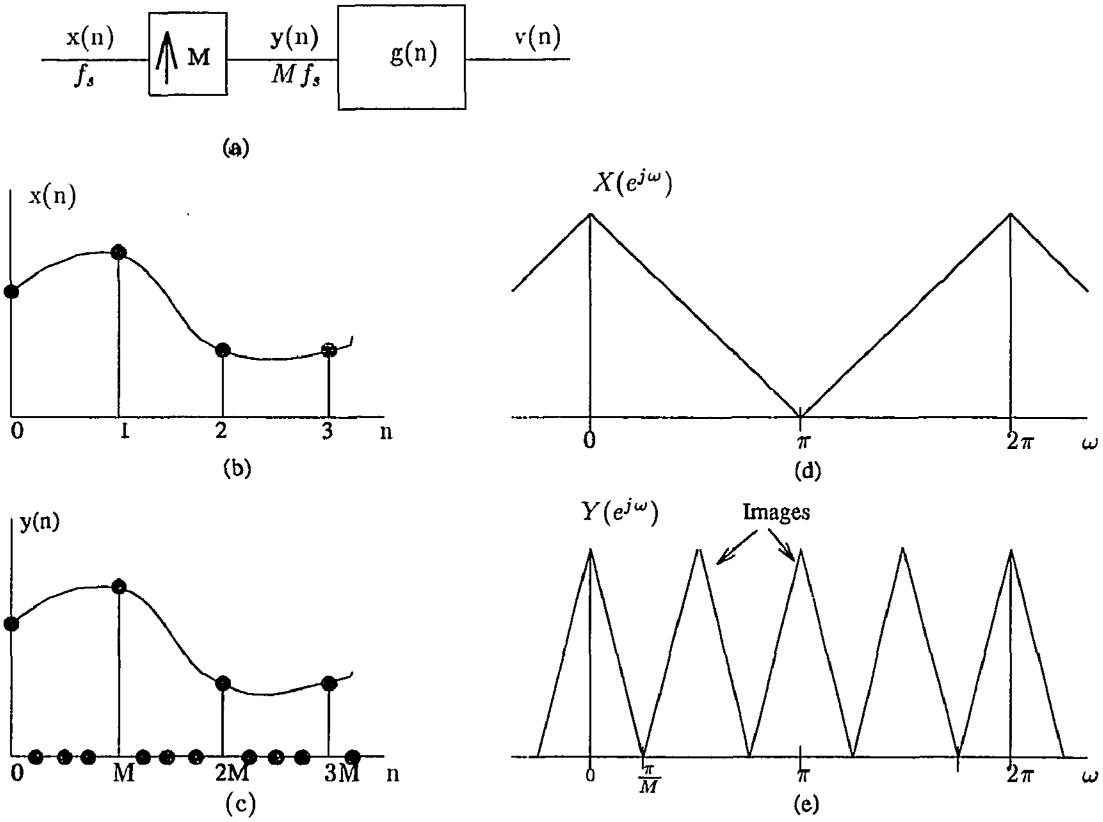

Figure 2.2 The interpolation operation: (a) composite upsampler and filter, (b) and (d) input to upsampler, time and frequency domains, (c) and (e) upsampler output, time and frequency domains for M=4.

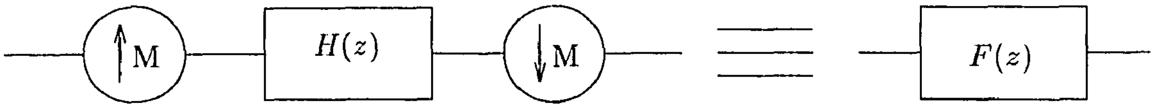

Figure 2.3 A cascade operation and its equivalent representation

where M is any integer. This representation can be compactly written as

$$H(z) = \sum_{l=0}^{M-1} z^{-l} E_l(z^M) \tag{2.18}$$

where

$$E_l(z) = \sum_{k=0}^{N'-1} e_l(k) z^k \tag{2.19}$$

with

$$e_l(k) = h(kM + l), \qquad 0 \le l \le M - 1 \tag{2.20}$$

When an upsampler is followed by a filter $H(z)$ and a downsampler as shown in Fig. 2.3, we can replace this structure by a simple filter $F(z)$. Notice that $F(z)$ is nothing else but the 0^{th} polyphase component of $H(z)$ as given by

$$f(k) = e_0(k) = h(kM), \qquad 0 \le k \le N' - 1 \tag{2.21}$$

2.2.3 The Two-Band and M-Band Subband Transforms

Now, that we have laid out the foundations of multirate operations, we will analyze a generic two-band perfect reconstruction (PR) filter bank as shown in Fig. 2.4. The input signal $x(n)$ occupying a bandwidth from 0 to π is divided into two equal subbands. The analysis filters $H_1(z)$ and $H_2(z)$ both serve as anti-aliasing and frequency splitters. As mentioned above, the signals $\theta_1(n)$ and $\theta_2(n)$ are each downsampled by 2 to give the subband signals $v_1(n)$ and $v_2(n)$. In a typical application the two signals are further processed through a quantizer and transmitted to

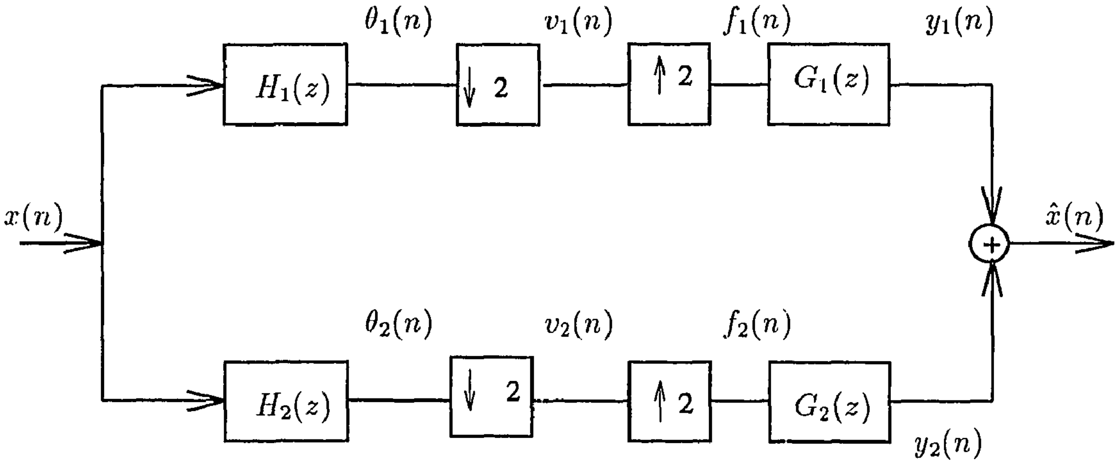

Figure 2.4 Two band filter bank

the receiver. In order to derive the PR conditions, we will assume that no processing occurs between the transmitter and receiver, and therefore, the received signals are $v_1(n)$ and $v_2(n)$. At the receiver end, these two signals are upsampled and filtered by the interpolation filters to restore the missing samples. The resulting signals are summed up to yield the reconstructed signal. Tracing the signals through out the top branch gives

$$\begin{aligned} \theta_1(z) &= H_1(z)X(z) \\ Y_1(z) &= G_1(z)F_1(z) \end{aligned} \tag{2.22}$$

The input/output relationships of the downsampler and upsampler are

$$\begin{aligned} V_1(z) &= \frac{1}{2}\left[\theta_1(z^{1/2}) + \theta_1(-z^{1/2})\right] \\ F_1(z) &= V_1(z^2) \end{aligned} \tag{2.23}$$

Putting all of these expressions together leads to

$$Y_1(z) = \frac{1}{2}G_1(z)\left[H_1(z)X(z) + H_1(-z)X(-z)\right] \tag{2.24}$$

Likewise for the bottom branch, we get

$$Y_2(z) = \frac{1}{2}G_2(z)\left[H_2(z)X(z) + H_2(-z)X(-z)\right] \tag{2.25}$$

The reconstructed output signal $\hat{X}(z)$ is the sum of $Y_1(z)$ and $Y_2(z)$ as

$$\begin{aligned} \hat{X}(z) &= \frac{1}{2}\left[H_1(z)G_1(z) + H_2(z)G_2(z)\right]X(z) \\ &\quad + \frac{1}{2}\left[H_1(-z)G_1(-z) + H_2(-z)G_2(-z)\right]X(-z) \\ &= T(z)X(z) + S(z)X(-z) \end{aligned} \tag{2.26}$$

The reconstructed signal consists of two parts. The first one $T(z)X(z)$ is the original signal multiplied by some transfer function $T(z)$. The second part is termed as the aliasing component. This anomaly is introduced because of the finite roll-off in filter responses. To achieve perfect reconstruction, we require the following

$$\begin{aligned} (1)\ \ S(z) &= 0,\ \textit{for all } z \\ (2)\ \ T(z) &= cz^{-n_o},\ \textit{where } c \textit{ is a constant} \end{aligned} \tag{2.27}$$

The first requirement gets rid of the unwanted aliasing terms. Whereas the second one implies that the output should be a scaled , translated replica of the input. This can be succeeded if we choose

$$\begin{aligned} G_1(z) &= -H_2(z) \\ G_2(z) &= H_1(z) \end{aligned} \tag{2.28}$$

This in turn makes $T(z)$ become

$$T(z) = \frac{1}{2}\left[H_1(-z)H_2(z) - H_1(z)H_2(-z)\right] \tag{2.29}$$

Now the first requirement is met. We let the analysis filters be related as

$$H_2(z) = z^{-(N-1)}H_1(-z^{-1}) \tag{2.30}$$

$T(z)$ further becomes

$$T(z) = \frac{1}{2}z^{-(N-1)}\left[H_1(z)H_1(z^{-1}) + H_1(-z)H_1(-z^{-1})\right] \tag{2.31}$$

Then, the second requirement imposes the following condition

$$\begin{aligned} Q(z) &= H_1(z)H_1(z^{-1}) + H_1(-z)H_1(-z^{-1}) = constant \\ &= R(z) + R(-z) = constant \end{aligned} \tag{2.32}$$

We notice that $R(z)$ and $R(-z)$ are nothing else but the spectral density of the filters $H_1(z)$ and $H_1(-z)$, respectively. Therefore, we write $R(z)$ and $R(-z)$ as

$$\begin{aligned} R(z) &= \sum_{k=-(N-1)}^{(N-1)} \alpha_k z^{-k} \\ R(-z) &= \sum_{k=-(N-1)}^{(N-1)} (-1)^k \alpha_k z^{-k} \end{aligned} \tag{2.33}$$

We can deduce from Eq. (2.33) that $\{\alpha_k\}$ has to be zero for even values of k except $k = 0$ in order to have $Q(z)$ be a constant. We can take this result a bit further by recalling that $R(z)$ is also the Z-transform of the autocorrelation function $\rho(n)$ of $h_1(n)$, $\rho(n)$ is given as

$$\rho(n) = \sum_k h_1(k)h_1(n+k) \tag{2.34}$$

We are able to recast Eq. (2.32) into a time domain requirement as

$$\rho(2n) = \sum_k h_1(k)h_1(k+2n) = \delta(n) \tag{2.35}$$

where $\delta(n)$ is the Dirac δ. What this equation tells us is that if the filters are chosen as above and if further the lowpass analysis filter satisfies Eq. (2.35), we get a two-band perfect reconstruction quadrature mirror filter (PR-QMF) bank structure. Eq. (2.35) can be interpreted as requiring $h_1(n)$ to be orthogonal to its own translates shifted by 2. This is called the paraunitary requirement for perfect reconstruction.

We can generalize this result for an M-band structure as shown in Fig. 2.5. In this case, the perfect reconstruction condition in time domain is found as [2]

$$\sum_k h_r(k)h_s(k+Mn) = \delta(r-s)\delta(n) \tag{2.36}$$

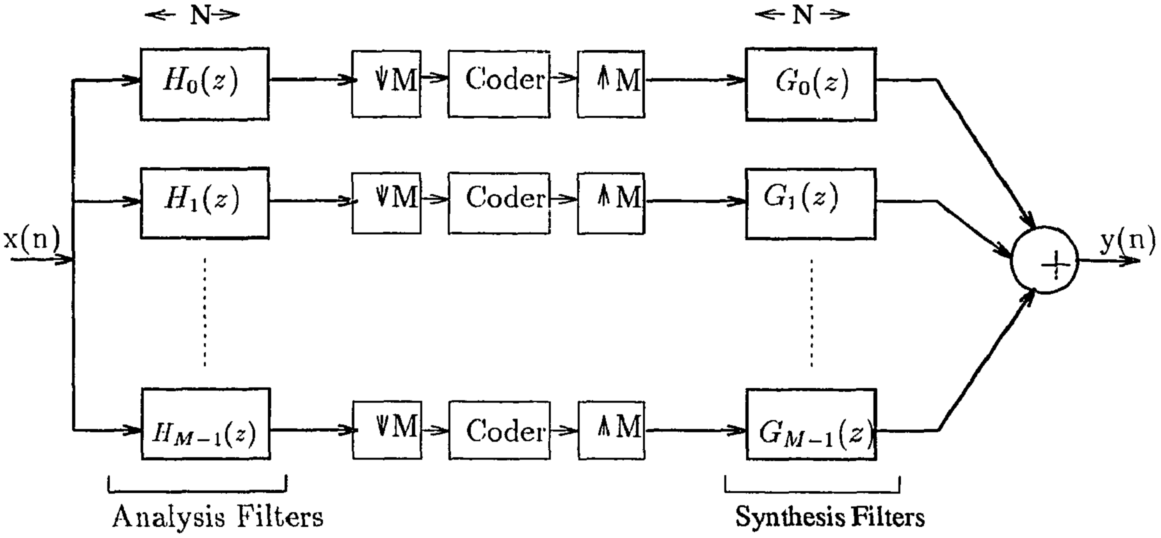

Figure 2.5 Maximally decimated M-band filter bank

The above equation asserts that $h_r(k)$ is orthogonal to its own translates shifted by multiples of M and $r \neq s$, $h_r(k)$ is orthogonal to all M translates of $h_s(k)$.

2.2.4 M-band Multiplierless Filter Design Example

At this point, we would like to present a design example of filter banks. We designed a four band eight-tap PR linear phase filter bank. In addition, we restricted the filter coefficients to be multiplier-free. The filter coefficients $\{a_i\}$ will be of the form

$$a_i = \pm 2^{\pm k} \pm 1 \tag{2.37}$$

where k is an integer. This type of filters have great practical merits because of the computational efficiency they offer. In fact, the usual multiplication taking place in a filtering operation is implemented via a simple shift (left or right) plus an addition in this case. The filter coefficients are tabulated below (Table 2.1). The magnitude responses of the four bands are depicted in Fig. 2.6.

Table 2.1 Filter coefficients of a four band 8-tap PR filter bank

Band 1	Band 2	Band 3	Band 4
$-2^{-2} + 1$	$2^{-2} + 1$	$2^{-2} + 1$	$-2^{-2} + 1$
-2^{-2} - 1	2^{-2} - 1	$-2^{-2} + 1$	$2^{-2} + 1$
-2^{1} - 1	-2^{2} - 1	-2^{2} - 1	-2^{1} - 1
-2^{2} - 1	-2^{1} - 1	$2^{1} + 1$	$-2^{2} + 1$
-2^{2} - 1	$2^{1} + 1$	$2^{1} + 1$	2^{2} - 1
-2^{1} - 1	$2^{2} + 1$	-2^{2} - 1	$2^{1} + 1$
-2^{-2} - 1	$-2^{-2} + 1$	$-2^{-2} + 1$	-2^{-2} - 1
$-2^{-2} + 1$	-2^{-2} - 1	$2^{-2} + 1$	2^{-2} - 1

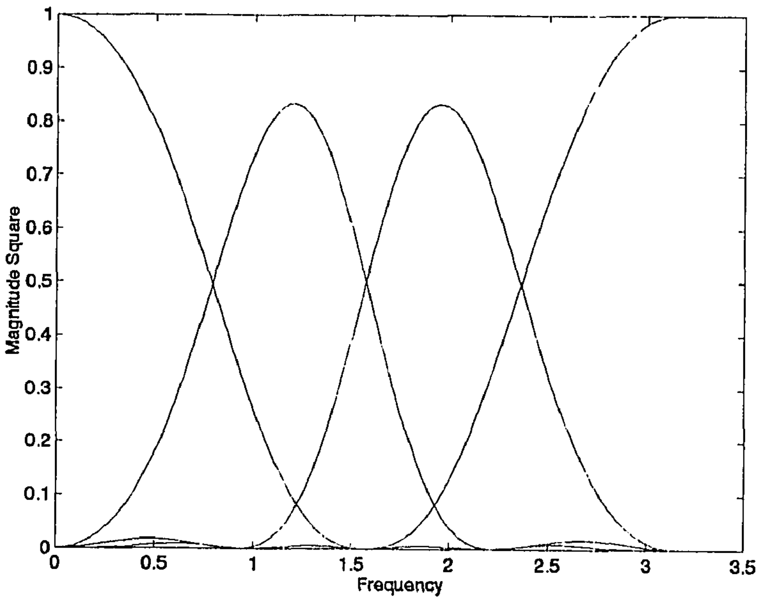

Figure 2.6 Magnitude response of a multiplierless four band filter bank

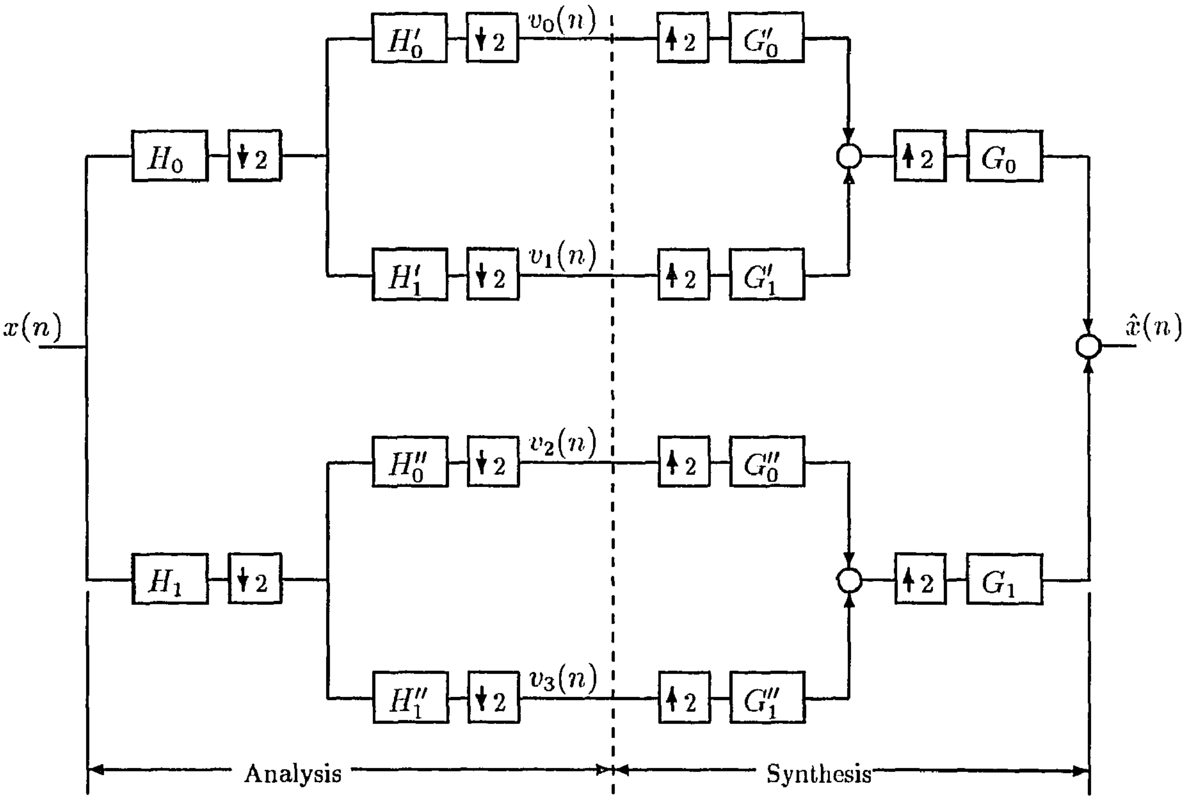

Figure 2.7 Four band regular binary tree structure

2.2.5 Tree Extensions and Multiresolution

The two band filter bank is the progenitor for the construction of tree structures. A variety of tree structures can be obtained by a repetitive use of this prototype filter bank yielding a wide span of resolutions of the original signal. Several tree structures capable of different decompositions were studied by Akansu and Liu[4]. If the signal is decomposed at each node beyond the first level, we obtain a regular binary tree. A four band binary tree is illustrated in Fig. 2.7. This structure can be redrawn into an equivalent structure of Fig. 2.9 by invoking the "noble identities" shown in Fig. 2.8[2][40]. It should be noted here that the splitting filters at different stages need not be the same [38]. However, if the entire structure is required to be PR, each stage should satisfy that requirement.

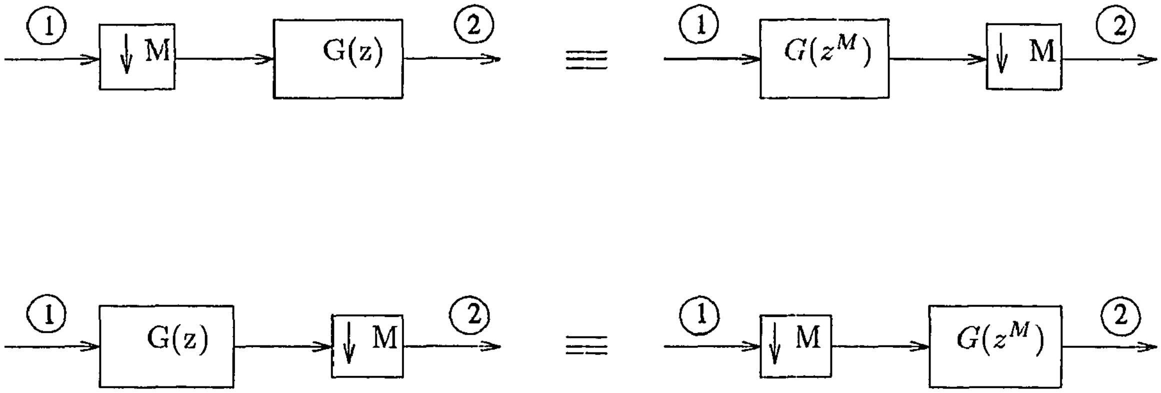

Figure 2.8 Noble identities

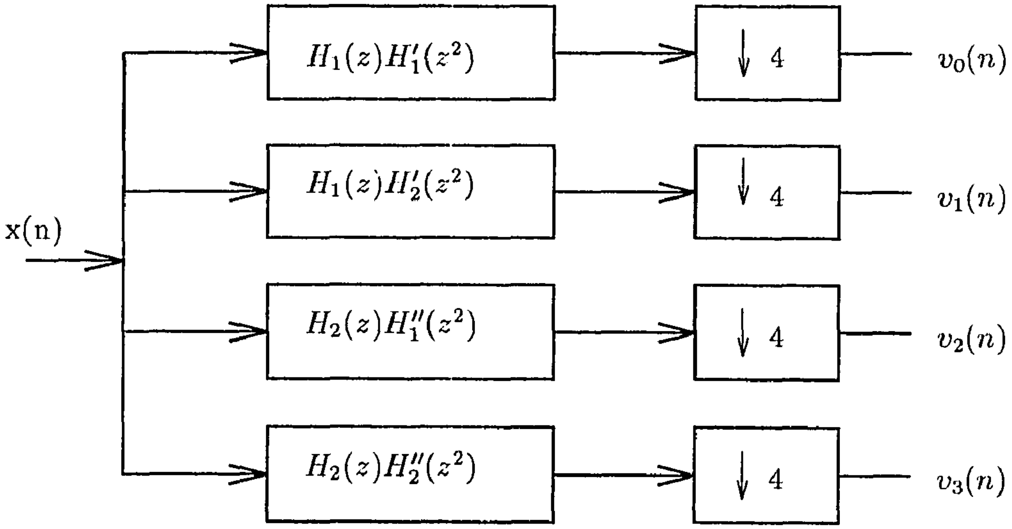

Figure 2.9 Equivalent structure

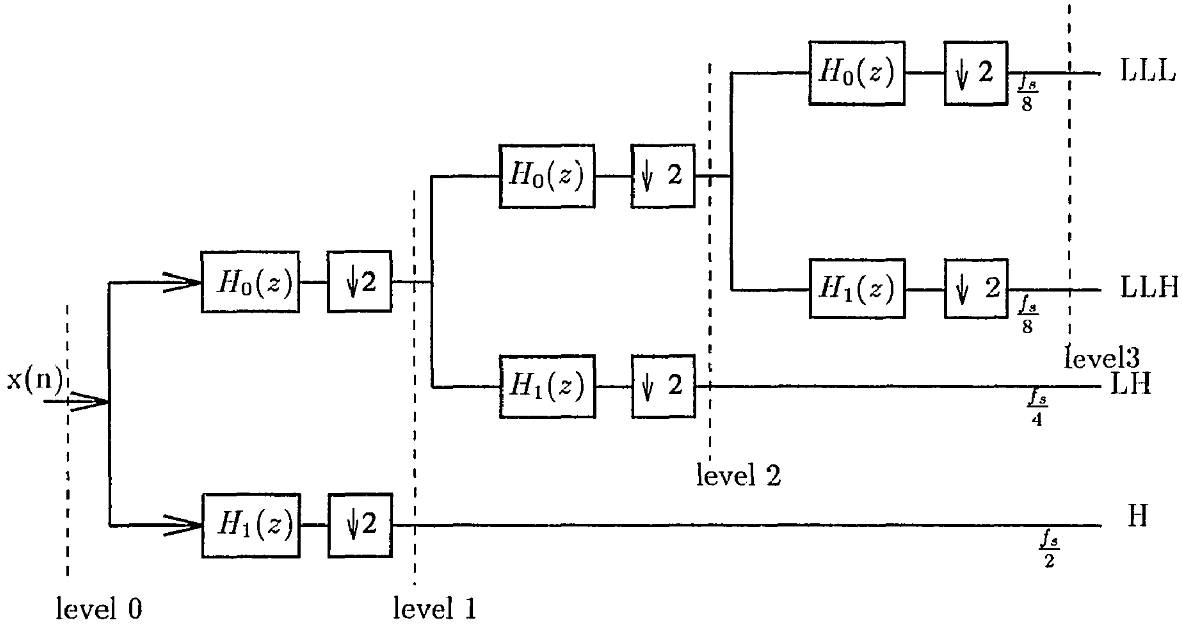

Figure 2.10 Three level dyadic tree structure

A dyadic or octave-band tree is obtained when only the lower half of the spectrum is partitioned into two equal bands at any level of the tree. Fig. 2.10 depicts a dyadic tree. At any level, the lower frequency component is called the "coarse" approximation, whereas the high frequency term is called the detail at that resolution. A dyadic tree is then a hierarchical data structure containing information about a signal at different resolutions. It can be viewed as a multiresolution decomposition. Unlike in the binary and dyadic tree structures, splitting a spectrum does not have to follow a repetitive scheme, but can take place at any node depending on the need for the decomposition. This type of split yields irregular tree structures as shown in Fig. 2.11.

2.3 The Wavelet Transform and Its Linkages with Filter Banks

The wavelet transform is a tool to decompose an analog or continuous-time signal with a family of orthonormal functions $\{\psi_{ab}(t)\}$. These $\{\psi_{ab}(t)\}$ functions are derived

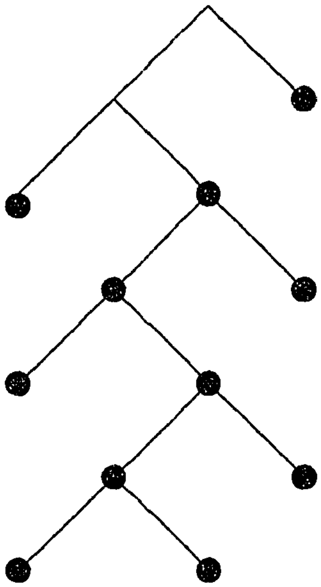

Figure 2.11 Irregular tree structure

from a prototype kernel function $\psi(t)$ known as the mother function through dilations and translations of $\psi(t)$ as[17]

$$\psi_{ab}(t) = \frac{1}{\sqrt{a}}\psi(\frac{t-b}{a}) \tag{2.38}$$

where $a \geq 0$, and $-\infty < b < \infty$. So, we can define the wavelet transform of a signal $x(t)$ as [17]

$$W(a,b) = \int_{-\infty}^{\infty} \psi_{ab}(t)x(t)dt \tag{2.39}$$

On the other hand, $x(t)$ is synthesized through the inverse wavelet transform as

$$x(t) = \frac{1}{C}\int_{-\infty}^{\infty}\int_{0}^{\infty}\frac{dadb}{a^2}W(a,b)\psi_{ab}(t) \tag{2.40}$$

where

$$C = \int_{0}^{\infty}\frac{|\Psi(\Omega)|^2}{\Omega}d\Omega \tag{2.41}$$

$\Psi(\Omega)$ is the Fourier transform of $\psi(t)$. The invertibility of the wavelet transform is secured if $\psi(t)$ satisfies an *admissibility* condition, namely C being finite[17].

2.3.1 The Discrete Wavelet Transform

The discretization of a and b leads to the discrete wavelet transform (DWT). This is somehow a misnomer because the operation still takes place in the continuous-time domain. In this case, the wavelet decomposition of $x(t)$ behaves as

$$d_{m,n} = \int_{-\infty}^{\infty} x(t)\psi_{m,n}(t)dt \tag{2.42}$$

and the synthesis formula is

$$x(t) = \sum_{m}\sum_{n} d_{m,n}\psi_{mn}(t) \tag{2.43}$$

where $\{\psi_{ab}(t)\}$ as a result of the discretization becomes

$$\psi_{mn}(t) = 2^{-m/2}\psi(2^{-m}t - n) \tag{2.44}$$

The construction of the mother wavelet $\psi(t)$ necessitates the following steps[17]:

1. Determination of the complementary scaling function $\phi(t)$ which satisfies the inter-scale property

   $$\phi(t) = \sqrt{2}\sum_{n} h(n)\phi(2t - n) \tag{2.45}$$

   Similarly, the mother wavelet also satisfies the containment condition

   $$\psi(t) = \sqrt{2}\sum_{n} g(n)\phi(2t - n) \tag{2.46}$$

   It was shown that the inter-scale coefficients $h(k)$ and $g(k)$ are nothing else but the lowpass and highpass filters of a two-band perfect reconstruction filter bank, respectively. The Fourier transforms of $\phi(t)$ and $\psi(t)$ are related to the Fourier transform of inter-scale coefficients as

   $$\Phi(\Omega) = \prod_{k=1}^{\infty} H(e^{j\frac{\omega}{2^k}}) \tag{2.47}$$

   and

   $$\Psi(\Omega) = G(e^{j\frac{\omega}{2}})\prod_{k=2}^{\infty} H(e^{j\frac{\omega}{2^k}}) \tag{2.48}$$

where $H(e^{j\omega})$ and $G(e^{j\omega})$ are the Fourier transforms of $h(k)$ and $g(k)$, respectively. For these infinite products to converge, we require that $H(z)$ to have a certain degree of regularity, i.e. having at least one zero at $\omega = \pi$ or equivalently at $z = -1$. It turns out that the orthonormality and finite support of the scaling and wavelet functions are set up by the orthonormality and finite duration of $h(k)$, and $g(k)$. Eq.(2.47) and Eq.(2.48) provide the methodology for the construction of wavelet and scaling families. One simply starts with any paraunitary, compact support (i.e. finite duration) two-band filter bank. The Fourier transforms of the wavelet and scaling functions are then obtained by the infinite products in Eq.(2.47) and Eq. (2.48). These equations imply the following completeness properties of wavelet and scaling bases.

2. The wavelets are orthonormal in both indices. They are orthonormal in time n at the same scale m, and orthonormal across scales (intra- and inter-scale orthonormalities),

$$< \psi_{m,n}(t), \psi_{m',n'}(t) >= \delta_{m-m'}\delta_{n-n'} \tag{2.49}$$

3. The complementary scaling function $\phi(t) \leftrightarrow \Phi(\Omega)$ is orthonormal within the same scale (intra-scale orthonormality only),

$$< \phi_{mn}(t), \phi_{mn'}(t) >= \delta_{n-n'} \tag{2.50}$$

where

$$\phi_{mn}(t) = 2^{-m/2}\phi(2^{-m}t - n) \tag{2.51}$$

The scaling function is a low-pass function.

4. Complementary property of the wavelet and scaling bases

$$< \psi_{mn(t)}, \phi_{m'n'}(t) >= 0 \tag{2.52}$$

CHAPTER 3

TIME-FREQUENCY LOCALIZATION IN TRANSFORMS, SUBBANDS AND WAVELETS

The goal of this chapter is to study and clarify the notion of time and frequency localizations as it is pertinent to both the analog and the discrete-time signal domains. This notion is based on the famous uncertainty principle that gives a lower bound of the joint localization.

3.1 Time-frequency Distributions and Optimum Signal Shaping

The time-frequency shaping of a single function in both the analog and discrete-time domain is very well understood. The trade-offs between the time and frequency domain localizations have been well known[30][13]. It is simply explained by the well known uncertainty principle. From a transform point of view, we would like to extend this concept to do time-frequency shaping of a set of functions which must be complete. To better understand this shaping, a discrete-time version of the uncertainty principle is derived.

3.1.1 Classical Uncertainty

The basic objective in signal analysis is to devise an operator capable of extracting local features of a signal in both time and frequency domains. This requires a basis function, or kernel, whose spread or extent is simultaneously narrow in both domains. This in turn suggests that the transformation kernel $\phi(t)$ and its Fourier transform $\Phi(\Omega)$ should have narrow spreads about selected points t_0, and Ω_0.

However, the classical uncertainty principle asserts that for any function $\phi(t)$, (with $\sqrt{t}\phi(t) \to 0$, as $t \to \pm\infty$)[30][13],

$$\sigma_T \sigma_\Omega \geq \frac{1}{2} \tag{3.1}$$

where σ_T, σ_Ω are the RMS spreads in time and frequency, respectively, of $\phi(t)$ and $\Phi(\Omega)$ about the center values. That is

$$\begin{aligned}\sigma_T^2 &= \frac{\int (t-\bar{t})^2|\phi(t)|^2 dt}{E},\\ \sigma_\Omega^2 &= \frac{\frac{1}{2\pi}\int_{-\infty}^{\infty}(\Omega-\bar{\Omega})^2|\Phi(\Omega)|^2 d\Omega}{E}\end{aligned} \tag{3.2}$$

where E is the energy in the signal,

$$E = \int_{-\infty}^{\infty}|\phi(t)|^2 dt = \frac{1}{2\pi}\int_{-\infty}^{\infty}|\Phi(\Omega)|^2 d\Omega \tag{3.3}$$

and $\bar{t}$, $\bar{\Omega}$ refer to the center-of-mass of these kernels,

$$\begin{aligned}\bar{t} &= \frac{\int_{-\infty}^{\infty} t|\phi(t)|^2 dt}{E},\\ \bar{\Omega} &= \frac{\frac{1}{2\pi}\int_{-\infty}^{\infty}\Omega|\Phi(\Omega)|^2 d\Omega}{E}\end{aligned} \tag{3.4}$$

The product $\sigma_T\sigma_\Omega$ is called the resolution cell. The equal sign holds in Eq. (3.1) if and only if $\phi(t)$ (and consequently, its Fourier transform), is Gaussian of the form $e^{-\alpha t^2}$. The derivation of this result can be found in[30].

The Short-Time Fourier Transform(STFT) has been used to extract frequency characteristics of a signal over some selected interval in time. The STFT positions a window function $g(t)$ at some point τ on the time axis and calculates the Fourier transform of the signal contained within the spread or extent of that window,

$$F(\beta,\tau) = \int_{-\infty}^{\infty} f(t)g(t-\tau)e^{j\beta t}dt \tag{3.5}$$

When the window function $g(t)$ is Gaussian, the STFT is called Gabor transform[18][13]. The basis functions are generated by *modulation* and *translation* of the window function by the parameters β and τ, respectively. Note that when τ increases, the kernel simply translates in time while keeping the spread of the window fixed.

Let $g(t) \leftrightarrow G(\Omega)$ be a Fourier transform pair, and assume that $\bar{t} = 0$, and $\bar{\Omega} = 0$. Then the translated, modulated kernel pair are given by

$$g_{\tau,\beta}(t) = g(t-\tau)e^{j\beta t} \leftrightarrow G_{\tau,\beta}(\Omega) = e^{-j(\Omega-\beta)\tau}G(\Omega-\beta) \tag{3.6}$$

This two-parameter family is centered at τ, β in the time-frequency plane, i.e.

$$\bar{t}_{\tau,\beta} = \tau, \qquad \bar{\Omega}_{\tau,\beta} = \beta \tag{3.7}$$

Now it is readily shown that the spread of this shifted, modulated kernel is constant in both domains, i.e.

$$\begin{aligned} \sigma^2_{\Omega(\tau,\beta)} &= \frac{\frac{1}{2\pi}\int_{-\infty}^{\infty}(\Omega-\beta)|G_{\tau,\beta}(\Omega)|^2 d\Omega}{E} = \sigma^2_{\Omega} \\ \sigma^2_{T(\tau,\beta)} &= \int_{-\infty}^{\infty}(t-\tau)^2|g_{\tau,\beta}(t)|^2 dt = \sigma^2_T \end{aligned} \tag{3.8}$$

where σ_Ω, σ_T are the RMS spreads of the unmodulated, untranslated kernels. This implies that the resolution cell $\sigma_T\sigma_\Omega$ has a constant shape, as well as a constant area in the time frequency plane as shown in Fig. 3.1. For the Gaussian window $\sigma_T\sigma_\Omega = 1/2$. The wavelet transform, introduced in the previous chapter, has a variable shape, but constant product time-frequency tiles as seen in Fig. 3.1.

3.1.2 Discrete-time Uncertainty Theorem

The discrete-time version of uncertainty is as follows: Let $f(n) \leftrightarrow F(e^{j\omega})$ be a discrete-time Fourier transform pair,

$$F(e^{j\omega}) = \sum_{n=-\infty}^{\infty} f(n)e^{-jn\omega} \leftrightarrow f(n) = \frac{1}{2\pi}\int_{-\pi}^{\pi} F(e^{j\omega})e^{jn\omega}d\omega \tag{3.9}$$

By the Parseval theorem, the energy of the signal is given in both domains as

$$E = \sum_{n=-\infty}^{\infty}|f(n)|^2 = \frac{1}{2\pi}\int_{-\pi}^{\pi}|F(e^{j\omega})|^2 d\omega \tag{3.10}$$

We define the mean (analogous to the center-of-mass of a distribution) by[2]

$$\bar{\omega} = \frac{\frac{1}{2\pi}\int_{-\pi}^{\pi}\omega|F(e^{j\omega})|^2 d\omega}{E} \tag{3.11}$$

$$\bar{n} = \frac{\sum_{-\infty}^{\infty} n|f(n)|^2}{E} \tag{3.12}$$

The spreads of a function in time and in frequency domains are defined as

$$\begin{aligned} \sigma_n^2 &= \frac{\sum_{-\infty}^{\infty}(n-\bar{n})^2|f(n)|^2}{E}, \\ \sigma_\omega^2 &= \frac{\frac{1}{2\pi}\int_{-\pi}^{\pi}(\omega-\bar{\omega})^2|F(e^{j\omega})|^2 d\omega}{E} \end{aligned} \tag{3.13}$$

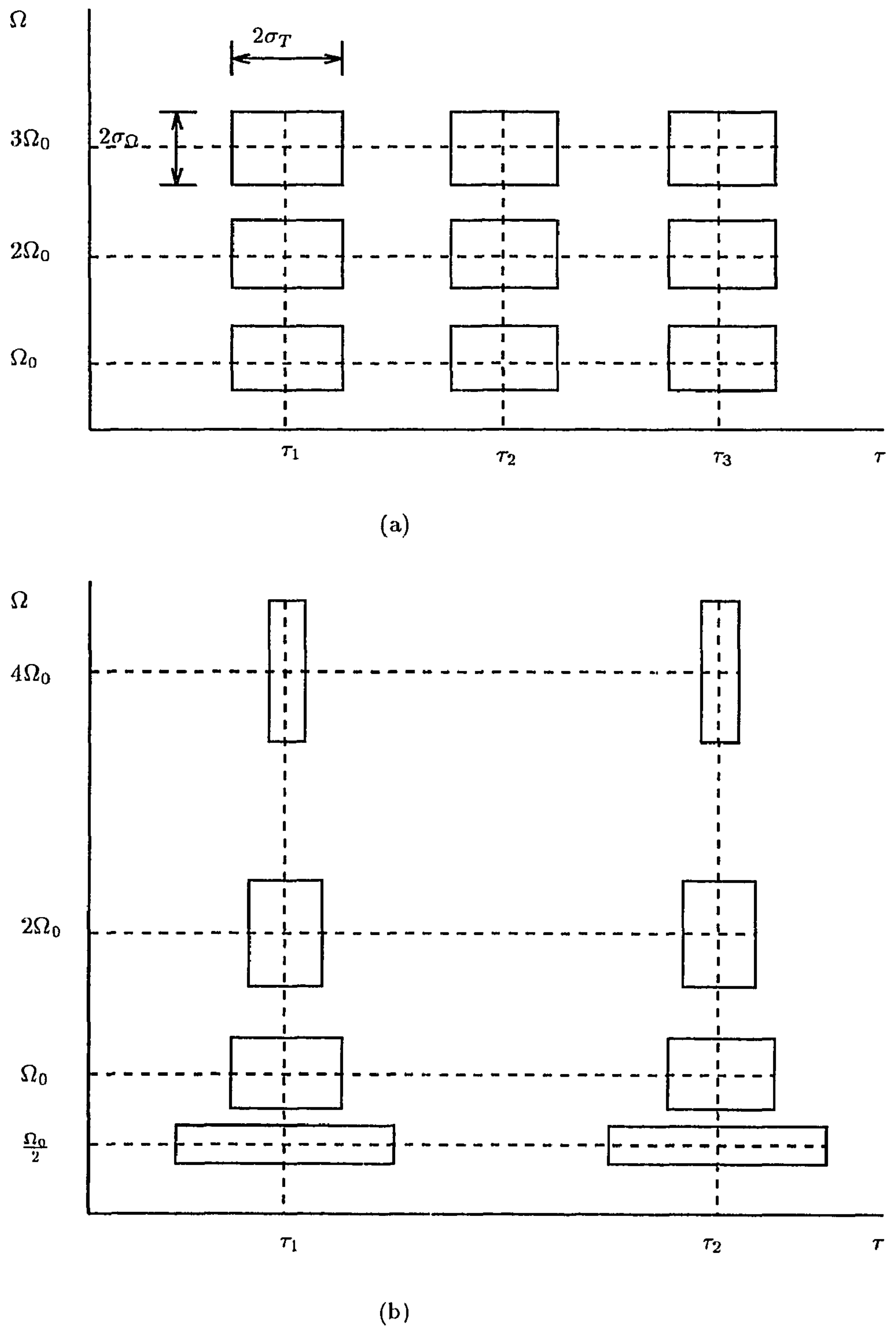

Figure 3.1 (a) Time-Frequency plane showing resolution cells for STFT, (b) Resolution cells for wavelet transform

Theorem: For any real signal $\bar{\omega} = 0$, and without loss of generality, we can also shift the time origin to make $\bar{n} = 0$. For this case, we show that the time-frequency product $\sigma_n \sigma_\omega$ or resolution cell is given by

$$\begin{aligned} \sigma_n \sigma_\omega &\geq \frac{|1-\mu|}{2} \\ \mu &\triangleq \frac{|F(e^{j\omega})_{\omega=\pi}|^2}{E} = \frac{|F(-1)|^2}{E} \end{aligned} \tag{3.14}$$

Proof: For convenience let $\bar{n} = 0$, and note that

$$nf(n) \leftrightarrow j\frac{dF}{d\omega} \tag{3.15}$$

so that

$$\sum_n n^2 |f(n)|^2 = \frac{1}{2\pi}\int_{-\pi}^{\pi} |\frac{dF}{d\omega}|^2 d\omega \tag{3.16}$$

By the Schwartz' inequality, we have

$$|I|^2 = |\frac{1}{2\pi}\int_{-\pi}^{\pi} \omega F^*(e^{j\omega})\frac{dF}{d\omega}d\omega|^2 \leq [\frac{1}{2\pi}\int_{-\pi}^{\pi}\omega^2|F(e^{j\omega})|^2 d\omega][\frac{1}{2\pi}\int_{-\pi}^{\pi}|\frac{dF}{d\omega}|^2 d\omega] \tag{3.17}$$

Integrating by parts,

$$\begin{aligned} I &= \frac{1}{2\pi}[\omega|F(e^{j\omega})|^2]_{-\pi}^{\pi} - \frac{1}{2\pi}\int_{-\pi}^{\pi} F(e^{j\omega})[\omega dF^* + F^* d\omega] \\ &= |F(-1)|^2 - \frac{1}{2\pi}\int_{-\pi}^{\pi}\omega F(e^{j\omega})\frac{dF^*}{d\omega}d\omega - \frac{1}{2\pi}\int_{-\pi}^{\pi}|F(e^{j\omega})|^2 d\omega \\ &= |F(-1)|^2 - I^* - E \end{aligned} \tag{3.18}$$

or

$$I + I^* = |F(-1)|^2 - E$$

But,

$$|I + I^*| \leq 2|I|$$

for any complex number, therefore

$$\left|\frac{I}{E}\right| = \sigma_\omega \sigma_n \geq \frac{1}{2E}\left|E - |F(-1)|^2\right| = \frac{1}{2}|1-\mu|$$

In the analog version, $F(\pm\infty) = 0$, and the lower limit is simply $1/2$. In the discrete-time case $F(-1)$ need not be zero. Note that in our notation $F(e^{j\omega})$ at $\omega = 0$, and $\omega = \pi$ are denoted by $F(1)$ and $F(-1)$, respectively.

Remark: The frequency measure in Eq. (3.13) is not suitable for bandpass signals with peak frequency responses centered at $\pm\hat{\omega}$. In order to obtain a measure of the spread about $\hat{\omega}$, we need to define σ_ω^2 on the interval $[0, \pi]$, rather than $[-\pi, \pi]$. In this case we will use

$$\hat{\omega} = \frac{\frac{1}{\pi}\int_0^\pi \omega |F(e^{j\omega})|^2 d\omega}{\frac{1}{\pi}\int_0^\pi |F(e^{j\omega})|^2 d\omega} \tag{3.19}$$

$$\hat{\sigma}_\omega^2 = \frac{\frac{1}{\pi}\int_0^\pi (\omega - \hat{\omega})^2 |F(e^{j\omega})|^2 d\omega}{\frac{1}{\pi}\int_0^\pi |F(e^{j\omega})|^2 d\omega} \tag{3.20}$$

and σ_n^2 remains unchanged. It easily follows that

$$\hat{\sigma}_\omega^2 = \sigma_\omega^2 - (\hat{\omega})^2 \tag{3.21}$$

and

$$\hat{\sigma}_\omega^2 \sigma_n^2 \geq \frac{1}{4}(1 - \mu)^2 - (\hat{\omega})^2 \sigma_n^2 \tag{3.22}$$

Eq. (3.22) demonstrates the reduction in the time-frequency product when using the $[0, \pi]$ interval for bandpass signals. An alternative derivation similar to the above proof, shows that this product can be expressed as

$$\hat{\sigma}_\omega \sigma_n \geq \frac{1}{2}|1 - \mu'|$$
$$\mu' = \frac{\hat{\omega}}{\pi}\frac{|F(1)|^2}{E} + (1 - \frac{\hat{\omega}}{\pi})\frac{|F(-1)|^2}{E} \tag{3.23}$$

For bandpass signals with zero DC gain, $F(1) = 0$, Eq. (3.23) reduces to

$$\mu' = (1 - \frac{\hat{\omega}}{\pi})\frac{|F(-1)|^2}{E} \tag{3.24}$$

If, additionally, we have $F(-1) = 0$, then $\mu' = 0$, and

$$\hat{\sigma}_\omega \sigma_n \geq \frac{1}{2} \tag{3.25}$$

In the sequel we concentrate on low-pass filters such that $F(e^{j\omega})_{max}$ occurs at $\omega = 0$ and use Eqs. (3.13) and (3.14). In this case, there are two classes of filters or signals. The first class is that of signals possessing a certain degree of regularity, namely

$$\text{Class I:} \qquad F(-1) = 0 \rightarrow \sigma_n\sigma_\omega \geq \frac{1}{2} \tag{3.26}$$

Whereas, the second class is free of this requirement,

$$\text{Class II:} \qquad F(-1) \neq 0 \rightarrow \sigma_n\sigma_\omega \geq \frac{|1-\mu|}{2} \tag{3.27}$$

The bound on the time-frequency product in the first case is the same as that for the continuous-time case(in which $F(\pm\infty) = 0$). In the analog case, we know that the equality in the lower bound is achieved when $\Omega F(\Omega)$ is proportional to $\frac{dF}{d\Omega}$, or $F(\Omega) = Ke^{-b\Omega^2/2}$, a Gaussian. In the discrete-time formulation, we have the same form of integral resulting in the differential equation

$$\frac{dF}{d\omega} = -K\omega F^*(e^{j\omega}) \tag{3.28}$$

whose solution is a Gaussian $e^{-K\omega^2/2}$. This Gaussian function satisfies the differential equation but cannot satisfy the Class I boundary condition $F(e^{j\pi}) = 0$. In this case we conclude that the lower bound cannot be attained and the strict inequality holds, $\sigma_n\sigma_\omega > \frac{1}{2}$. For the Class II set of functions, the Gaussian can satisfy both the differential equation and the boundary condition resulting in the equality $\sigma_n\sigma_\omega = \frac{1}{2}|1-\mu|$.

3.1.3 Gaussian Distributions

For the Class II signals, the Gaussian is

$$\begin{aligned} |F(e^{j\omega})|^2 &= Ke^{-\omega^2/2\sigma^2}, \qquad |\omega| < \pi \\ K &= \frac{\sqrt{\pi/2}}{\sigma erf(\pi/\sigma)} \end{aligned} \tag{3.29}$$

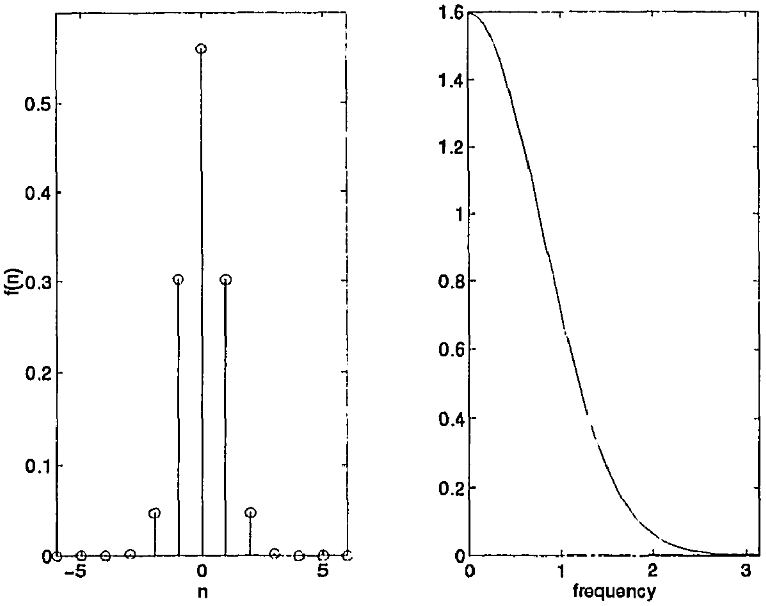

Figure 3.2 Time and frequency plots for narrow-band Gaussian functions

The constant K is chosen so as to normalize the signal energy E to unity over $[-\pi, \pi]$. In Appendix A, we show that

$$\begin{aligned} \sigma_\omega &= \sigma\sqrt{1-\mu} \\ \mu &= \frac{|F(\pi)|^2}{E} = Ke^{\pi^2/2\sigma^2} \end{aligned} \tag{3.30}$$

and hence

$$\sigma_\omega \sigma_n = \frac{|1-\mu|}{2}, \rightarrow \sigma_n = \frac{\sqrt{1-\mu}}{2\sigma} \tag{3.31}$$

For the narrow-band case, $\sigma \leq \pi/4$, $\mu \lesssim 10^{-3}$, and $F(-1) \approx 0$, resulting in $\sigma_\omega^2 \approx \sigma^2$, $\sigma_\omega \sigma_n \approx 1/2$. The corresponding time function is found to be approximately Gaussian,

$$f(n) = \sigma\sqrt{\frac{K}{\pi}}e^{-\sigma^2 n^2} \tag{3.32}$$

Examples of these narrow-band Gaussian functions are shown in Fig. 3.2. Again note that the time-frequency product is very close to 1/2 in these cases.

For the wide-band case, with $\sigma \geq 3\pi/8$, we must use the more exact expansions in Eqs. (3.30) and (3.31). For example, for $\sigma = \pi/2$, we calculate $\mu = 0.22625$,

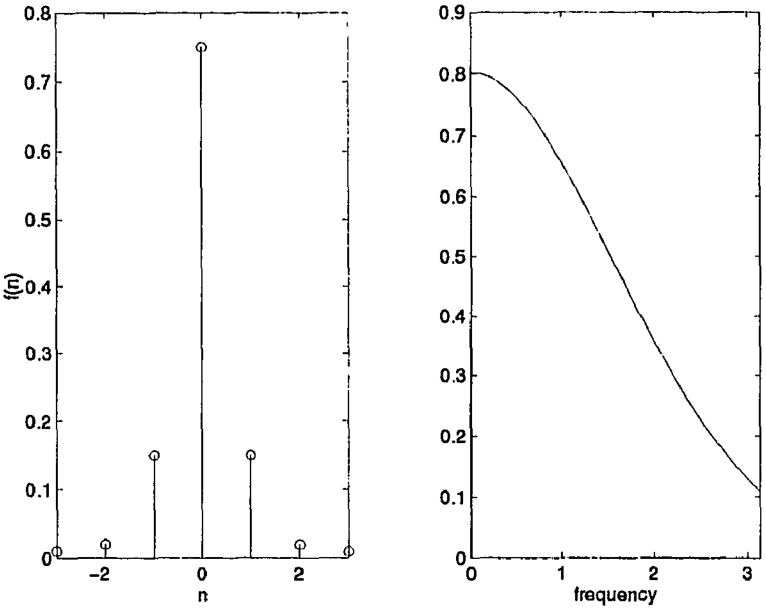

Figure 3.3 Time and frequency plots for wide-band Gaussian functions

$\sigma_\omega = 1.382$, $\sigma_n\sigma_\omega = 0.3869$, and $\sigma_n = 0.28$ time samples. In this case, there is no simple approximation for $f(n)$ which must be computed numerically from the inversion formula, Eq. (3.9). These are shown in Fig. 3.3 where the very short duration of $f(n)$ is duly noted.

3.2 Time-frequency Properties of Block Transforms

We can examine the time-frequency localization of established block transforms by analyzing the time-frequency products of each basis function. The time-frequency spreads for the Discrete Cosine Transform(DCT) and Walsh-Hadamard Transform(WHT) basis functions are given in Table 3.1. The trade-offs in σ_n, and σ_ω as a function of filter length are obvious from this table. In order to sharpen the frequency response, the transform size or filter lengths are increased. As seen in Table 3.1, the frequency spread σ_ω^2 is decreased significantly but at an appreciable increase in σ_n^2 owing to the longer filter lengths or basis sequences. The time-frequency products or resolution cells also increase with the filter length, i.e. with the size of transform.

As mentioned earlier, the basis lengths of block transforms are equal to the number of functions which correspond to the size of the transforms. There is a very limited flexibility in order to improve the frequency selectivity of basis functions. For some of the applications, narrow frequency bands are desirable, and we are led to consider a broader structure– the M-band filter bank, where the length of each analysis and synthesis filter is not constrained. These extended length, or overlapping basis, filters also provide additional degrees of freedom for optimizing other aspects of system performance.

3.3 Time-frequency Properties of Lapped Orthogonal Transforms

In order to obtain narrower frequency bands σ_ω^2, we can expand the length of each analysis and synthesis filter. We should expect a concomitant increase in σ_n^2. The extension of the unitary block transform, non-overlapping basis, results to this case is called the paraunitary solution as discussed previously. We can now compute the time-frequency localization of LOT filter banks and compare them with their block transform antecedents. Table 3.2 displays the localization characteristics of the 8×8 DCT and the 8×16 DCT-based LOT. Again we note the narrowing of the frequency spread and the attendant increase in σ_n^2. The time-frequency products of DCT-LOT basis is significantly less than that of DCT as expected.

3.4 Time-frequency Properties of M-Band and Hierarchical Filter Banks

For our present purposes, we want to evaluate the time-frequency localization properties of some known filter banks. Table 3.3 lists these characteristics for three different 8-tap two-band filter banks, the Binomial QMF[3], the Smith-Barnwell

Table 3.1 Time-frequency localizations of DCT and WHT bases for 2,4, and 8-band cases

	$\overline{\omega}$	$\overline{n}$	σ_ω^2	σ_n^2	$\sigma_\omega^2 \times \sigma_n^2$
2×2 DCT	0	0.50	1.2899	0.2500	0.3225
and WHT	π	0.50	1.2899	0.2500	0.3225
4×4 DCT	0	1.50	0.6787	1.2500	1.2234
	1.27	1.50	0.3809	1.9570	0.7454
	1.85	1.50	0.2424	1.2500	0.3030
	π	1.50	0.4896	0.5428	0.2657
4×4 WHT	0	1.50	0.6787	1.2500	0.8484
	1.29	1.50	0.2424	1.2500	0.3030
	1.85	1.50	0.2424	1.2500	0.3030
	π	1.50	0.6787	1.2500	0.8484
8×8 DCT	0	3.50	0.3447	5.2500	1.8097
	0.74	3.50	0.3021	8.4054	2.5393
	1.02	3.50	0.2413	5.9572	1.4375
	1.36	3.50	0.1957	5.4736	1.0712
	1.71	3.50	0.1488	5.2500	0.7812
	2.08	3.50	0.1206	5.0263	0.6062
	2.45	3.50	0.0797	4.5428	0.3621
	π	3.50	0.1388	2.0955	0.2908
8×8 WHT	0	3.50	0.3447	5.2500	1.8097
	0.82	3.50	0.3485	5.2500	1.8296
	1.15	3.50	0.2977	5.2500	1.5629
	1.43	3.50	0.1488	5.2500	0.7812
	1.72	3.50	0.1488	5.2500	0.7812
	1.99	3.50	0.2977	5.2500	1.5629
	2.33	3.50	0.3485	5.2500	1.8296
	π	3.50	0.3447	5.2500	1.8097

Table 3.2 Time-frequency localizations of 8 × 8 DCT and 8 × 16 DCT-LOT

	$\overline{\omega}$	$\overline{n}$	σ^2_ω	σ^2_n	$\sigma^2_\omega \times \sigma^2_n$
8 × 8 DCT	0	3.50	0.3447	5.2500	1.8097
	0.74	3.50	0.3021	8.4054	2.5393
	1.02	3.50	0.2413	5.9572	1.4375
	1.36	3.50	0.1957	5.4736	1.0712
	1.71	3.50	0.1488	5.2500	0.7812
	2.08	3.50	0.1206	5.0263	0.6062
	2.45	3.50	0.0797	4.5428	0.3621
	π	3.50	0.1388	2.0955	0.2908
8 × 16 DCT-LOT	0	7.50	0.0917	4.654	0.4269
	0.59	7.50	0.0549	7.615	0.418
	0.98	7.50	0.0345	8.387	0.2898
	1.37	7.50	0.0523	8.645	0.4523
	1.76	7.50	0.0367	8.35	0.3070
	2.16	7.50	0.0608	7.549	0.4596
	2.55	7.50	0.0389	7.778	0.3026
	π	7.50	0.119	5.360	0.6419

CQF[35], and the multiplierless PR-QMF[1]. Tables 3.4 and 3.5 also display this comparison for hierarchical structure 4-band(22-tap product filters), and 8-band(50-tap product filters) configurations. In all these cases, the multiplierless structure has the best time-frequency product $\sigma_n \sigma_\omega$, followed by the Smith-Barnwell CQF, and the Binomial QMF. As expected, longer duration filters have narrower σ_ω's and wider σ_n's. Again, as expected, the 8-band, 8-tap block transforms (Table 3.1) have much narrower σ_n's than any of the 8-band tree-structured filter banks, but very poor frequency localization.

Figure 3.4 displays the impulse responses of the product filters of the two-band Binomial QMF based hierarchical regular tree for the 2 and 4-band cases along with the basis functions of the 2 × 2 and 4 × 4 DCT (Fig. 3.5). Figures 3.6 and 3.7 show the corresponding frequency responses. These demonstrate the drawbacks of blindly repeating a two-band PR-QMF module in a hierarchical subband tree. The

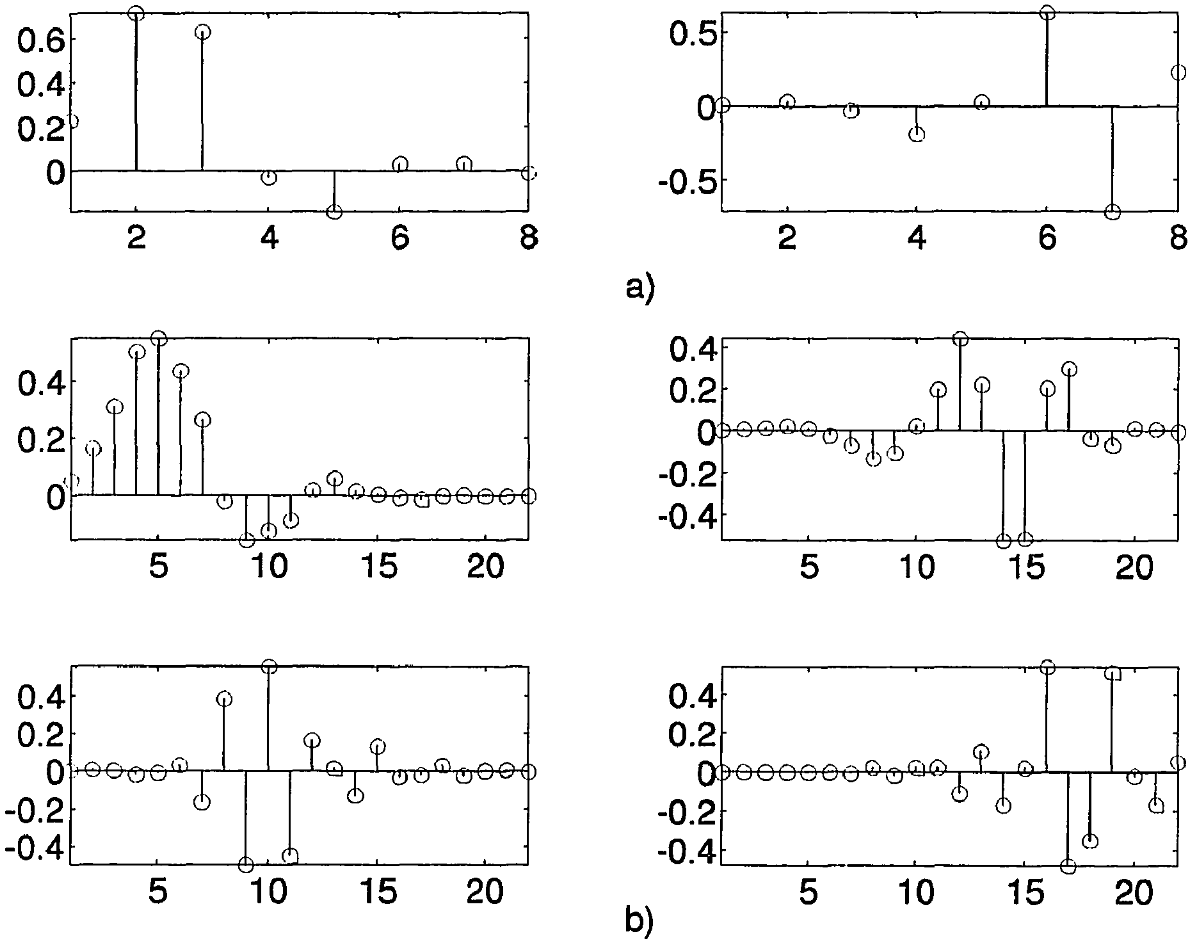

Figure 3.4 Impulse response of the product filters of the two-band binomial QMF-based hierarchical tree for the (a) two-band and (b) four-band case

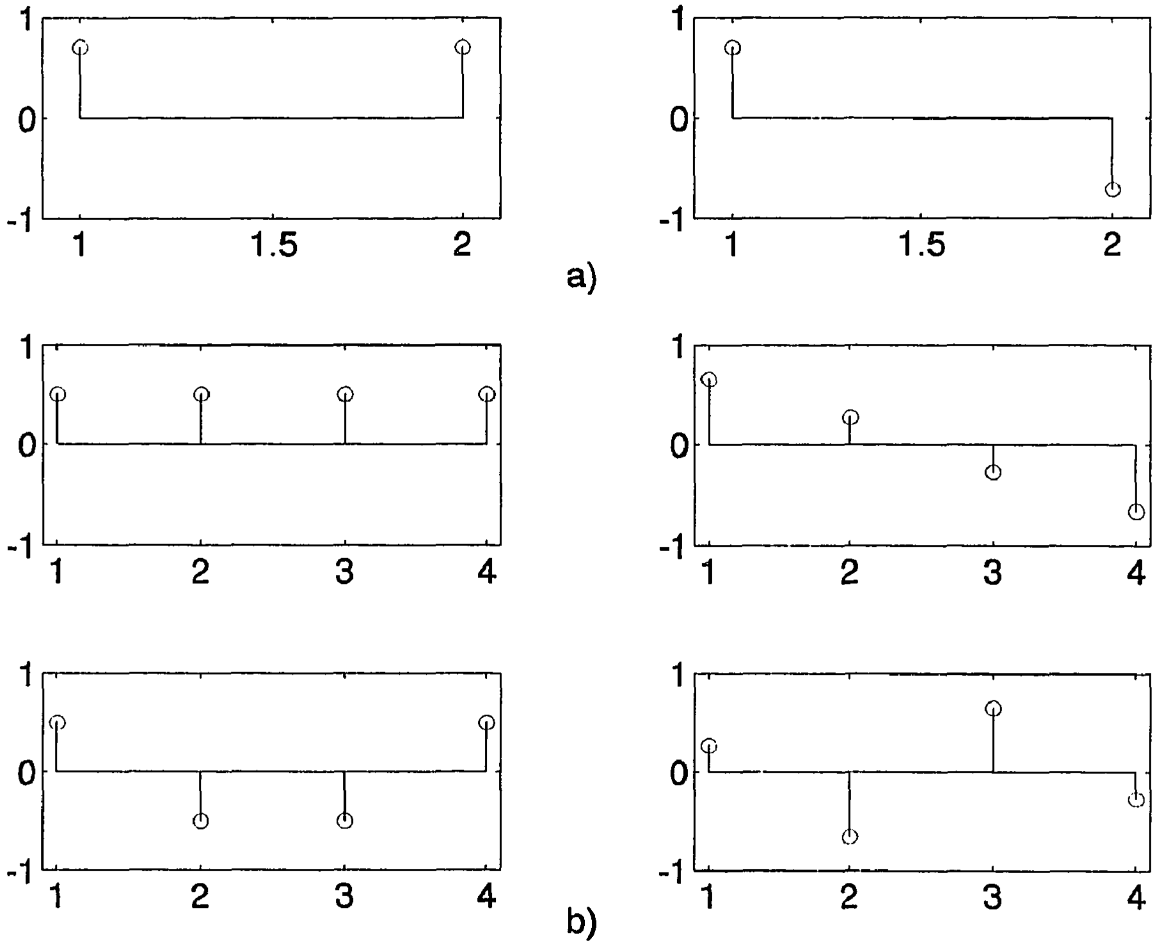

Figure 3.5 Basis functions of the 2 × 2 and 4 × 4 DCT

Table 3.3 The time-frequency localizations of several 8-tap PR-QMF/wavelet filters

	$\overline{\omega}$	$\overline{n}$	σ_ω^2	σ_n^2	$\sigma_\omega^2 \times \sigma_n^2$
B-QMF (8-tap)	0	1.46	0.9468	0.6025	0.5704
	π	5.54	0.9468	0.6025	0.5704
Multiplierless (8-tap)	0	2.50	0.9743	0.3750	0.3654
	π	4.50	0.9743	0.3750	0.3654
Smith-Barnwell (8-tap)	0	4.17	0.9174	0.5099	0.4678
	π	2.83	0.9174	0.5099	0.4678

time spread increases considerably while the time-frequency product degrades. This suggests two possibilities: either design the M-band, single level structure directly or use the hierarchical tree structure, but monitor the product functions from level-to-level.

3.5 Wavelets and Time-frequency Decomposition

The orthonormal wavelets were introduced in Section 2.3 as a tool for multiresolution decomposition of continuous-time signals to potential applications in several fields. The wavelet transform is a mapping with superior time-frequency localization compared with the STFT.

3.5.1 Time-frequency Resolution for Wavelet Families

The time-frequency localization of the wavelet transform is distinctly different from that of the STFT. Define $\bar{t}, \bar{\Omega}$ as the centers of mass of $\psi(t)$, $\Psi(\Omega)$ on $(-\infty, \infty)$, and $[0, \infty)$ respectively. Then the RMS spreads for the prototype are

$$\begin{aligned} \sigma_\Omega^2 &= \frac{\frac{1}{\pi}\int_0^\infty (\Omega - \bar{\Omega})^2 |\Psi(\Omega)|^2 d\Omega}{E} \\ \sigma_T^2 &= \frac{\int_{-\infty}^\infty (t - \bar{t})^2 |\psi(t)|^2 dt}{E} \end{aligned} \qquad (3.33)$$

This wavelet function is centered at $\bar{t}, \bar{\Omega}$ in time-frequency plane with spreads σ_T, and σ_Ω. It follows that $\psi_{ab}(t) \leftrightarrow \Psi_{ab}(\Omega)$ is centered at $(\bar{t}_{ab}, \bar{\Omega}_{ab}) = (a\bar{t} + b, \bar{\Omega}/a)$ with

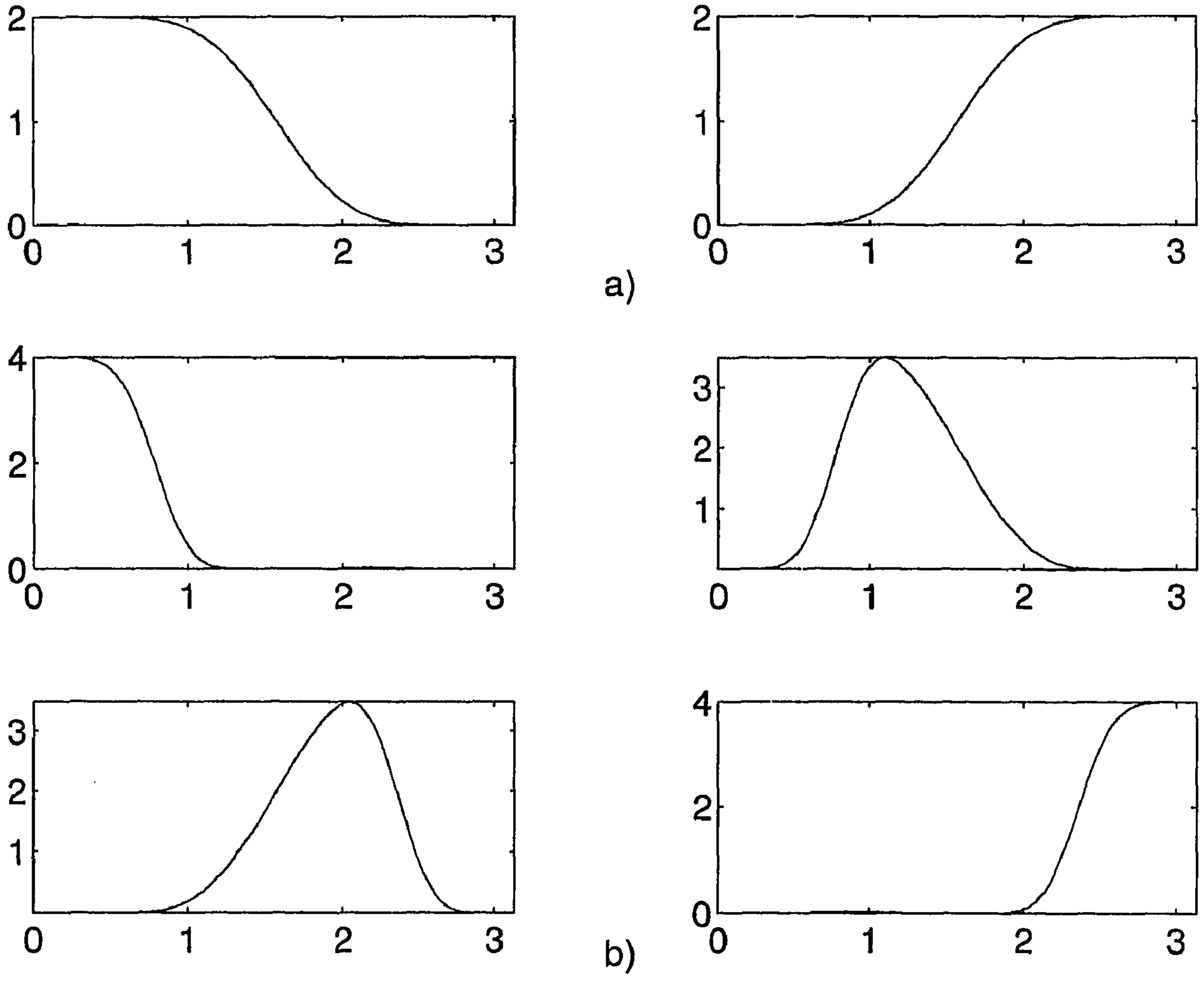

Figure 3.6 Frequency responses of (a) functions in Fig. 3.4.a and (b) functions in Fig. 3.4.b

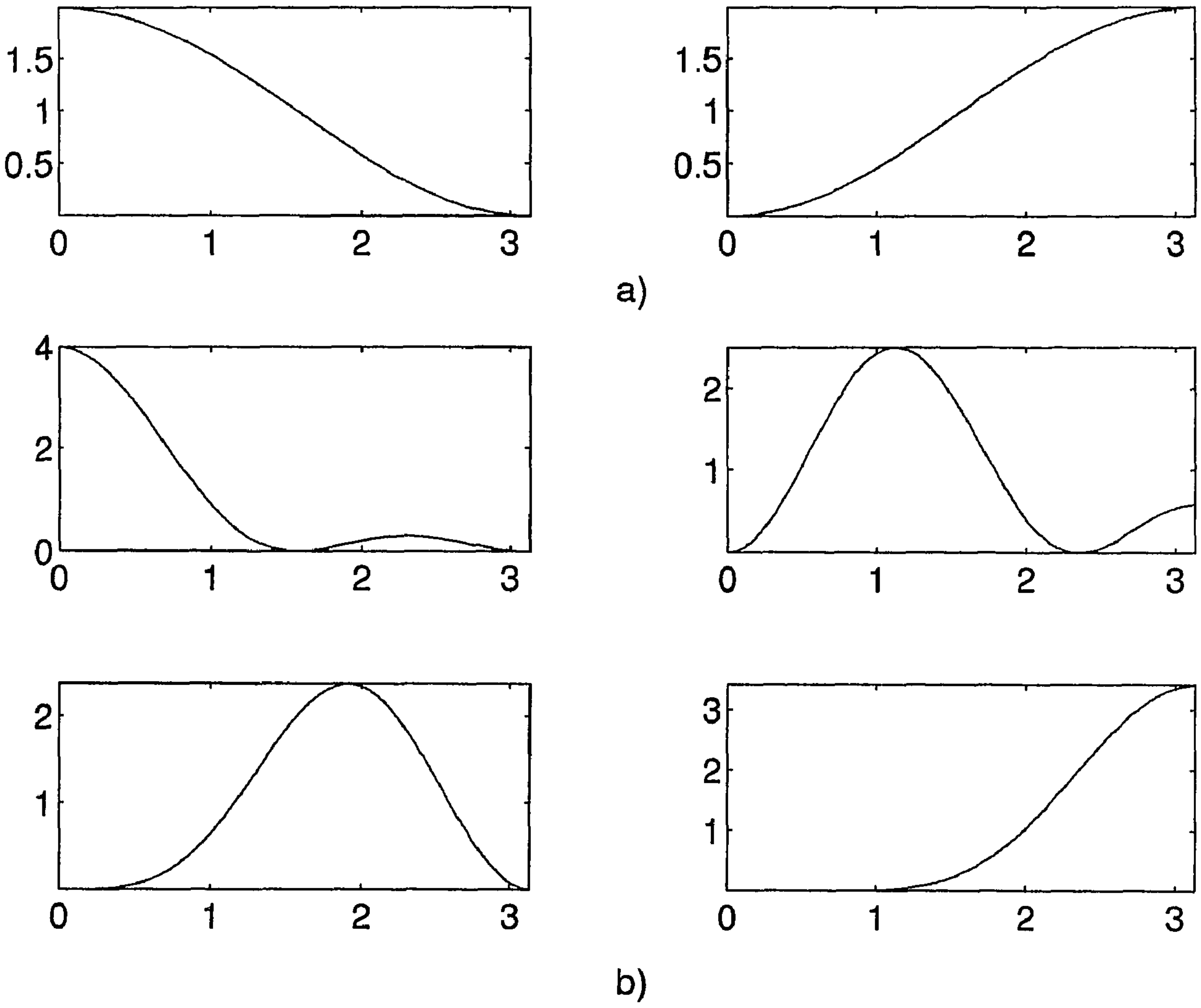

Figure 3.7 Frequency responses of (a) functions in Fig. 3.5.a and (b) functions in Fig. 3.5.b

Table 3.4 The time-frequency localizations of hierarchical subband trees for 2-level(4-band)

	$\overline{\omega}$	$\overline{n}$	σ_ω^2	σ_n^2	$\sigma_\omega^2 \times \sigma_n^2$
B-QMF Hierarchical 4 Band Tree (22 tap product filters	0	4.05	0.2526	2.7261	0.6886
	1.23	12.88	0.1222	3.8269	0.4676
	1.91	16.28	0.1222	2.7757	0.3392
	π	8.80	0.2526	2.2622	0.5714
Multiplierless (22 tap product filters)	0	7.50	0.2747	1.5817	0.4345
	1.24	11.50	0.1346	2.1683	0.2918
	1.90	13.49	0.1346	2.1675	0.2918
	π	9.50	0.2747	1.5818	0.4345
Smith-Barnwell (22 tap product filters)	0	12.45	0.2339	2.1458	0.5019
	1.22	9.88	0.1077	2.9463	0.3173
	1.92	8.45	0.1077	3.0185	0.3251
	π	11.22	0.2339	2.0772	0.4859

spread

$$\begin{aligned} \sigma_{\Omega(ab)}^2 &= \frac{1}{a^2}\sigma_\Omega^2 \\ \sigma_{t(ab)}^2 &= a^2\sigma_t^2 \end{aligned} \tag{3.34}$$

and resolution cell $\sigma_{t(ab)}\sigma_{\Omega(ab)} \geq 1/2$. Thus, the resolution, i.e. localization, in time and frequency depends on this scale parameter a. The shape of the resolution cell depends on a although the cell area is constant. This can be contrasted with the STFT which has constant shape resolution. These are shown in Fig. 3.1, and the span of these cells in the time-frequency plane is called a "tiling" of the plane.

An often quoted example of a wavelet is the second derivative of a Gaussian

$$\psi(t) = (1 - t^2)e^{-t^2/2} \leftrightarrow \Psi(\Omega) = \sqrt{2\pi}\Omega^2 e^{-\Omega^2/2}$$

This mother function has excellent localization in time and frequency and satisfies the admissibility condition. But it is not of compact support, and is not complete. For this case, we calculate $(\bar{t} = 0, \sigma_t^2 = 7/6)$, and $(\bar{\Omega} = 1.505, \sigma_\Omega^2 = 0.23646)$, resulting in a time-frequency cell $\sigma_T\sigma_\Omega = 0.525$.

Table 3.5 The time-frequency localizations of hierarchical subband trees for 3-level(8-band) cases

	$\overline{\omega}$	$\overline{n}$	σ_ω^2	σ_n^2	$\sigma_\omega^2 \times \sigma_n^2$
B-QMF Hierarchical 8 Band Tree (50 tap product filters)	0	9.12	0.0644	11.726	0.7552
	0.63	26.96	0.0490	15.953	0.7817
	1.01	34.11	0.0961	11.326	1.0884
	1.45	19.65	0.0496	9.7846	0.4853
	1.68	22.56	0.0496	10.510	0.5213
	2.13	37.99	0.0961	12.013	1.1544
	2.52	31.54	0.0490	14.950	0.7326
	π	14.36	0.0644	10.777	0.6940
Multiplierless (50-tap product filters)	0	17.53	0.0724	6.3415	0.4591
	0.64	25.46	0.0688	8.8171	0.6066
	1.02	29.46	0.1193	9.1282	1.0890
	1.45	21.54	0.0558	7.2005	0.4018
	1.68	23.47	0.0558	7.2099	0.4023
	2.11	31.53	0.1193	9.1234	1.0884
	2.50	27.54	0.0688	8.8269	0.6073
	π	19.47	0.0724	6.3371	0.4588
Smith-Barnwell (50-tap product filters)	0	28.86	0.0591	8.6494	0.5112
	0.6137	24.03	0.0321	11.837	0.3800
	0.9951	21.22	0.0688	12.623	0.8685
	1.4488	26.55	0.0436	9.5939	0.4183
	1.6927	25.32	0.0436	9.6769	0.4219
	2.1465	19.57	0.0688	12.599	0.8668
	2.5279	22.51	0.0321	11.912	0.3824
	π	27.93	0.0591	8.5379	0.5046

We have seen in Eqs.(2.47) and (2.48) that orthonormal wavelet families can be generated by any pair of two-band paraunitary filters $H_0(z)$, $H_1(z)$, with $H_0(-1) = 0$. The generation of Daubechies wavelets are given in [17]. These wavelet filters are identical to the Binomial QMF[3]. These filters have the maximally flat magnitude square responses. In [15] and [16] other wavelet families(e.g. the most regular, Coiflets) are devised by imposing other requirements on $H_0(z)$.

Table 3.6 compares the time-frequency resolutions of scaling and wavelet functions for three wavelet families generated by 6-tap paraunitary filters; the Daubechies, most regular and Coiflet, along with the localization properties of the progenitor discrete-time filters. As seen in Eq. (2.47) and Eq. (2.48), the Fourier domain equalities require infinite product terms theoretically. The localization measures in this table assumed the maximum product order of $k = 8$ in Eq. (2.47) and Eq. (2.48). It considered the frequency range of $-2^k\pi \leq \Omega \leq 2^k\pi$. Table 3.6 demonstrates that the time-frequency localizations are important measures in the evaluation of a wavelet family as an analog filter bank. In particular, the role of regularity in wavelet transforms should be evaluated for signal processing applications.

3.6 Discussions and Conclusions

In this chapter, we examined the discrete-time uncertainty principle, its measure by a resolution cell, and lower bounds for different classes of signals. We also evaluated the time-frequency resolutions of some known orthogonal signal decomposition techniques; block transforms, lapped orthogonal transforms, subband filter banks and wavelets.

Historically, the design of transform bases and filter banks has emphasized either the time or frequency domain with orthogonality as their main feature. It is well observed and understood in visual signal processing and coding applications

Table 3.6 Time-frequency localizations of 6-tap wavelet filters, and corresponding scaling and wavelet functions

		Daubechies[19][21]	Mostregular[29]	Coiflet[27]
Scaling Function	σ_T^2	0.134	0.143	0.086
	σ_Ω^2	5.22	5.77	11.86
	$\sigma_T^2\sigma_\Omega^2$	0.699	0.825	1.02
Wavelet Function	σ_T^2	0.178	0.188	0.108
	σ_Ω^2	8.97	11.70	39.36
	$\sigma_T^2\sigma_\Omega^2$	1.596	2.199	4.25
Low-Pass PR-QMF	σ_n^2	0.453	0.470	0.305
	σ_ω^2	0.987	0.996	1.059
High-Pass PR-QMF	σ_n^2	0.453	0.470	0.305
	σ_ω^2	0.987	0.996	1.059

that the behavior of transform basis or filters should be monitored jointly in time and frequency domains. It is expected that this point will be considered in the future designs.

The FIR two-band orthonormal filter banks have a vital role as the inter-scale coefficients in the design of compactly supported orthonormal wavelet transform bases. The wavelet theory emphasizes the differentiability or regularity property of the basis functions in the design. Wavelet regularity implies a flat frequency response for the wavelet filters at $\omega = 0$ and $\omega = \pi$. In Table 6, the time and frequency localizations of wavelet filters along with the corresponding wavelet and scaling functions were evaluated for three different families proposed by Daubechies. In addition to the regularity measure, new performance measures may be needed in the design of wavelet bases for signal processing applications.

The transform bases or filter banks consist of a set of functions. The inter-band leakage or overlapping of frequency functions should also be considered in the design. This means a good localization at the desired region of time-frequency plane for all the functions in the basis.

We conclude that the overlapping transform basis or filter bank design has significantly more degrees of freedom than has been utilized. We expect more flexible basis designs in the future for more efficient spectral decomposition of signal sources.

CHAPTER 4

SUBSPECTRAL MODELING IN FILTER BANKS

4.1 Introduction

The popular linear transform techniques, block transforms and subband filter banks, have been successfully used for spectral decomposition. The generalized linear transform (GLT) theory has matured and well established [2][40]. This general approach provides non-overlapping and overlapping block transform bases with multiresolution properties. In addition, the unequal bandwidth basis solutions are shown to be feasible. Therefore, the current trend in decomposition field is to search the best transform basis for the given input signal statistics. The subband structuring (time-frequency tiling) along with the optimal basis design techniques, provide the mathematical tools for spectral decomposition .

The spectral analysis and modeling has found its applications in many diverse areas like speech coding to forecasting. The recent advances in the GLT theory have opened new avenues for the joint treatment of the signal decomposition, spectral analysis and modeling problems. We attempt to assess the merits of subspectral modeling over the conventional modeling techniques which utilize the full spectrum.

The basic idea here is to split the signal spectrum into its subspectra based on certain criteria, and model them individually rather than modeling the full spectrum. It is shown that the subband or sub-interval modeling is superior to the full interval modeling of the spectrum.

Linear predictive(LPC) modeling technique has been widely used particularly for low bit-rate speech coding and synthesis [7][14]. There have been contradicting reports in the literature on the practical merits of subband LPC modeling, coding. We also address that problem in this chapter as the special case of the general topic studied. We will show that performance improvement is possible in subspectral LPC modeling over full spectrum. We give the possible reasonings why the earlier studies on subband LPC were not performing satisfactorily and contradicting to the expectations.

The idea of selective linear prediction of speech was first mentioned by Makhoul[26]. Later, subspectral modeling was studied by Roberts, and Wiggins [33]. It was reported in [7] that the subband LPC was not superior to the conventional case for speech coding applications. On the other hand, Ref. [14] reports that subband LPC provided a better coding performance than the full band case in their experiments. All of these studies were mainly experimental. More recently, Rao and Pearlman [32] have addressed some aspects of the problem.

We will, therefore, attempt to jointly treat the spectral decomposition and modeling steps and provide the theoretical reasonings for the experimental observations.

4.2 Statistical Source Modeling

Parametric modeling has been found to be an attractive method for the representation of signals. Among the widely used models, the moving average (MA), the autoregressive (AR), and the autoregressive-moving average (ARMA) models have been the most popular ones [23]. In all of these models, a signal $x(n)$ is assumed to be generated by exciting a filter $h(n)$ with white noise sequence $u(n)$ as

$$X(z) = U(z)H(z) \tag{4.1}$$

where $X(z)$, $U(z)$, and $H(z)$ are the z-transforms of $x(n)$, $u(n)$, and $h(n)$, respectively.

More specifically, in the case where $x(n)$ is an MA signal, the transfer function $H_{MA}(z)$ of $h_{MA}(n)$ is given by

$$H_{MA}(z) = B(z) = \sum_{k=0}^{q} b_k z^{-k} \tag{4.2}$$

where q is the filter order, and $b_0 = 1$. Clearly, $h_{MA}(n)$ is an FIR filter. We call $x(n)$ an MA(q) process. In the time domain, $x(n)$ is written as

$$x(n) = \sum_{k=0}^{q} b_k u(n-k) \tag{4.3}$$

When $x(n)$ is an AR signal, the spectral shaping filter used has a transfer function $H_{AR}(z)$ given by

$$H_{AR}(z) = \frac{1}{A(z)} = \frac{1}{1 + \sum_{k=1}^{p} a_k z^{-k}} \tag{4.4}$$

where p is the order of filter. It is assumed stable, since $h_{AR}(n)$ is an IIR filter. We call $x(n)$ as an $AR(p)$ process. Similarly, $x(n)$ is written in the time domain as

$$x(n) = -\sum_{k=0}^{p} a_k x(n-k) + u(n) \tag{4.5}$$

where $a_0 = 1$. Last, in ARMA modeling which is a combination of both AR and MA models, we find $H_{ARMA}(z)$ expressed as

$$H_{ARMA}(z) = \frac{B(z)}{A(z)} = \frac{\sum_{k=0}^{q} b_k z^{-k}}{1 + \sum_{k=1}^{p} a_k z^{-k}} \tag{4.6}$$

This one is also an IIR filter which is assumed to be stable. $x(n)$ is referred to be an $ARMA(p,q)$ process. In this case, $x(n)$ is written as

$$x(n) = -\sum_{k=0}^{q} a_k x(n-k) + \sum_{k=0}^{q} b_k u(n-k) \tag{4.7}$$

4.3 Relationships Among Model Parameters

For a given AR, MA, or ARMA model of a finite order, it is possible to express it in terms of the other two . For instance, an MA or ARMA process can be represented by a unique AR model of infinite order. Particularly for ARMA to AR transformation, we derive the relationship between an ARMA with finite parameters and its AR counterpart. For ARMA, we know that

$$H(z) = \frac{B(z)}{A(z)} = \frac{\sum_{k=0}^{q} b_k z^{-k}}{1 + \sum_{k=1}^{p} a_k z^{-k}} \tag{4.8}$$

Let

$$C(z) = 1 + \sum_{k=1}^{\infty} c_k z^{-k} \tag{4.9}$$

be the $AR(\infty)$ model. Therefore , we can rewrite Eq. (4.8) as

$$H(z) = \frac{B(z)}{A(z)} = \frac{1}{C(z)} \tag{4.10}$$

The sequence $\{c(n)\}$ where n goes from 0 to ∞ is easily obtained in a recursive manner as

$$c(n) = -\sum_{k=1}^{q} b_k c(n-k) + \sum_{k=0}^{p} a_k \delta(n-k) \tag{4.11}$$

where $\delta(n)$ is the Kronecker delta. This infinite series will converge if the zeros of $B(z)$ are inside the unit circle. In other words, for this series to converge, $H(z)$ will be assumed minimum phase. $H(z)$ will then be both stable and invertible.

4.4 Effects of Multirate Operators on Spectral Modeling

In this work, we study the modeling problem in a multirate environment and investigate the effects of multirate processing on modeling. We assume that our input $x(n)$ to be an $AR(p)$ process. Its power spectrum (PS) is given by

$$S_X(z) = \frac{1}{A(z)A(z^{-1})} \tag{4.12}$$

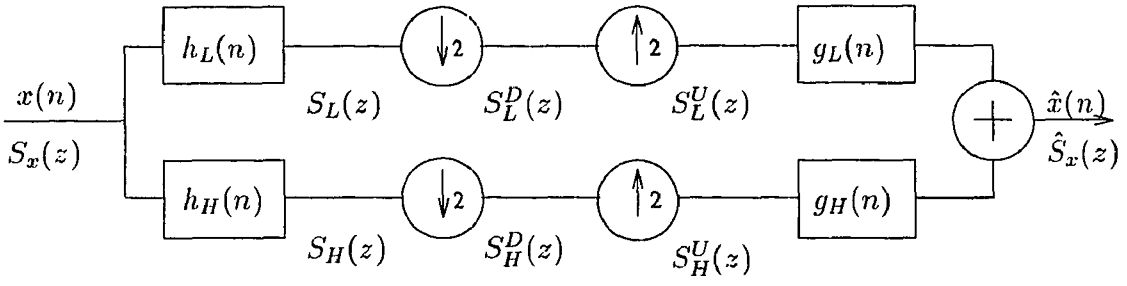

Figure 4.1 A generic two-band filter bank structure

where $A(z) = 1 + \sum_{k=1}^{p} a_k z^{-k}$. We study the two-band subband structure given in Fig. 4.1 This structure decomposes a signal into two subband signals by passing it through a lowpass and a highpass filters. The subband signals are downsampled to satisfy Nyquist rate requirement before any processing (modeling, coding). At the receiver side, each of the downsampled subband signals is upsampled and further processed by interpolation filters before the summation at the output. The filters are chosen in such a way that aliasing and imaging distortions introduced by the downsamplers and upsamplers, respectively, are removed, resulting in a perfect reconstruction of the original signal.

The operators used in a multirate or filter bank structure are displayed individually in Fig. 4.2

4.4.1 Effects of Filtering

The filter output in Fig. 4.2.a is expressed as $y(n) = x(n) * b(n)$ where * stands for linear convolution. $B(z)$ is assumed to be an FIR . The power spectrum density of the process $y(n)$ is easily expressed as

$$S_Y(z) = \frac{B(z)B(z^{-1})}{A(z)A(z^{-1})} \tag{4.13}$$

The output $Y(z)$ is an $ARMA(p,q)$ process. $B(z)$ may be any one of the spectral splitting or anti-aliasing filters and $Y(z)$ is its output.

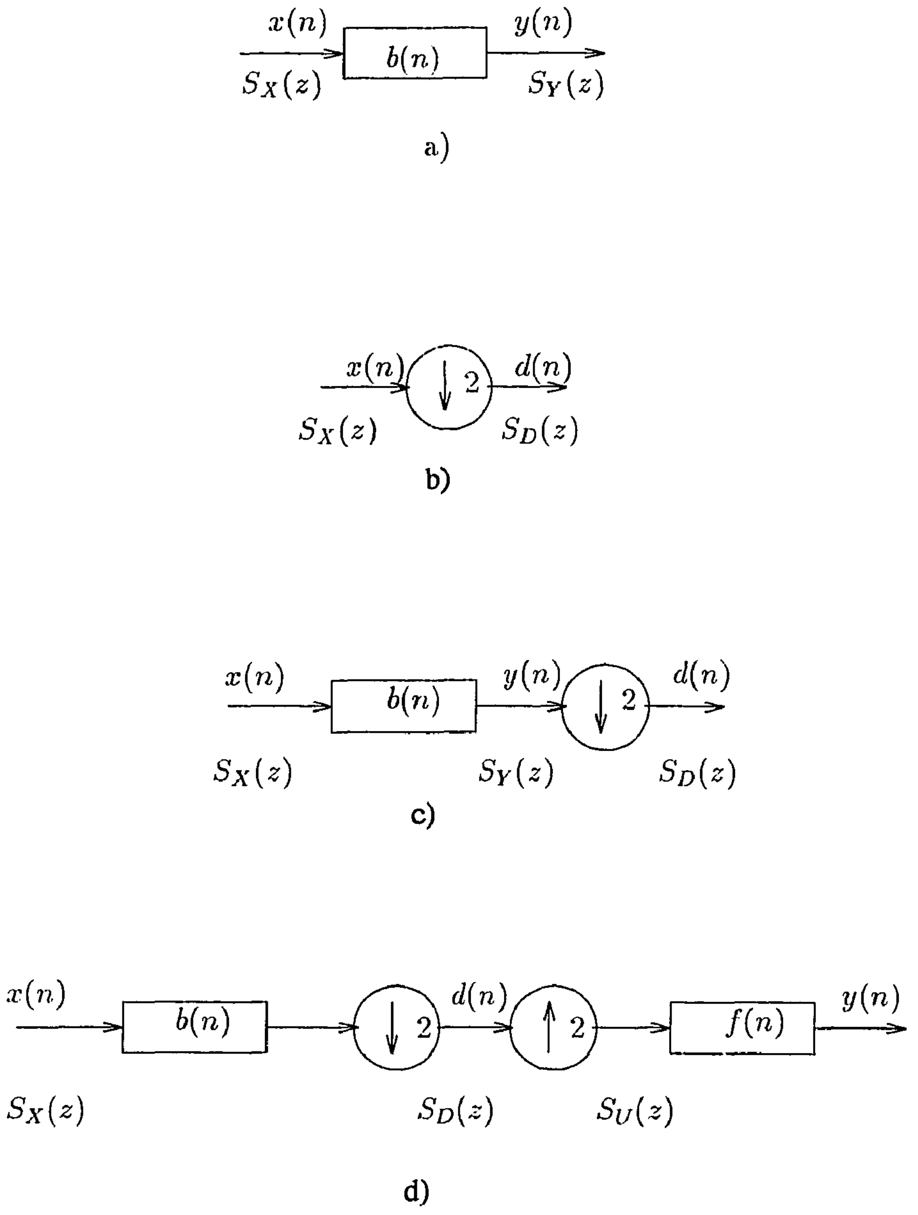

Figure 4.2 Some typical interconnections analyzed

4.4.2 Effects of Downsampling

$x(n)$ is an input to the downsampler as given in Fig. 4.2.b. The output $d(n)$ of the downsampler has a PS given as

$$S_D(z) = \frac{1}{2}\left[S_x(z^{\frac{1}{2}}) + S_x(-z^{\frac{1}{2}})\right] \tag{4.14}$$

Let us now expand the above equation to find out what kind of process $d(n)$ is. $A(z)$ can be written in a factorizable form as

$$A(z) = \prod_{k=1}^{p}(1 - p_k z^{-1}) \tag{4.15}$$

where p_ks are the zeros of $A(z)$. Therefore, $S_D(z)$ is expressed as

$$S_D(z) = \frac{1}{2}\left[\frac{1}{\prod_{k=1}^{p}(1 - p_k Z^{-1})(1 - p_k Z)} + \frac{1}{\prod_{k=1}^{p}(1 + p_k Z^{-1})(1 + p_k Z)}\right] \tag{4.16}$$

where $Z = z^{\frac{1}{2}}$. We can rewrite Eq. (4.16) as

$$S_D(z) = \frac{1}{2}\left[\frac{\prod_{k=1}^{p}(1 + p_k Z^{-1})(1 + p_k Z) + \prod_{k=1}^{p}(1 - p_k Z^{-1})(1 - p_k Z)}{\prod_{k=1}^{p}(1 - p_k Z^{-1})(1 - p_k Z)(1 + p_k Z^{-1})(1 + p_k Z)}\right] \tag{4.17}$$

We notice that the numerator in Eq. (4.17) is a polynomial in degree $[\frac{p}{2}]$ and the denominator is a polynomial in degree p. [x] stands for the integer part of x. Thus, the output $D(z)$ in Fig. 4.2.b is an $ARMA(p, [\frac{p}{2}])$ process.

4.4.3 Effects of Decimation

The combination of anti-aliasing filtering and downsampling is called the decimation operation. $y(n)$ is the input to the decimator as seen in Fig. 4.2.c. In this case, the output $d(n)$ of the decimator has a PS given as

$$\begin{aligned} S_D(z) &= \frac{1}{2}\left[S_Y(z^{\frac{1}{2}}) + S_Y(-z^{\frac{1}{2}})\right] \\ S_D(z) &= \frac{1}{2}\left[S_X(z^{\frac{1}{2}})S_B(z^{\frac{1}{2}}) + S_X(-z^{\frac{1}{2}})S_B(-z^{\frac{1}{2}})\right] \end{aligned} \tag{4.18}$$

We will expand the above equation again to find out what kind of process $d(n)$ is. The filter function $B(z)$ can be written in a factorizable form as

$$B(z) = \prod_{k=1}^{q}(1 - z_k z^{-1}) \tag{4.19}$$

where $z_k s$ are the zeros of polynomial $B(z)$. Therefore, $S_D(z)$ is expressed as

$$S_D(z) = \frac{1}{2}\left[\frac{\prod_{k=1}^{q}(1 - z_k Z^{-1})(1 - z_k Z)}{\prod_{k=1}^{p}(1 - p_k Z^{-1})(1 - p_k Z)} + \frac{\prod_{k=1}^{q}(1 + z_k Z^{-1})(1 + z_k Z)}{\prod_{k=1}^{p}(1 + p_k Z^{-1})(1 + p_k Z)}\right] \tag{4.20}$$

where $Z = z^{\frac{1}{2}}$. We can rewrite Eq. (4.20) as

$$S_D(z) = \frac{1}{2}\frac{P(z)}{Q(z)} \tag{4.21}$$

where the numerator and denominator polynomials are given as

$$\begin{aligned} P(z) &= \prod_{k=1}^{p}(1 + p_k Z^{-1})(1 + p_k Z)\prod_{k=1}^{q}(1 - z_k Z^{-1})(1 - z_k Z) + \\ &\quad \prod_{k=1}^{p}(1 - p_k Z^{-1})(1 - p_k Z)\prod_{k=1}^{q}(1 + z_k Z^{-1})(1 + z_k Z) \end{aligned} \tag{4.22}$$

$$Q(z) = \prod_{k=1}^{p}(1 - p_k Z^{-1})(1 - p_k Z)(1 + p_k Z^{-1})(1 + p_k Z) \tag{4.23}$$

We notice that the numerator is a polynomial in degree $[\frac{p+q}{2}]$ and the denominator is a polynomial in degree p. [x] stands for the integer part. Thus, $D(z)$ is an $ARMA(p, [\frac{p+q}{2}])$ process. If $B(z)$ is one of the splitting filters in the filter bank, and is a good $\pi/2$ filter, $Y(z)$ is essentially similar to an $AR(p')$ where $p\prime < p$. The intuition behind the smaller order is that the effects of any poles located in $[\pi/2, \pi]$ interval are negligible. Thus, the signal can be represented by a smaller number of poles.

4.4.4 Effects of Upsampling

Taking the output of the decimator as input to the upsampler as seen in Fig. 4.2.d., we can easily trace the combined effects of the upsampler and the interpolation filter on the spectrum. The input and output spectra of the upsampler are related as[28]

$$S_U(z) = \frac{1}{2} S_D(z^2) \tag{4.24}$$

Hence, the spectrum at the output of the interpolation filter becomes

$$S_Y(z) = \frac{1}{4}\frac{P(z)}{Q(z)} F(z)F(z^{-1}) \tag{4.25}$$

where

$$\begin{aligned} P(z) \; = \; & \prod_{k=1}^{p}(1 + p_k z^{-1})(1 + p_k z) \prod_{k=1}^{q}(1 - z_k z^{-1})(1 - z_k z) + \\ & \prod_{k=1}^{p}(1 - p_k z^{-1})(1 - p_k z) \prod_{k=1}^{q}(1 + z_k z^{-1})(1 + z_k z) \end{aligned} \tag{4.26}$$

$$Q(z) = \prod_{k=1}^{p}(1 - p_k z^{-1})(1 - p_k z)(1 + p_k z^{-1})(1 + p_k z) \tag{4.27}$$

We see that the spectrum at the output of the interpolation filter is an $ARMA(2p, p + 2q)$ process.

4.4.5 AR(1) Source Case

If an $AR(1)$ process is assumed as input to the filter bank, we can easily trace the spectral changes through a typical branch of the filter bank. Therefore, the spectra at different points of the branch are as follows:

1. The input is an $AR(1)$ process.
2. The spectrum at the output of the analysis filter is therefore an $ARMA(1, 3)$ process if a four-tap filter is used.

3. The output of the downsampler can be shown to be an $ARMA(1,2)$ process.
4. The spectrum of the output of the branch can be shown to be $ARMA(2,7)$ with the assumption of a four-tap interpolation filter used for example the Binomial-QMF.

4.5 Performance Analysis of Subspectral Modeling

Autoregressive modeling of signals is often used because it is easily implementable and fairly understood. We give the theoretical setting of AR modeling performance in general and specify it to the sub-spectral configuration.

4.5.1 AR Modeling and Error Analysis

A signal can be expressed as a linear combination of its previous samples in AR modeling as

$$x(n) = -\sum_{k=1}^{p} a_k x(n-k) + u(n) \tag{4.28}$$

where $\{a_i\}$ are the prediction coefficients and $\{u(n)\}$ is the prediction error signal. There are several efficient algorithms to calculate AR model parameters $\{a_i\}$, based on the measured statistics of a given signal. The relations between $\{a_i\}$ and input correlation sequence $R_{XX}(m)$ are found as

$$\sum_{k=1}^{p} a_k R_{XX}(\mid i-k \mid) = -R_{XX}(i) \qquad 1 \leq i \leq p \tag{4.29}$$

Eq. (4.29) implies a set of p linear equations in p unknowns. The minimum prediction error employing $\{a_i\}$ is found as[26]

$$E^p = R_{XX}(0) + \sum_{k=1}^{p} a_k R_{XX}(k) \tag{4.30}$$

4.5.2 Discussions on Error Performance

It is readily seen from Eq. (4.30) that the modeling performance depends on the spectrum of the signal. We would like to compare the performance of modeling at various points of the filter bank. Fig. 4.5 displays the AR modeling performance for several input sources. These inputs were chosen to have different statistical features. Fig. 4.3 and Fig. 4.4 illustrate the power spectral density of two pure AR and ARMA processes along with those of two sample speech frames.

For comparison purposes, ARMA modeling errors are also included in Table 4.1. It is observed from Fig. 4.5 and Table 4.1 that AR and ARMA techniques perform comparably for the given cases. It is clear that the subspectral modeling before the rate change, using either technique, significantly outperforms both the full spectrum case and the one after the rate change. This is due to the following facts. First, the superiority of subspectral modeling over full spectrum is attributed to the fact that each portion of the spectrum is approximated by an independent model (piecewise approximation). Thus, the whole spectrum is fitted better and smaller modeling errors are obtained. Second, the superiority of subspectral modeling before rate change over the one after rate change is due to the fact that the decimation operation distorts the spectrum by introducing aliasing components in the subband signals [2]. More interestingly, subspectral modeling error after the rate change was found to be comparable or inferior to the full spectrum case depending on the input source. Therefore, the subband modeling is not justified theoretically for the experiments performed in this study. The results suggest that performance improvements are possible if the subspectral modeling is done before the downsampler.

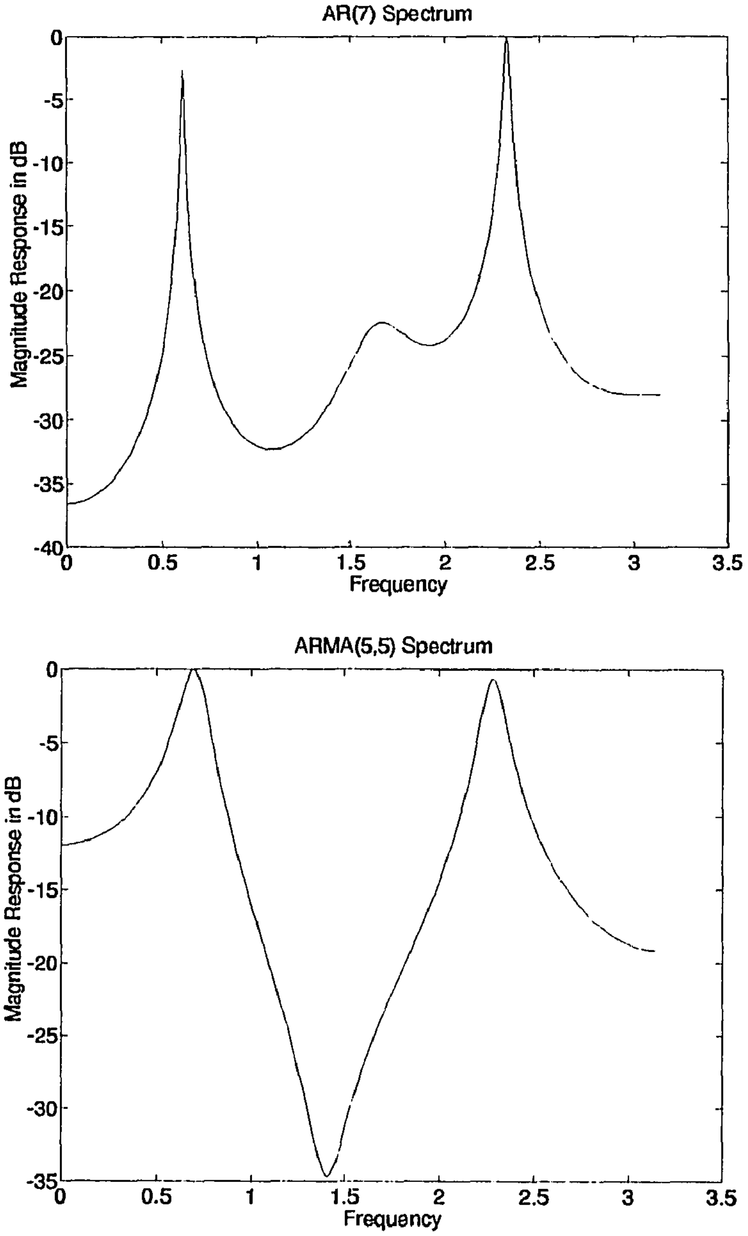

Figure 4.3 Power spectral density of $AR(7)$ and $ARMA(5,5)$ sources

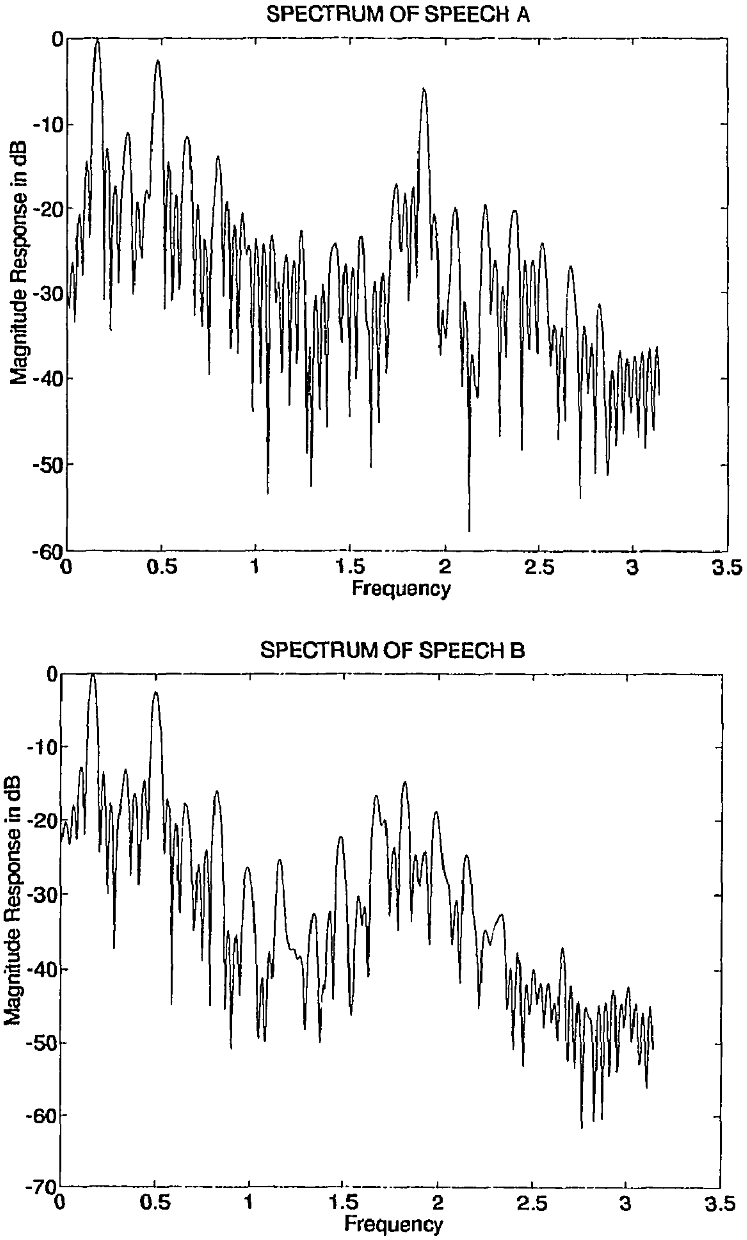

Figure 4.4 Power spectral density of two sample speech frames

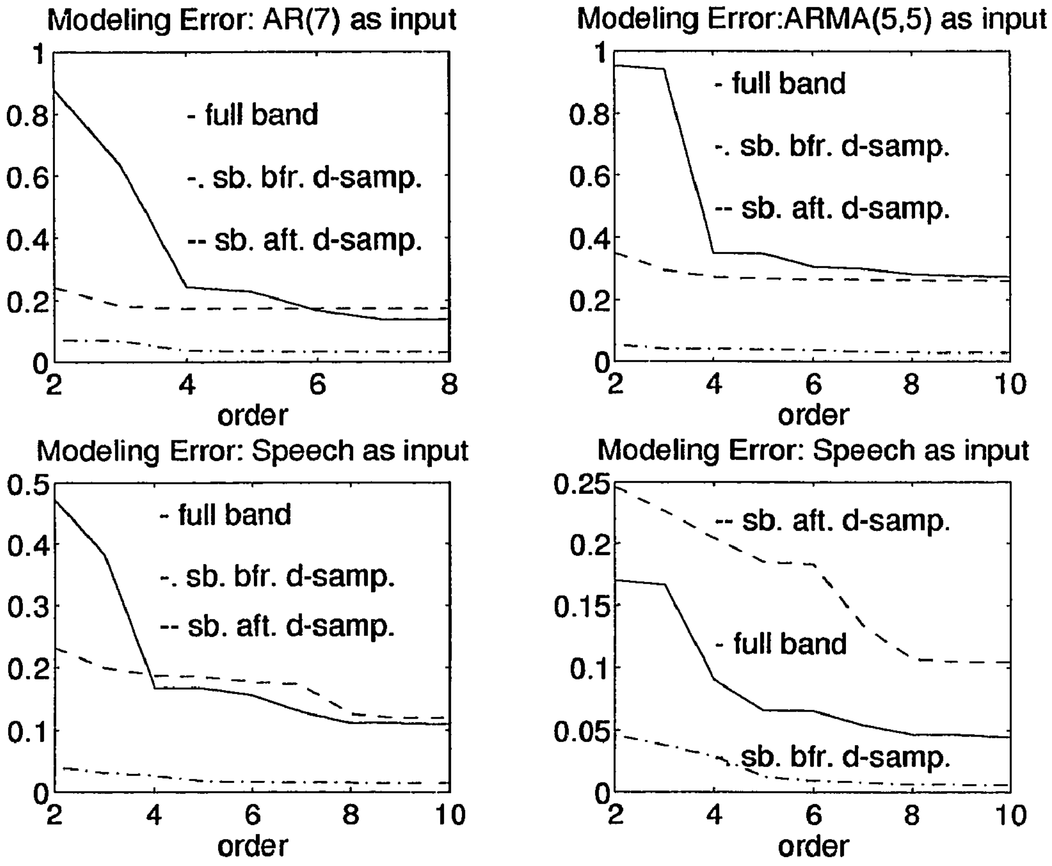

Figure 4.5 Prediction error in subbands vs. order p

Table 4.1 ARMA modeling error performance for different input sources

Input Source	Order (p+q)	Full Band	Subband Before Downsampler	Subband After Downsampler
$AR(7)$	8	0.1378	0.0522	0.1818
$ARMA(5,5)$	10	0.2577	0.0387	0.2649
Speech A	10	0.1094	0.0144	0.1749
Speech B	10	0.0422	0.0088	0.1051

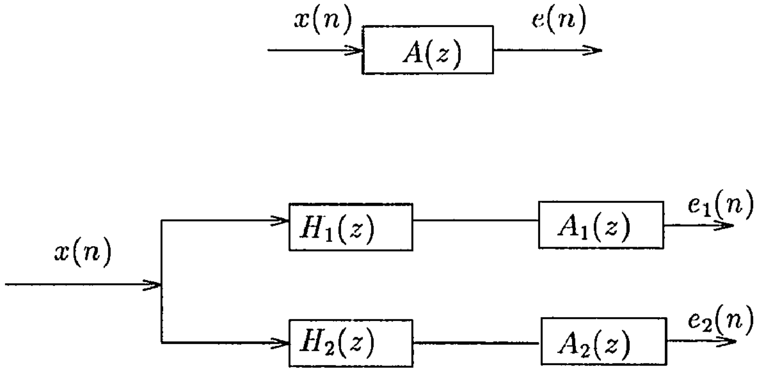

Figure 4.6 Pertaining to the proof

4.6 A Simple Proof of Performance Improvement in Subspectral Modeling

Let $x(n)$ be the process to be modeled as an AR. $A(z)$, the modeling filter, is such that Err is minimum as depicted in Fig. 4.6. The modeling error is calculated as

$$\begin{aligned} Err &= \sum_{k=0}^{N-1} e^2(n) = \frac{1}{2\pi}\int_{-\pi}^{\pi} \mid E(\omega) \mid^2 d\omega \\ Err &= \frac{1}{2\pi}\int_{-\pi}^{\pi} \mid A(\omega) \mid^2 \mid X(\omega) \mid^2 d\omega \end{aligned} \quad (4.31)$$

Assume that $x(n)$ is split into two equal bands in the frequency domain. With the same token, $A_1(z)$, the model of band 1, is such that the modeling error $Err1$ is minimum , where

$$\begin{aligned} Err1 &= \sum_{k=0}^{N-1} e_1^2(n) = \frac{1}{2\pi}\int_{-\pi}^{\pi} \mid E_1(\omega) \mid^2 d\omega \\ &= \frac{1}{2\pi}\int_{-\pi}^{\pi} \mid A_1(\omega) \mid^2 \mid H_1(\omega) \mid^2 \mid X(\omega) \mid^2 d\omega \end{aligned} \quad (4.32)$$

Similarly, $A_2(z)$, the model of band 2, is such that $Err2$ is minimized , where

$$Err2 = \sum_{k=0}^{N-1} e_2^2(n) = \frac{1}{2\pi}\int_{-\pi}^{\pi} \mid E_2(\omega) \mid^2 d\omega$$

$$= \frac{1}{2\pi}\int_{-\pi}^{\pi} \mid A_2(\omega) \mid^2 \mid H_2(\omega) \mid^2 \mid X(\omega) \mid^2 d\omega \tag{4.33}$$

If the filters $H_1(z)$ and $H_2(z)$ are power complementary, such that

$$\mid H_1(\omega) \mid^2 + \mid H_2(\omega) \mid^2 = 1 \tag{4.34}$$

we can write the total modeling error Err of the system as

$$\begin{aligned} Err &= \frac{1}{2\pi}\int_{-\pi}^{\pi} \mid A(\omega) \mid^2 (\mid H_1(\omega) \mid^2 + \mid H_2(\omega) \mid^2) \mid X(\omega) \mid^2 d\omega \\ Err &= \frac{1}{2\pi}\int_{-\pi}^{\pi} \mid A(\omega) \mid^2 \mid H_1(\omega) \mid^2 \mid X(\omega) \mid^2 d\omega + \frac{1}{2\pi}\int_{-\pi}^{\pi} \mid A(\omega) \mid^2 \mid H_2(\omega) \mid^2) \mid X(\omega) \mid^2 d\omega \\ Err &= E_a + E_b \end{aligned} \tag{4.35}$$

For each band, there is a unique modeling filter that leads to a minimum error for a given order. Since $A_1(z)$ is unique for $x_1(n)$, any other filter used will give a higher modeling error. Therefore, it is clear that E_a is greater than $Err1$. Similarly, we conclude that E_b is also greater than $Err2$. This implies then that always $Err > Err_1 + Err_2$.

4.7 Subspectral CELP Speech Coding and Performance Comparisons

One of the widely used applications of AR modeling is LPC based speech coding. In this case, speech sequence is subdivided into frames of 160 – 200 samples at the sampling rate of 8 KHz. Then AR modeling or LPC analysis is performed on each frame. The AR coefficients along with the residual modeling error are encoded and transmitted to the decoder. The AR coefficients or LPC parameters are not quantized directly since their quantization may not always lead to a stable filter. Additionally, the quantization effects on the shape of the spectrum are of practical concern. Instead, an alternative set of parameters called line spectral pairs (LSP) or line spectral frequencies (LSF) are used to encode $\{a_i\}$ coefficients. The LSFs exhibit nice intrinsic properties which permits efficient coding of LPC coefficients [19],[36]. The LSPs are the roots of the sum and difference filters given by

$$P_{n+1}(z) = A_n(z) + z^{-(n+1)}A_n(z^{-1}). \quad \textit{Sum filter} \tag{4.36}$$

$$Q_{n+1}(z) = A_n(z) - z^{-(n+1)}A_n(z^{-1}). \quad \textit{Difference filter} \tag{4.37}$$

where n is the order of prediction filter $A(z)$.

These filters have their zeros on the unit circle (UC). Thus, only the phase of these roots has to be computed. The polynomials $P(z)$ and $Q(z)$ have extraneous roots at $z = 1$ and $z = -1$, respectively. Therefore, each filter has $n/2$ root pairs. The roots of $P(z)$ and $Q(z)$ are ordered on UC and interlaced with each other. These properties are exploited in order to have an efficient coding. After quantization of LSP coefficients, the reconstructed filter $A_n^q(z)$ retains its stability. The reconstructed filter is expressed as

$$A_n^q(z) = 0.5 \times (P_{n+1}^q(z) + Q_{n+1}^q(z)). \tag{4.38}$$

In this study, we used a prediction order $n = 10$. Let vector $\underline{\omega}^T = [\omega_1, \omega_2, ..., \omega_{10}]$ represents these LSPs frequencies. An efficient vector quantization (VQ) procedure has been devised by Paliwal and Atal[29]. The full range of $\underline{\omega}^T$ is partitioned in two parts, $\underline{\omega}_a$ and $\underline{\omega}_b$. The size of each of these vectors is 4 and 6 respectively. Each of these sub-vectors is quantized separately. In subband LPC coding application, for the two-band filter bank example, the $\{a_i^L\}$ and $\{a_i^H\}$, the low and high band LPC parameters, respectively, are mapped into LSP domain for quantization purposes. In this application, the full range of $\underline{\omega}_L^T$ and $\underline{\omega}_H^T$ is not partitioned in two parts. It is worth mentioning that the particular partitioning of the vector $\underline{\omega}^T$ used in this work lends itself to $\pi/2$ subspectral decomposition. The reason behind this is that statistics have shown that more than 99 % of LSF vectors of order 10 have their first 4 LSF's confined to the interval 0 to $\pi/2$.

Code Excited Linear Predictive (CELP) coder has been found to be the leading candidate for relatively high quality speech compression that will transmit speech in the range of $4800 - 9600$ $bits/sec$ with an acceptable level of complexity[6]. The basic approach in this coder is to use time-varying predictive filters to model the correlation between speech samples . To do that, the digitized speech signal $s(n)$ is filtered using a short-time predictor to extract the formants (LPC) coefficients or vocal tract information. The coefficients are quantized and used for the prediction of the signal. The signal that remains after removal of the correlation between adjacent samples is further filtered using a long-time predictor to extract the pitch information and thus removal of the correlation between adjacent pitch periods. The pitch data composed of the pitch lag and the pitch prediction coefficient are also quantized and used for predictive filtering of the signal. The transmitted information consists of quantized filter parameters (side information), gain term, and the quantized residual samples from the filters (residual information). This remaining information is modeled by samples drawn form a stochastic codebook such that the resulting synthetic signal is a close replica to the original speech signal. Fig. 4.7.a shows the basic structure of the coder.

The codebook contains N excitation vectors. The selection of the best excitation vector is performed by a full search procedure through the codebook using a weighted mean square error criterion. Each excitation vector is scaled by a gain factor g_i and passed through the long and short time filters, to restore the pitch and the vocal tract information, respectively. The resulting signal $x_i(n)$ is then used in computing the optimal gain term g_i for that vector and the resulting error $e_i(n)$. the index of the vector codeword and the quantized scalar gain corresponding to the minimum distortion d_i are transmitted to the receiver.

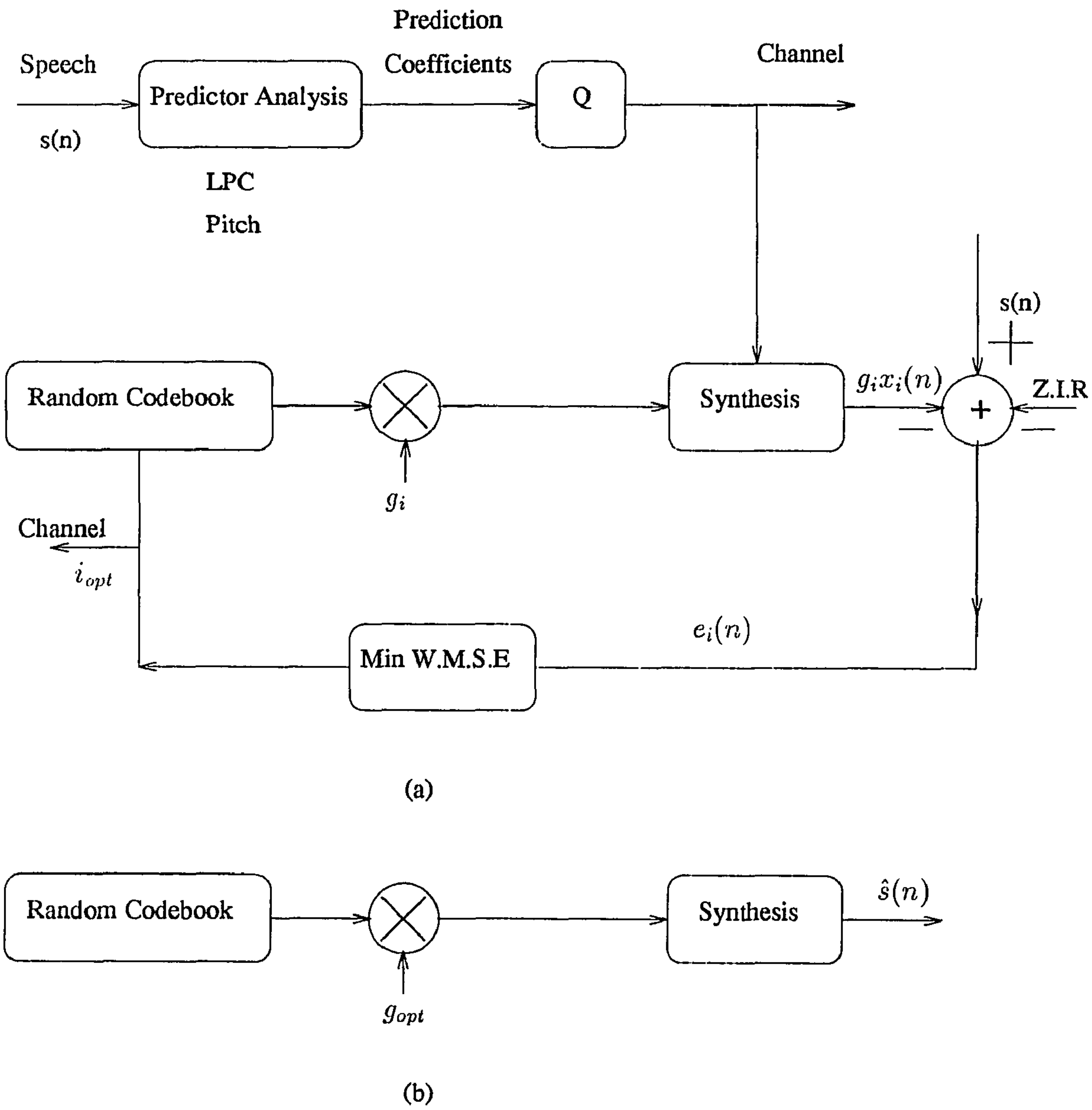

(a)

(b)

Figure 4.7 a) CELP coder, b) decoder

Table 4.2 CELP SNR (dB) performance at 4.8 Kb/sec for different schemes

Speaker	Full Band	Subband without Downsampler			Subband with Downsampler		
		Lowpass	Highpass	overall	Lowpass	Highpass	overall
Male	10.07	9.25	3.30	8.94	9.71	3.15	9.12
Female	8.73	8.54	3.82	8.37	8.40	4.04	8.05

At the receiver end, the decoder simply multiplies the excitation vector by an appropriate gain and passes the resulting signal through the synthesis filters to generate the replica of the original speech. Illustration of the CELP decoder appears in Fig. 4.7.b.

To assess the benefits of subband modeling, we embedded a two-band filter bank within the CELP structure. Several simulations, running at 4.8 Kb/sec, were conducted using the CELP coding approach. The first one used no filter bank decomposition. The second and third simulations had 2 band-split configuration being incorporated in the CELP structure with/without downsamplers respectively. The SNR results between the original speech and the coded one are tabulated below for both a male and a female speakers. As it can be seen, the CELP algorithm performs better in terms of SNR for the fullband than for either type of the two band scheme. However, listening tests revealed no preference is given to anyone of them. In other words, all of them exhibited a comparable speech quality. It should be noticed that CELP favors low frequencies to the high ones. This is expected, since high frequency signals exhibit low correlation between the samples.

4.8 Conclusions

We presented a joint treatment of spectral decomposition and modeling problems in this chapter. A complete analysis of the subspectral modeling problem is given. The performance of subspectral modeling and the conventional modeling approaches are compared. It is shown that subspectral modeling provides significant performance improvements if used carefully. The proposed approach was tested for several signals, including speech signals, and is shown to follow the theoretical results. It is expected that the combination of spectral decomposition and modeling steps will open new avenues for better treatment of many signal processing problems. However, when subband modeling was combined with coding of speech namely CELP technique, it was found that no real gain was obtained. The improvements in this scenario are shown to be quite random. Therefore, this study explains the reasons of conflicting performance results with subband LPC based speech coders reported in the literature.

CHAPTER 5

SUBBAND IMAGE CODING

5.1 Introduction

In the last two decades or so, tremendous research activities were geared toward the area of image compression. The main reasons for this are the high demand for transmission of pictorial information using digital computers and the rapid deployment of digital transmission facilities. Image compression has found many areas of applications. Among these, there is the recent emerging video-telephone technology and teleconferencing. Also of great commercial interest is the high quality coding of broadcast television namely High Television (HDTV). Besides these, transmission and storage of medical images and archives just to name a few make use of image compression technologies for efficient handling of the data.

A vast myriad of compression algorithms were developed to meet the bandwidth constraints required for potential transmission of digital pictures. From a simple differential pulse code modulation (DPCM) coder that provides acceptable coding quality at bit rate slightly below 1 bit per pixel to the powerful vector quantization (VQ) based coder that can supply good image quality at rates below 0.5 bits per pixel, we find a sea of algorithms. Some are based on block transforms (DCT), some on lapped transforms, others on subband filter banks, or any combination of all of these schemes. Of particular interest is the investigation and comparison of the performance of different subband filter bank structures used in a typical image codec.

5.2 Problem Statement

Subband coding of images is a technique by which an image is decomposed into a set of subbands each comprising a particular frequency band. This task is accomplished by the usage of an analysis filter bank. The obtained subband signals are presented to the encoder for compression purposes via an optimal and efficient bit allocation scheme. Afterwards, the encoded subband signals are sent through the channel. At the receiver side, the received signals are decoded and passed through a synthesis filter bank to recombine the subbands in order to get a close replica of the original image. At this point, we would like to pose the following questions:

- What type of filter bank ought to be used? That is, should we use an hierarchical splitting or direct partitioning of the image?.
- To what extend should the image be split into subbands prior to coding? that is how many subbands should we split the image to?.

Since our attention is to use filter banks in a complete codec system, we cannot, strictly speaking, separate this study from the use of quantization of the subbands. The reason is that it is the coding part that makes the difference on the quality of the decoded images. Nonetheless, we will use the same coding algorithm in all upcoming experiments in order to study the effects of the different filter bank structures raised up earlier.

5.3 Filter Bank Structures

Filter banks come in two categories hierarchical and direct structures as mentioned earlier. The former makes a repetitive use of a generic two-band (PR or non-PR) filter bank in order to get the desired frequency split. The latter, however, as its name implies, split the signal in a single shot. Fig. 5.1 illustrates several two dimensional frequency band splitting. Fig. 5.1.a and c) can only be obtained using hierarchical structures. Whereas Fig. 5.1.b and d) can be obtained using either type of structure. It is evident from Fig. 5.1 that the direct form M-band structure does not provide multiresolution signal representation which is a by-product in hierarchical M-band structure. In addition, since there can not be any linear-phase two-band paraunitary

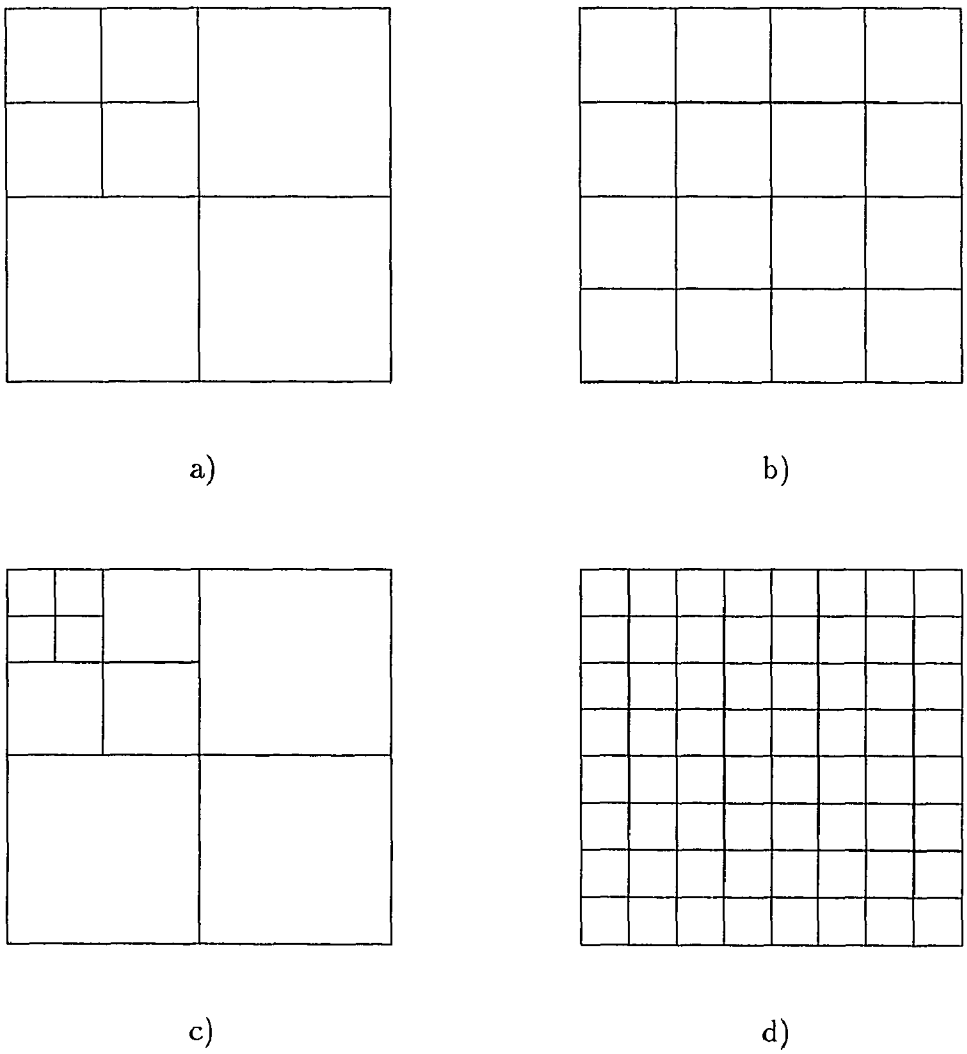

Figure 5.1 Different two-dimensional spectrum splits

filter bank solutions[2][40], all the product filters in hierarchical filter bank have non-linear phase. In contrast, it is possible to design linear-phase M-band paraunitary filter banks with equal bandwidths.

Table 5.1 G_{TC} performance of 2-, 4-, 8-band hierarchical filter bank(based on 2-band PR-QMFs), along with the performance of direct-form filter banks for an $AR(1)$ source of $\rho = 0.95$.

	$2-Band$	$4-Band$	$8-Band$
6-tap BQMF (Hier.)	3.7588	6.7665	8.5293
8-tap BQMF (Hier.)	3.8109	6.9076	8.7431
6-tap (Direct)	3.7588		
8-tap (Direct)	3.8109	6.25	6.42
8-tap (Direct, Multiplierless)		6.0	
16-tap (Direct)		6.85	7.80
32-tap (Direct)		7.05	8.24

5.4 Objective Performance Evaluation

In the beginning part of this evaluation, we shall compare the two structures as they stand by themselves without any coding incorporated in the system. At the end, we will add the coding block in order to evaluate the entire image codec.

5.4.1 Energy Compaction

The gain of transform coding over pulse code modulation(PCM), G_{TC}, has been widely used for the performance comparison of transforms and filter banks[20][2]. This measure for an M-band paraunitary filter bank is defined as

$$G_{TC} = \frac{\sigma_x^2}{(\prod_{j=1}^{M} \sigma_j^2)^{1/M}} \tag{5.1}$$

where σ_x^2 is the input variance and $\{\sigma_j^2\}$ are the variances of subband signals. So the coding can be interpreted in two ways: first, it is the ratio of the input variance σ_x^2 to the geometric mean of the subband variances $\{\sigma_j^2\}$. Second, is the ratio of the arithmetic to geometric mean of the subband signal variances. Table 5.1 provides G_{TC} performance of several different decomposition techniques for an AR(1) source. It is seen from the table that the hierarchical structure has better energy compaction than the direct structures considered here.

5.4.2 Time-frequency Localizations

The time and frequency spreads of a discrete-time sequence were discussed at length in Chapter three. We reproduce their definitions here as a reminder

$$\begin{aligned} \sigma_n^2 &= \frac{\sum_{-\infty}^{\infty}(n-\bar{n})^2|f(n)|^2}{E}, \\ \sigma_\omega^2 &= \frac{\frac{1}{2\pi}\int_{-\pi}^{\pi}(\omega-\bar{\omega})^2|F(e^{j\omega})|^2d\omega}{E} \end{aligned} \tag{5.2}$$

where the means are given as

$$\bar{\omega} = \frac{\frac{1}{2\pi}\int_{-\pi}^{\pi}\omega|F(e^{j\omega})|^2d\omega}{E}$$

$$\bar{n} = \frac{\sum_{-\infty}^{\infty}n|f(n)|^2}{E}$$

Table 5.2 and Table 5.3 displays the time-frequency localizations of several direct and hierarchical paraunitary filter banks. These tables indicate that the time spreads hierarchical structures are worse than the direct structures. On the other hand, the hierarchical cases have better frequency and joint time-frequency localizations.

5.4.3 Peak-to-peak Signal to Noise ratio

The compression algorithm used in this work is a lossy one. In other words, the decoded image is a distorted version of the original image. Therefore, an evaluation measure should be devised in order to assess the quality of the reproduced image. This kind of evaluation is termed an objective measure in contrast to a subjective one. The latter is a visual judgement of the quality of the decoded image made by the humans. One of the often used measure of objective performance is the peak-to-peak signal to noise ratio (PSNR). It is defined as

$$PSNR(dB) = 10log_{10}\frac{255^2}{E\{e(n)^2\}} \tag{5.3}$$

where $e(n)$ is the error between the original and the reconstructed image.

A generic image codec simulation program was utilized in this study. The codec employs any paraunitary filter bank, hierarchical or direct form, for spectral

Table 5.2 The time-frequency localizations of 4-band hierarchical subband tree(2-level, 8-tap Binomial-QMF) along with 8-tap and 16-tap direct 4-band structure

	$\overline{\omega}$	$\overline{n}$	σ_ω^2	σ_n^2	$\sigma_\omega^2 \times \sigma_n^2$
B-QMF Hierarchical 4 Band Tree (22 tap product filters)	0	4.05	0.2526	2.7261	0.6886
	1.23	12.88	0.1222	3.8269	0.4676
	1.91	16.28	0.1222	2.7757	0.3392
	π	8.80	0.2526	2.2622	0.5714
Multiplierless 4 Band Direct (8 tap,linear phase) filters)	0	3.5	0.3763	1.1946	0.4495
	1.17	3.5	0.1357	2.2465	0.3049
	1.97	3.5	0.1357	2.2465	0.3049
	π	3.5	0.3763	1.1946	0.4495
Direct Structure (8-tap, linear phase) filters)	0	3.50	0.3422	1.1541	0.3950
	1.16	3.5	0.1399	2.038	0.2852
	1.97	3.5	0.1399	2.038	0.2852
	π	3.5	0.3422	1.1541	0.3950
Direct Structure (16-tap, linear phase) filters)	0	7.5	0.2643	1.84	0.4855
	1.22	7.5	0.116	2.62	0.3045
	1.93	7.5	0.116	2.62	0.3045
	π	7.5	0.2634	1.84	0.4855

Table 5.3 The time-frequency localizations of 8-band hierarchical subband tree(3-level, 8-tap Binomial-QMF) along with 16-tap and 32-tap direct 8-band structure

	$\overline{\omega}$	$\overline{n}$	σ_ω^2	σ_n^2	$\sigma_\omega^2 \times \sigma_n^2$
B-QMF Hierarchical 8 Band Tree (50 tap product filters)	0	9.12	0.0644	11.726	0.7117
	0.63	26.96	0.0490	15.953	0.7818
	1.01	34.11	0.0961	11.326	1.0880
	1.45	19.65	0.0496	9.7846	0.4857
	1.68	22.56	0.0496	10.510	0.5215
	2.13	37.99	0.0961	12.013	1.1540
	2.52	31.54	0.0490	14.950	0.7327
	π	14.36	0.0644	10.777	0.6942
Direct Structure (16-tap, linear phase) filters)	0	7.5	0.111	4.675	0.5192
	0.69	7.5	0.2313	8.087	1.8703
	1.16	7.5	0.2158	7.3715	1.5912
	1.44	7.5	0.0681	5.296	0.3605
	1.70	7.5	0.0681	5.296	0.3605
	1.98	7.5	0.2158	7.3715	1.5912
	2.45	7.5	0.2313	8.087	1.8703
	π	7.5	0.111	4.675	0.5192
Direct Structure (32-tap, linear phase) filters)	0	15.5	0.0727	4.675	0.5327
	0.71	15.5	0.2158	11.48	2.4785
	1.13	15.5	0.2092	10.70	2.2391
	1.45	15.5	0.0520	8.14	0.4237
	1.68	15.5	0.0520	8.14	0.4237
	2.01	15.5	0.2092	10.70	2.2391
	2.43	15.5	0.2158	11.48	2.4785
	π	15.5	0.0727	4.675	0.5327

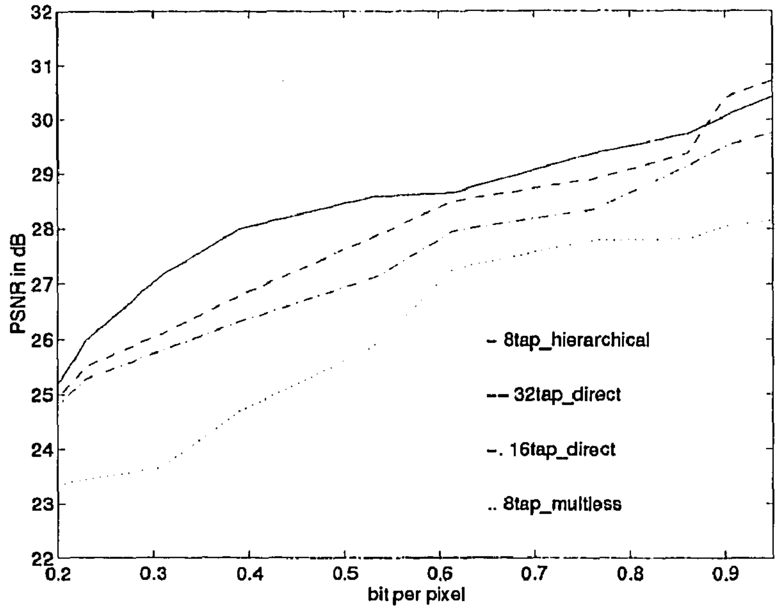

Figure 5.2 The rate-distortion performance of a 64-band subband image codec with direct and hierarchical decomposition structures for the test image LENA

decomposition of images. The subbands are allocated the available bits according to their variances. There were no visual weighting table nor fine tuning used in this codec model for the purpose of a fair image coding performance comparison of different filter banks. Fig. 5.2 displays the rate-distortion curves of 64-band subband image codec employing hierarchical and direct structures for the test image LENA. We also included the performance of a 16-band subband image code using four band eight tap multiplierless direct structure. This performance is depicted with the dotted line in Fig. 5.2. This figure shows that the hierarchical full-tree subband image codec outperforms the direct form cases considered here. Fig. 5.3 displays similar performance curves for the hierarchical subband image codecs of different tree structures. It is seen that the dyadic-tree based subband image codec outperforms the full-tree based codec for the coding experiments performed.

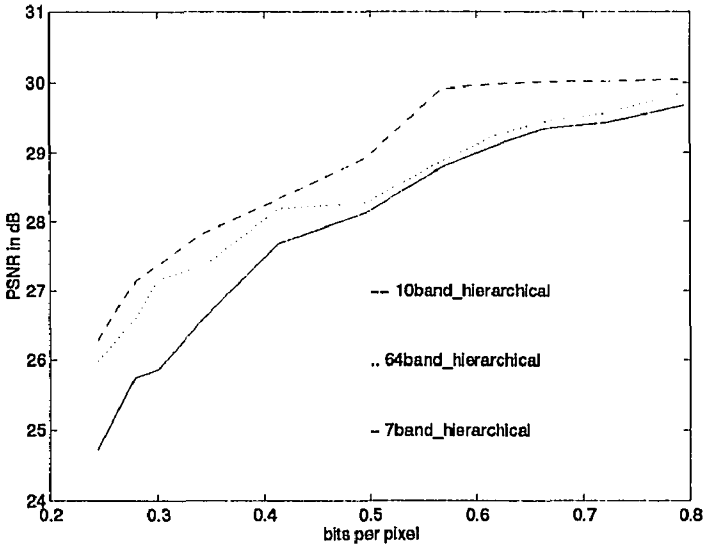

Figure 5.3 The rate-distortion performance of several different hierarchical subband image codecs for the test image LENA

5.5 Discussions and Conclusions

The following conclusions were drawn from the theoretical and experimental studies performed in this thesis:

1. The hierarchical 8-band split(50-tap product filters) provides a better energy compaction than the direct 8-band split(32-tap filters) for the cases considered here. The compaction performance increases when the number of bands is increased.
2. The time spread of hierarchical 8-band split is more than the direct form 8-band split for the cases considered in this study. The first has a non-linear(linear-like) phase response while the latter has linear phase response. The hierarchical structure has better frequency and joint time-frequency localizations than the direct forms considered.
3. The hierarchical structure(64-band) gave better rate-distortion performance than the direct form(64-band) structure for the test image LENA. The

visual quality of the compressed images for the 64-band hierarchical case were superior to the 64-band direct form cases considered.

4. The hierarchical dyadic tree of 10-bands outperformed the hierarchical full tree of 64-bands both objectively and subjectively for the experiments performed in this study. This somehow agrees with the concept of having better time-localized functions for the representation of high-frequency signal components. This observation suggests the computationally efficient dyadic-tree structures over full-tree structures for image coding.

5. The *tree structuring* or *time-frequency tiling* is an important concept in subband signal decomposition[4]. The different subbands of different applications should be treated accordingly. This also implies a flexible filter bank design concept which is expected to find its applications in the future.

6. More experimental studies for the visual assessment of quantization noise in subband image coding are expected in the future. The commonly agreed Q-tables of subband image coding are to be defined.

CHAPTER 6

DISCRETE MULTITONE TRANSCEIVERS

6.1 Introduction

A general digital communications system is depicted in Fig. 6.1[25]. A bit stream is passed through a coder to generate data symbols depending on the type of modulation needed. These data symbols are applied to a transmit filter, which generates a continuous-time signal fit for transmission over the continuous-time channel. The channel reshapes the transmitted signal and corrupts it with additive noise. At the receiver end, the received signal is processed by a receive filter to undo the effects of the channel and thus useful information is recovered. The decoder basically remaps the received symbols into a bit stream.

6.2 Discrete Multitone Modulation

Discrete multitone (DMT) or multi-carrier modulation is a class of orthogonal frequency division type of modulation. This concept dates back to the middle of 1960's[10] , but received more attention since 1980[31][12]. A discrete version of multitone (DMT) has been proposed as a standard for high-speed digital subscriber line (HDSL) and asymmetric digital subscriber line (ADSL) communications[12][39]. In this frequency division type modulation, a multitude of parallel QAM sub-channels are used to transmit data in order to maximize the throughput of the channel. The basic structure of a DMT transceiver is illustrated in Fig. 6.2. Instead of using a single modulation filter, the system makes use of a set of N modulating filters called transform basis functions. These filters can be represented as a set of vectors for discrete systems. These vectors are normally chosen to be an orthonormal family, i.e.

$$< p^i, p^j > = \delta_{ij} \tag{6.1}$$

where $<, >$ stands for the dot product.

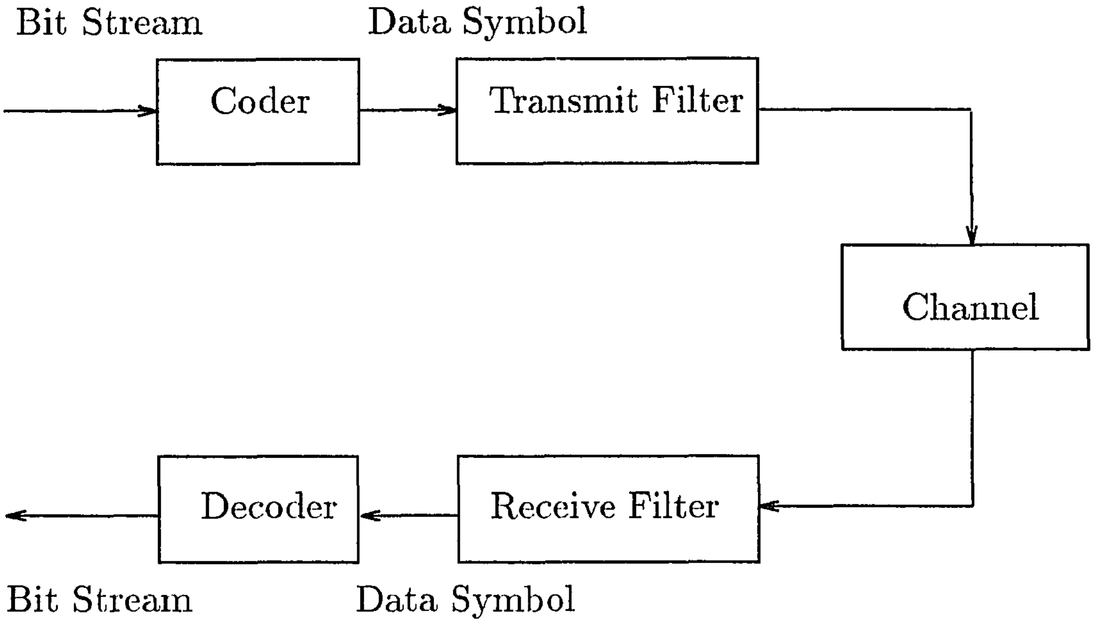

Figure 6.1 A general digital communications system

The sub-symbols $(X_0, X_1, ..., X_{N-1})$ that are applied to the modulating vectors $\{p_i\}$ are usually complex for quadrature amplitude modulation (QAM) schemes and real for pulse amplitude modulation (PAM) ones. These sub-symbols are formed by grouping sub-block of bits in the constellation step. The parsing of the incoming bits to the sub-symbols is controlled by the channel attenuations. Since the transmitted signal is the composite of N independent sub-signals or sub-channels, each of the sub-channels will carry a different number of bits commensurate on the sub-channel attenuation. Therefore, sub-channels that suffer less attenuation will carry more bits of information. This discussion leads to the work of Kalet[22]. In fact, Kalet studied the performance of multitone for the case of two and infinite number of sub-channels. He showed that multitone QAM systems provide a substantial increase in the achievable bit rate as compared to that of a single tone QAM for brickwall channel response cases. He also showed that multitone becomes theoretically optimum, i.e.

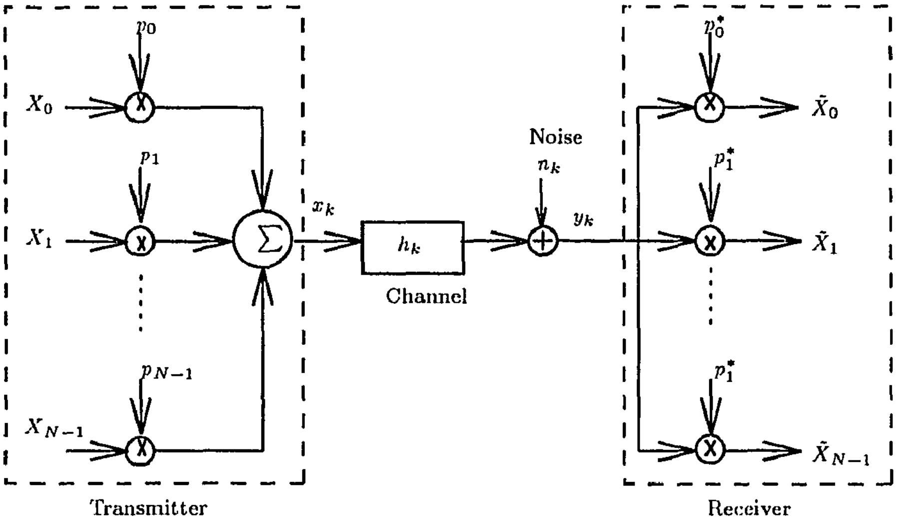

Figure 6.2 Basic structure of a DMT

approaching the channel capacity to within 8 to 9 dB, when an infinite number of carriers is used.

6.3 QAM Multitone System

Multitone systems can take many forms of modulation/demodulation schemes. However, QAM based mutitone systems were studied more widely in the literature. In order to understand the operation of a QAM multitone system, we would like to review some of the basic concepts of the scheme.

6.3.1 QAM System

We can think of a QAM system as a two-dimensional system and the signal constellation is on a two-dimensional plane. In general, the constellations take a variety of forms. For simplicity, we will assume that these constellations take a square shape containing some power of 4 symbols. Fig. 6.3 illustrates the constellation points of 2^4 or 16 point QAM. The probability of error, P_e, of a two-dimensional symbol in

QAM is given by[24]

$$P_e = KQ(\frac{d}{2\sigma}) = KQ(a\sqrt{\frac{2}{N_0}}) \tag{6.2}$$

where K is the number of neighboring symbols. It is given by

$$K = 4(1 - \frac{1}{\sqrt{2^n}}) \tag{6.3}$$

where n is the number of bits and it is assumed to be even. The distance between adjacent symbols in the constellation is $d = 2a$. N_0 is the power spectral density (PSD) and σ^2 is the noise variance such that $\sigma^2 = \frac{N_0}{2}$. The average symbol energy is given by

$$E = \frac{2}{3}(2^n - 1)a^2 \tag{6.4}$$

From this, we can relate n to the probability of error as

$$n = log_2\left[1 + \frac{3P}{N_0 W Q^{-1}(\frac{P_e}{K})}\right] \tag{6.5}$$

where $P = EW$ and W is the bandwidth.

6.3.2 General Concepts of Multitone

Fig. 6.4 depicts a QAM multitone system[22]. The transmitted signal consists of N QAM signal tones combined, each with a rectangular Nyquist spectrum of bandwidth equal to W_i Hz. We assume that the channel has a magnitude response of a staircase shape as shown in Fig. 6.5. In other words, the channel exhibits a brickwall magnitude response in each sub-channel, rendering the system ISI free.

The individual M-ary QAM tones have different number of bits per symbol where $M = 2^{n_i}$, n_i being the number of bits per symbol assigned for the i^{th} subchannel. It is assumed that each tone has different transmit power P_i such that the total transmitted power $P = \sum_{i=1}^{N} P_i = constant$. The total bit rate R_b is given by $R_b = \sum_{i=1}^{N} n_i W_i$ where W_i is the bandwidth of the i^{th} sub-channel. The idea behind multitone is to maximize R_b by optimally dividing the total power P among

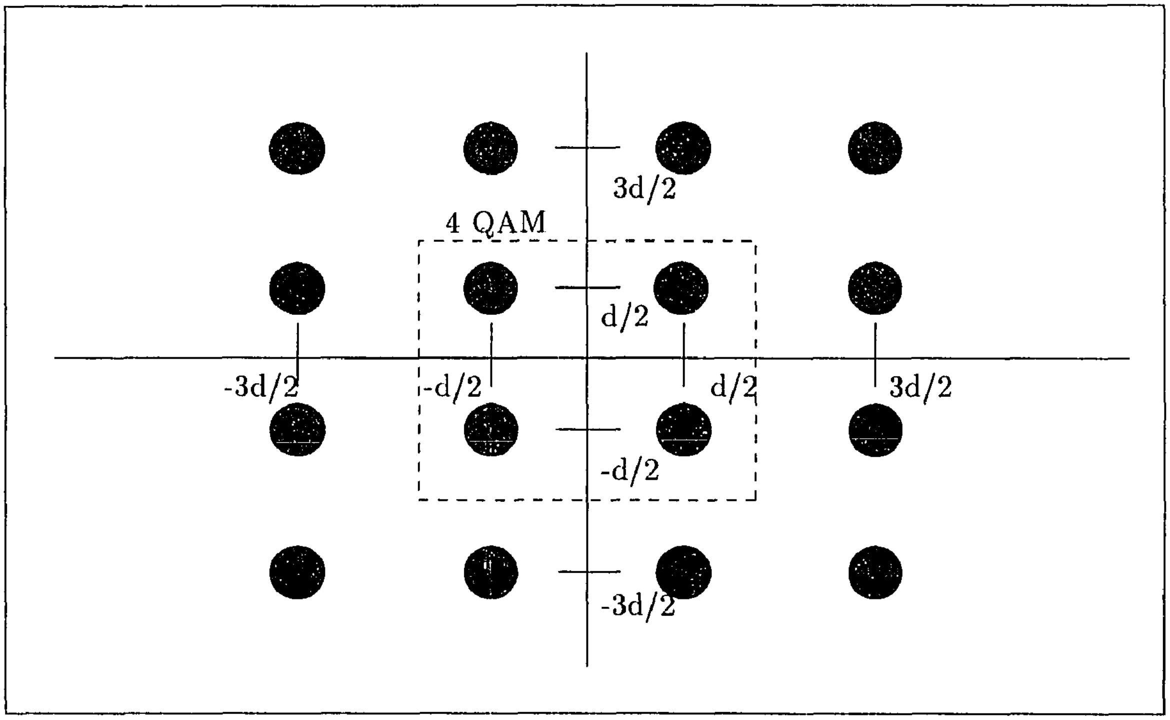

Figure 6.3 16 QAM constellation

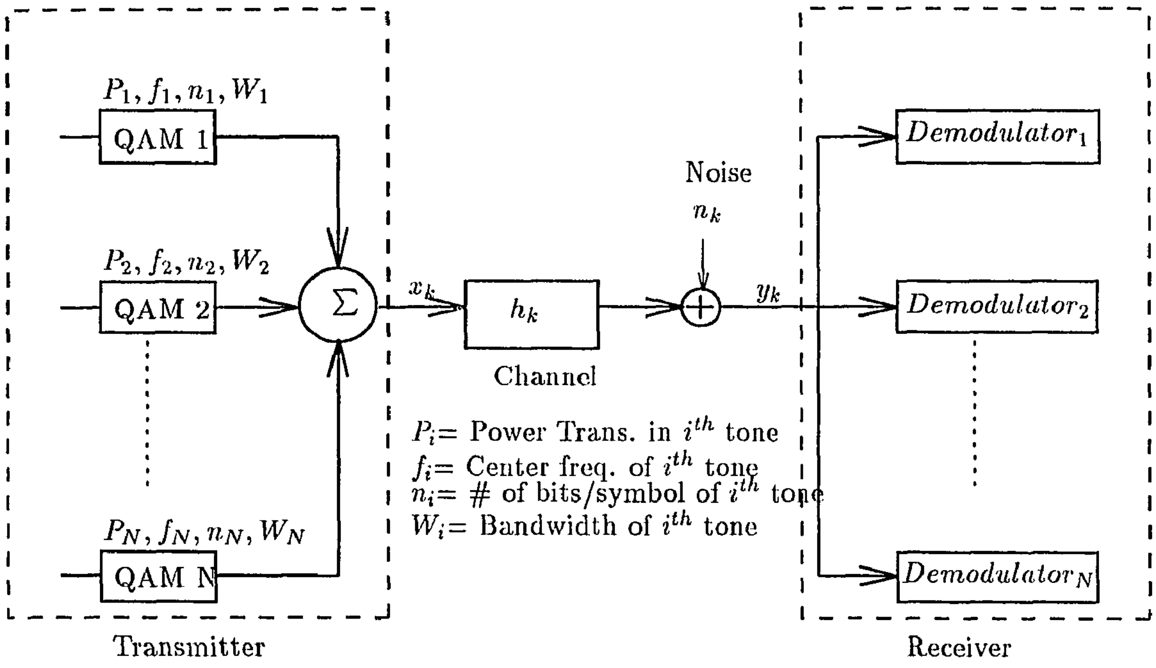

Figure 6.4 The multitone QAM system

the different tones or equal bandwidth sub-channels. As mentioned before, the sub-channels that suffer from more attenuation, receive less power and vice-versa.

6.3.3 Optimum Power Allocation

We extend the optimal power allocation scheme of Kalet[22] that considered only two-tone and ∞ of tones to an arbitrary number of sub-channels. This derivation is general in contrast to the indirect proof given by Kalet[21]. We assume that the probability of symbol error in each sub-channel to be equal to P_e. It can be shown that the bit assignment for the i^{th} channel to be given by[21]

$$n_i = log_2(1 + NM_ik_il_i) \tag{6.6}$$

where N is the total number of sub-channels, k_i is the proportion of the total power P allocated to the i_{th} sub-channel, l_i is the gain of that sub-channel, and M_i is a

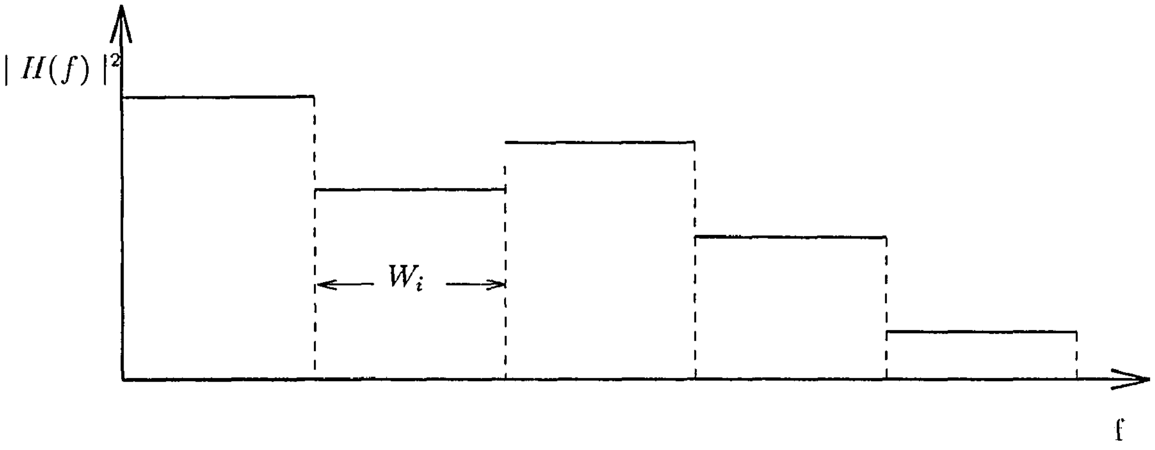

Figure 6.5 Brickwall magnitude response

constant that can be shown to be equal to [22]

$$M_i = \frac{3P}{WN_oQ^{-1}(P_e/Kn_i)} \tag{6.7}$$

where W is the total bandwidth of the channel, P_e is the symbol probability of error, and finally Kn_i is the number of neighbors in the i^{th} sub-channel.

We want to maximize the total bit rate R_b given by

$$R_b = \frac{W}{N}\sum_{i=1}^{N} log_2(1 + NM_ik_il_i) \tag{6.8}$$

subject to the following constraints

$$\sum_{i=1}^{N} k_i = 1 \tag{6.9}$$

and $k_i \geq 0$ for all i's. This optimization leads to

$$k_i = \frac{1 + \sum_{j=1}^{N}\frac{1}{NM_jl_j}}{N} - \frac{1}{M_il_iN} \tag{6.10}$$

It should be noted that the optimal bit allocation algorithm described here assumes the decomposition of a given channel into equal bandwidth sub-channels. The optimal values of k_i given by Eq. (6.10) reduce to $k_i = \frac{1}{N}$ at high signal-to-noise

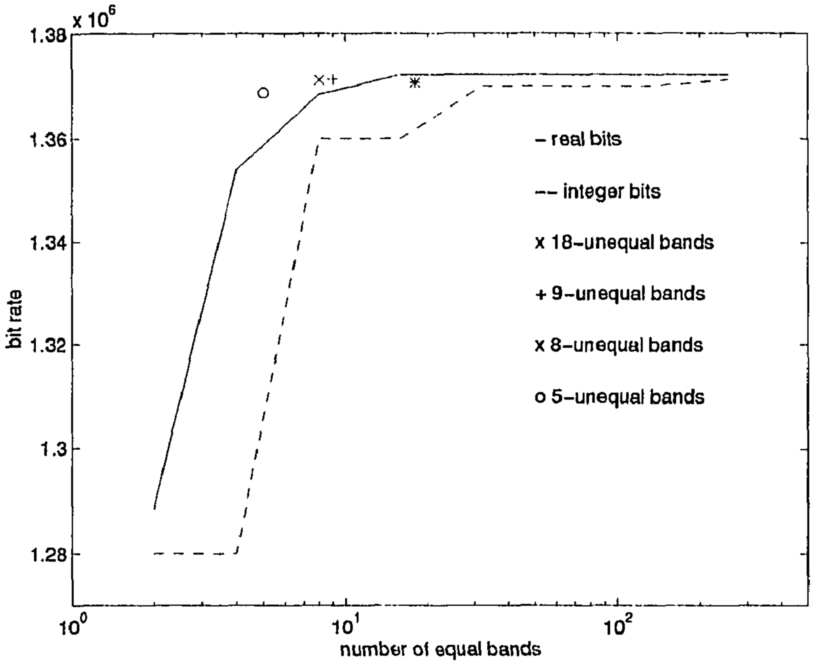

Figure 6.6 Performance curve of the Multitone

ratio. This is exactly the optimum value given by Kalet [21]. The performance curves of a multitone system for a typical subscriber loop, namely CSA Loop1 at 640 KHz sampling rate, corrupted by white Gaussian noise at -100 dBm for several different scenarios are depicted in Fig. 6.6. The input power is 20 mW in this example. The probability of symbol error is of 10^{-7}. These curves suggest that the more number of sub-channels we use, the larger the bit rate we can achieve. However, no significant theoretical performance improvement is observed beyond 20 sub-channels or so. The solid curve in Fig. 6.6 assumes a brickwall split of the channel into sub-channels and thus it is ISI free. The dashed curve assumes integer values for the different bits allocated to the sub-channels.

6.4 Practical Realizations of Modulation/demodulation

Theoretically speaking, multitone justifies itself. However, the practical issues regarding the implementation of a multitone do not seem to be appealing from a system designer point of view because of the need of having many QAM generators at the transmitter. The receiver will also require the same complexity as well. Fortunately, the linear orthonormal transform bases came to the rescue.

6.4.1 IDFT/DFT

We mentioned previously that the modulating/demodulation vectors form in general an orthonormal basis. Peled and Ruiz 1980[31] proposed the IDFT/DFT basis family as the modulating/demodulating vectors. Later, Ruiz, et al[34] improved this scheme. IDFT/DFT based DMT is shown in Fig.6.7. A mapping scheme of the N complex QAM symbols is performed before taking the IDFT in order to produce a real time domain samples. Basically, the scheme maps N complex $X(k)$ symbols into $2N$ $\tilde{X}(k)$ symbols that satisfy a certain conjugate symmetry property namely

$$\tilde{X}(k) = \tilde{X}^*(2N - k) \tag{6.11}$$

in order to obtain a suitable real signal as input to a real channel. The time-domain samples are passed through the channel as usual. At the receiver end, the demodulation process takes place through the use of a DFT to analyze the signal into the sub-symbols. An inverse mapping is further applied to get back the N QAM sub-symbols, hence the bit stream.

6.4.2 IDCT/DCT

The IDFT/DFT pair is replaced by an IDCT/DCT basis family. Since this is a real transform, the sub-symbols are assumed to be generated by a real modulation scheme, namely PAM. In order to get the optimum power allocation as applied to

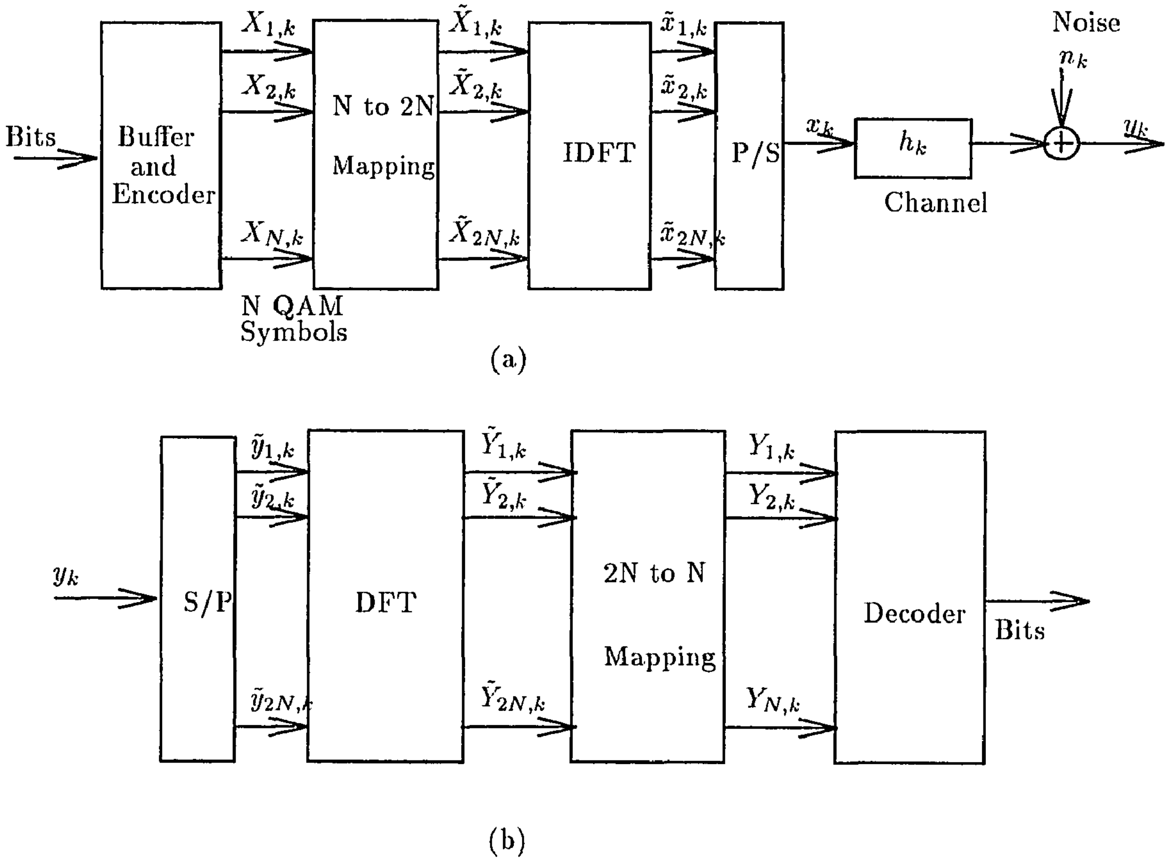

Figure 6.7 IDFT/DFT DMT: a) transmitter, b) receiver

PAM DMT, we follow the same treatment done using QAM. In this case [24],

$$P_e = KQ(\frac{d}{2\sigma}) = KQ(\frac{A}{\sigma}) \tag{6.12}$$

where K is given in this case as

$$K = 2\frac{(M-1)}{M} \tag{6.13}$$

and $A = \frac{d}{2}$. In PAM systems, the average energy of the symbol is expressed[24]

$$E = \frac{M^2-1}{3}A^2 \tag{6.14}$$

where M is the number of symbols in a PAM constellation. The bit rate for the i^{th} sub-channel becomes

$$n_i = \frac{1}{2}log_2\left[1 + \frac{6Nk_il_iP}{N_0WQ^{-1}(\frac{P_e}{Kn_i})}\right] \tag{6.15}$$

The constant M_i of Eq. (6.7) is modified accordingly as

$$M_i = \frac{6P}{WN_oQ^{-1}(P_e/Kn_i)} \tag{6.16}$$

6.4.3 M-band Filter Bank

The superiority of filter bank in frequency selectivity over block transforms is very well known[2][40][8]. Filter banks provide basis functions that are longer in time than the basis functions of block transforms. Therefore, they should have superior signaling performance if they are applied as the building block of the modulator/demodulator in a DMT transceiver. Tzannes et al.[39] have proposed such an approach in their discrete wavelet multitone (DWMT) as a substitute to the DFT based DMT[11][12]. They showed that DWMT is superior to its Fourier based DMT because of the better sub-channel isolation. A block diagram of DWMT is illustrated in Fig. 6.8. It should be noticed from this figure that DWMT is the dual of an M-band filter bank. Therefore, $G_i(z)$ and $H_i(z)$ are the synthesis and analysis filters of an M-band filter bank, respectively, as defined in Fig. 2.5.

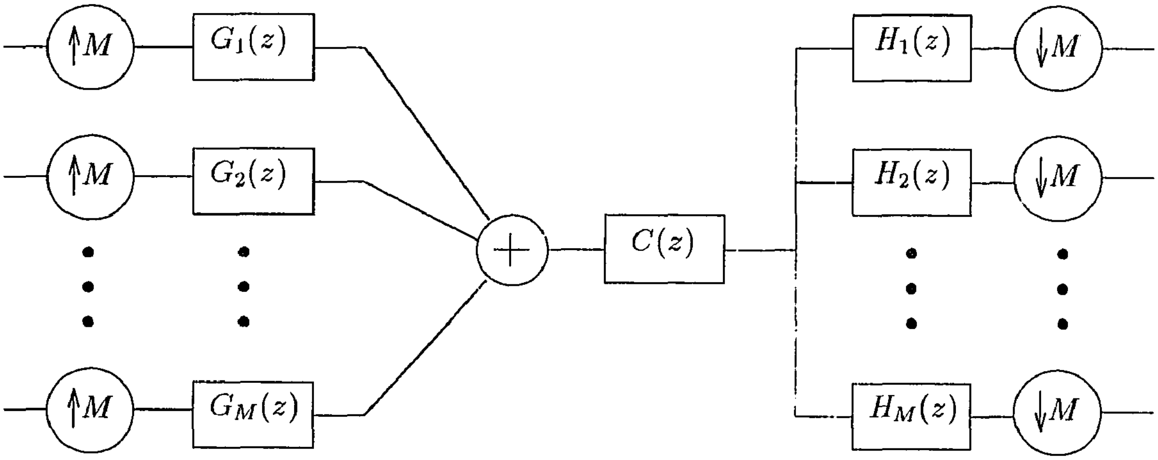

Figure 6.8 M-band realization of a DMT

6.5 Proposed Concept of Sub-channel Structuring

Any spectral splitting should not be performed blindly. Rather, a smart, justified unequal bandwidth split is to be performed for practical performance improvements. We propose the following algorithm for spectral decomposition as it is applied to the splitting of a channel into its sub-channels. To appreciate the advantages of the concept of sub-channel structuring, we plotted the impulse response of the channel (Fig. 6.9) along with its magnitude response in dB (Fig. 6.11). We, further, included the first derivative of its magnitude response (Fig. 6.10) and the magnitude response (Fig. 6.12). It is clear from these figures that the spectrum of the channel does not change significantly for some regions. Therefore, these regions can be combined together to form sub-channels of unequal bandwidths without significant performance degradation from the equal bandwidth decomposition of the channel. In practice, less number of channels implies less energy leakage among sub-channels. Hence, there is less distortion due to the interchannel interference (ICI). We can therefore highlight the conceptual advantages of this smart channel structuring over the conventional fixed decompositions as follows:

- It prevents redundant splitting of the channel, hence yielding a reduced complexity.
- The unnecessary splitting causes an increased aliasing between subchannels which is to be kept at its minimum.

6.5.1 A Simple Subchannel Structuring Algorithm

The full channel spectrum is divided into two equal bandwidth subchannels. If the energy σ_x^2 of the parent node is greater than a certain predefined threshold T_1, and if the ratio of the energies of the two children nodes is greater than another predefined threshold T_2, the splitting is justified at that parent node. Therefore, two new nodes or subchannels are obtained. If these unevenness tests fail, the splitting process is

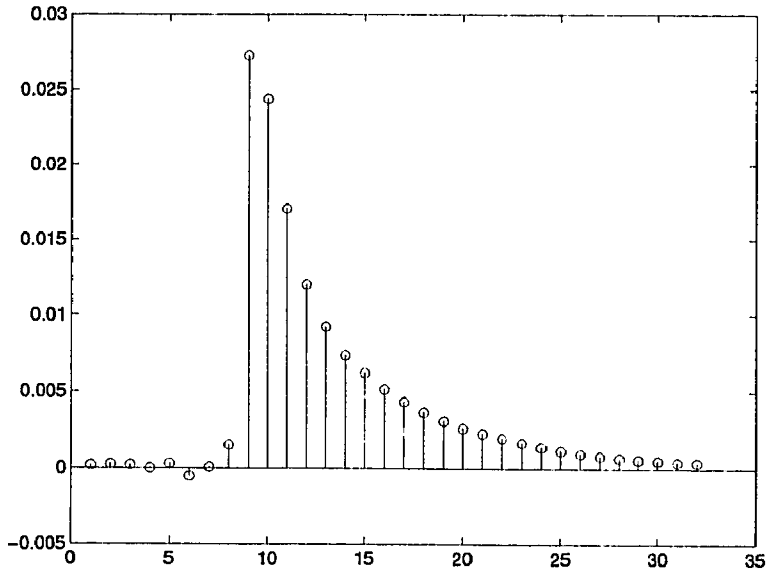

Figure 6.9 Impulse response of a typical CSA loop

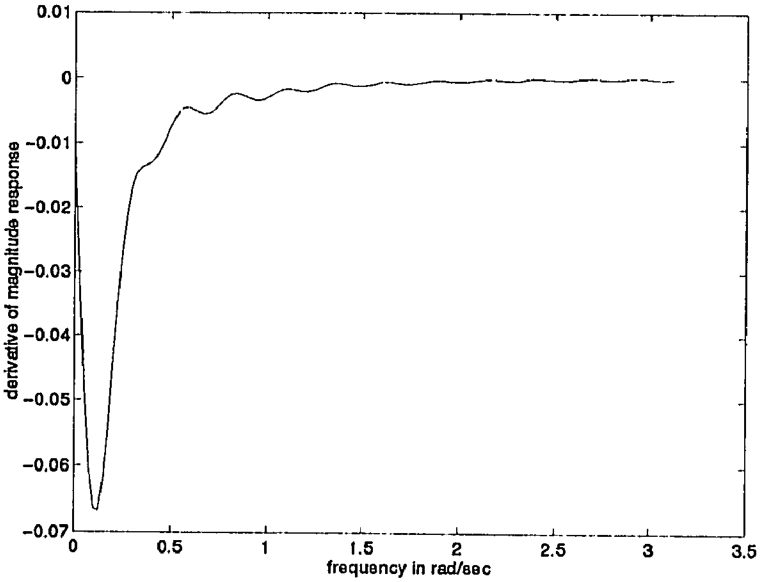

Figure 6.10 Derivative of magnitude response of a typical CSA loop

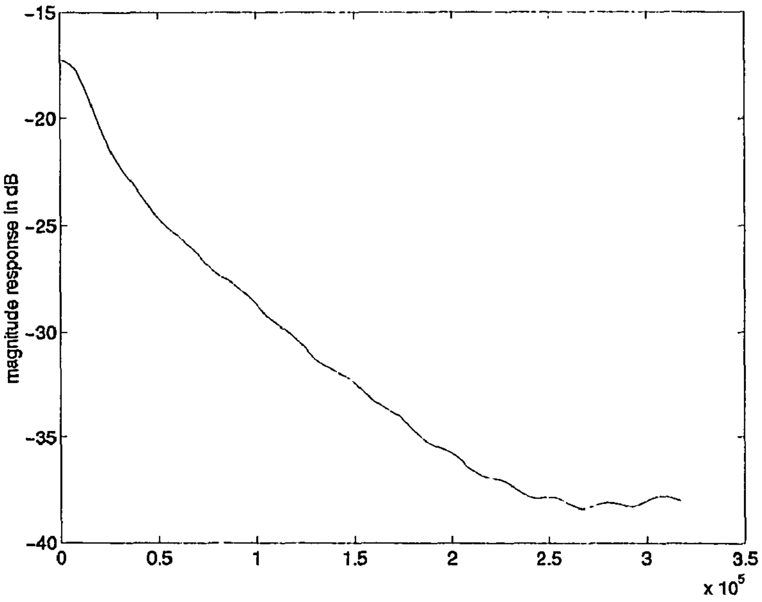

Figure 6.11 Magnitude response of a typical CSA loop

stopped at that level. Otherwise, it continues individually for each of the two new nodes. This algorithm somehow checks if there is both a.) enough unevenness in the parent spectrum or node and b.) enough energy in it to justify another spectral split. This unevenness check of the channel spectrum tries to mimic the derivative of the magnitude response. Based on this splitting scheme, we obtained the following sub-channel structure for the given channel (Fig. 6.13). Fig. 6.12 shows a brickwall unequal bandwidth approximation of the channel. It is clear from this figure that the channel split is finer at portions where both the magnitude response changes faster and the energy content is significant. On the other hand it is coarser when its slope levels off and/or energy content is insignificant. We can obtain different decompositions of the channel by varying the thresholds $T1$ and $T2$. Figs. 6.14, 6.15 and 6.16 illustrate this aspect.

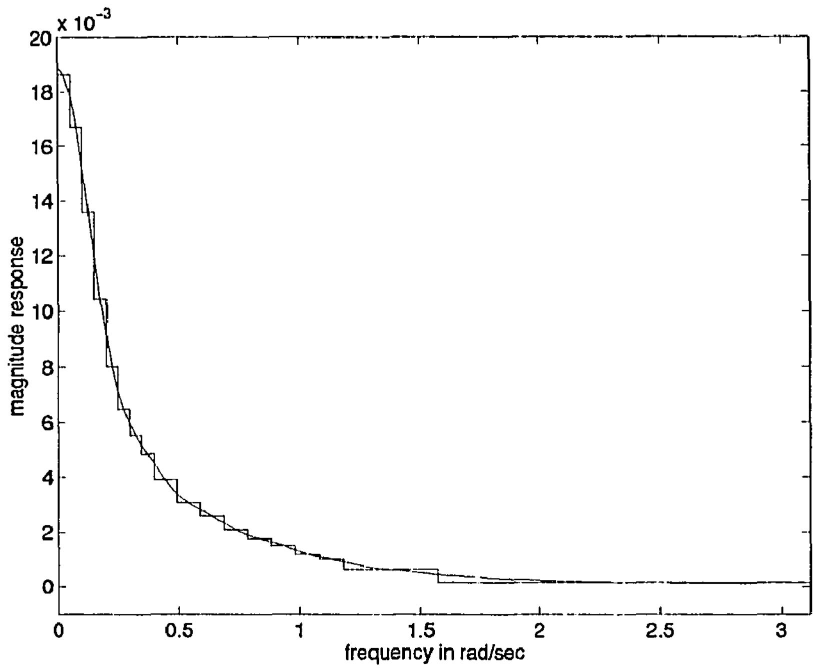

Figure 6.12 Magnitude response and its unequal bandwidth brickwall approximation

6.5.2 A Distortion Measure in Discrete Multitone Transceivers

All of the realizations of the DMT transceivers discussed before suffer from two kinds of distortions. The first kind of these distortions is the intersymbol interference (ISI) caused by the dispersive nature of the channel. ISI, therefore arises because the channel does not have a brickwall (ideal) type of frequency response. The second kind of distortions that plague DMT's is the interchannel interference (ICI). It is caused by the non-ideal nature of the synthesis/analysis filters used as modulators/demodulators. Therefore, interchannel interference immunity is not possible in a realizable DMT. We would like to develop a quantitative assessment of these two impairments which are inherent in a real digital communications scenario.

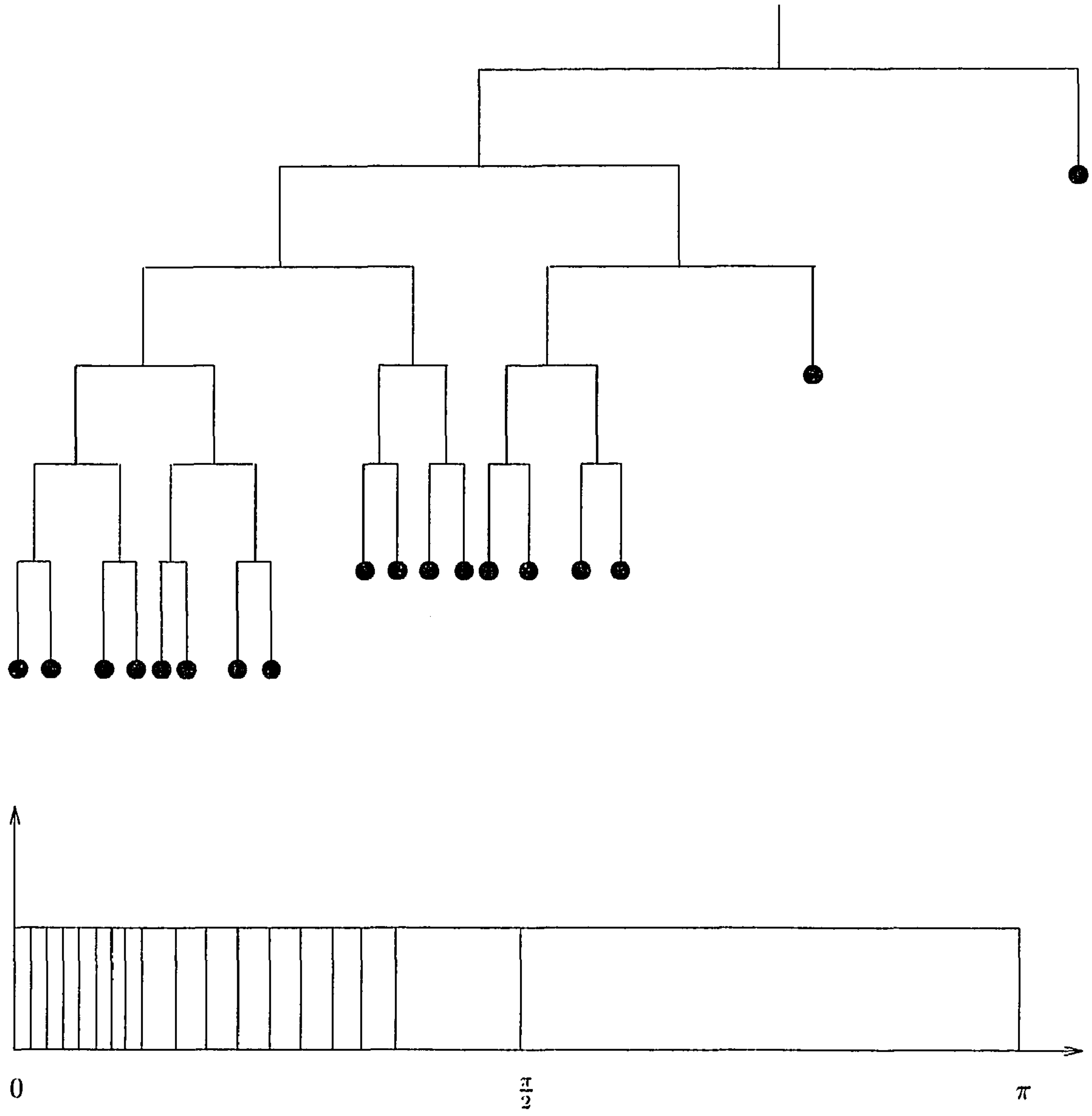

Figure 6.13 An eighteen unequal bandwidth sub-channel structure for the given example

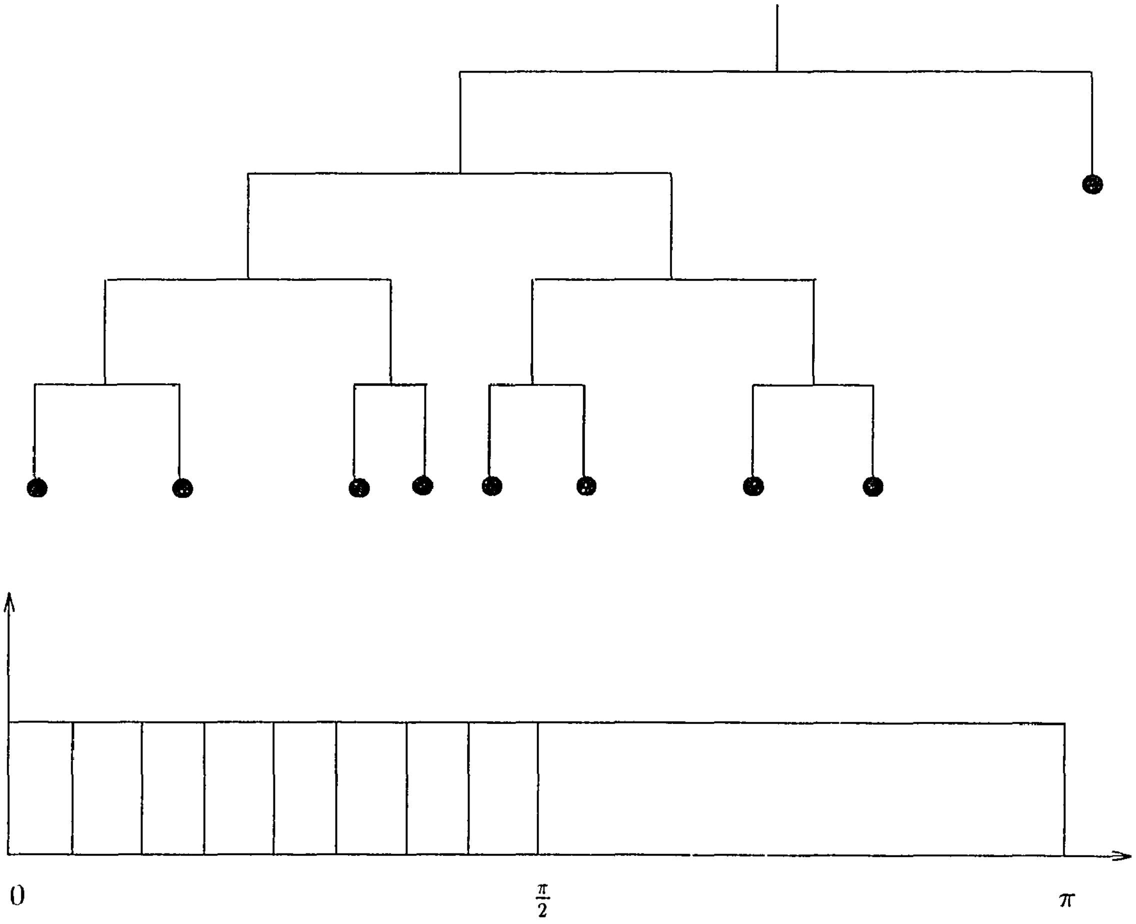

Figure 6.14 A nine unequal bandwidth sub-channel structure for the given example

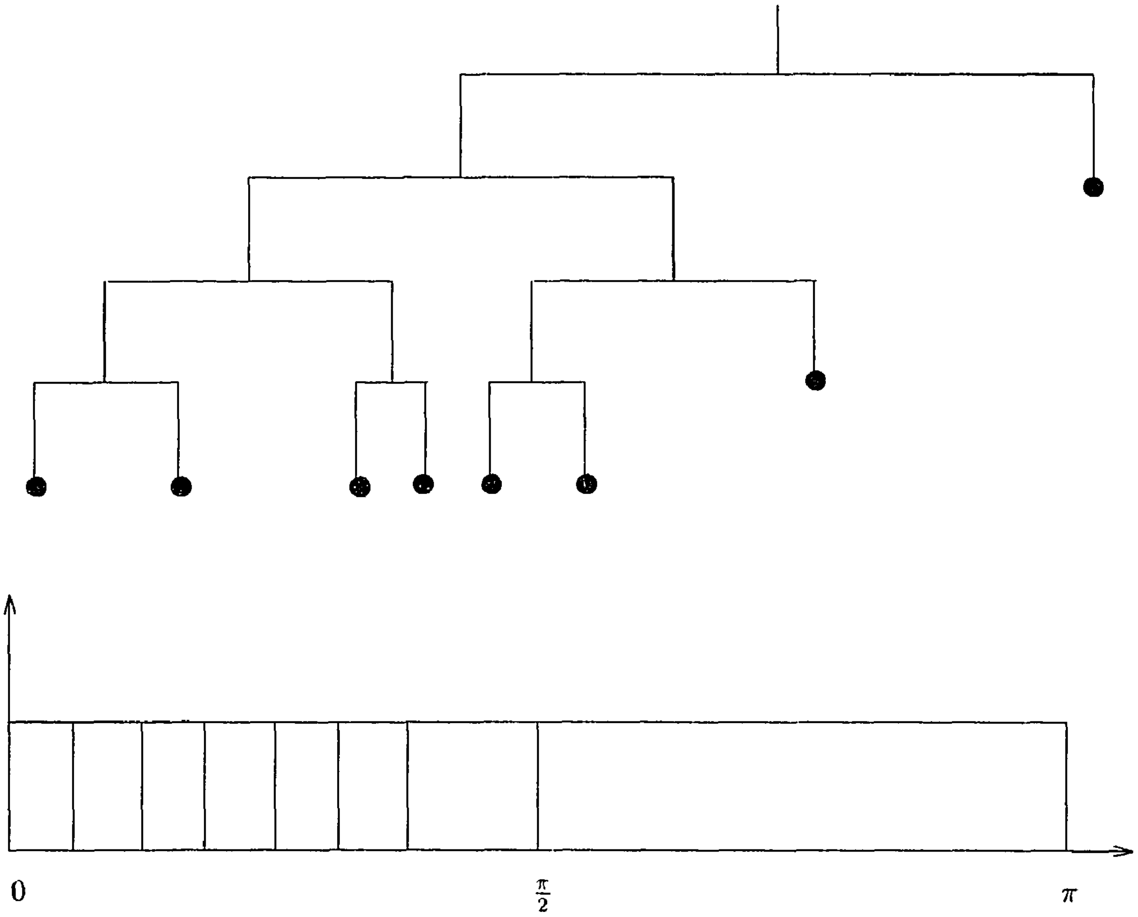

Figure 6.15 An eight unequal bandwidth sub-channel structure for the given example

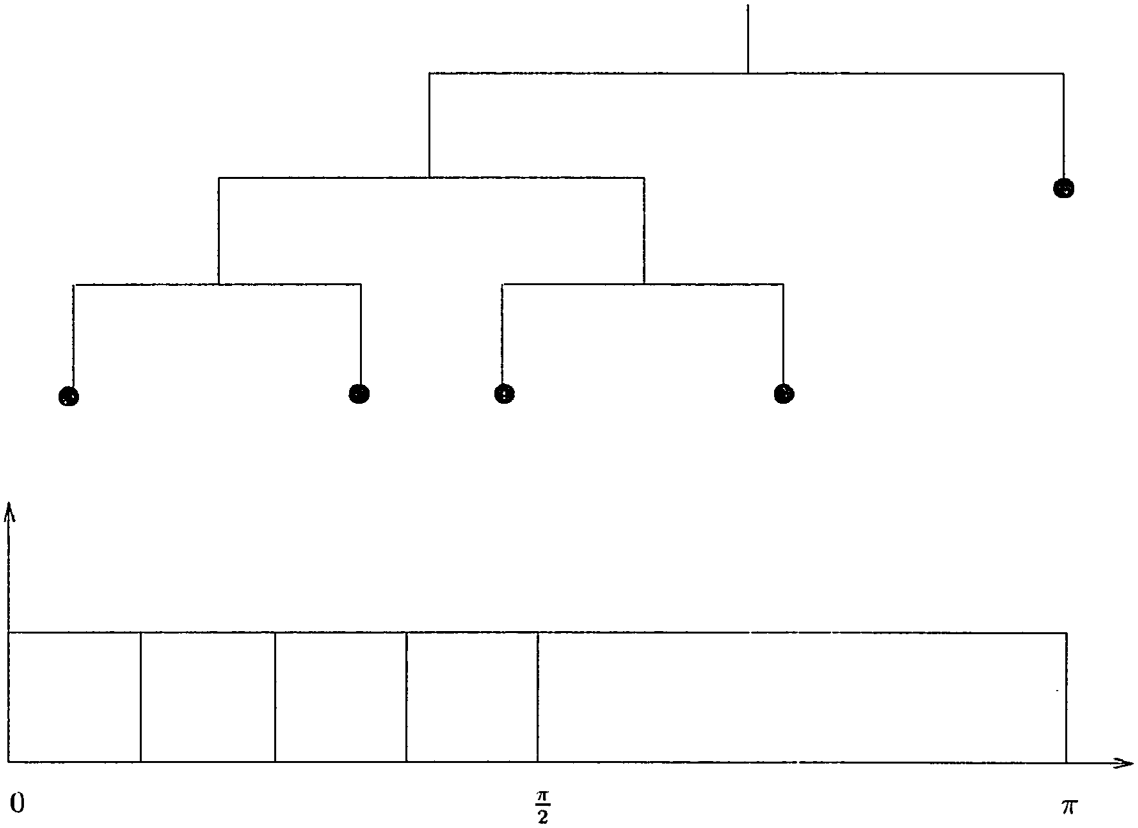

Figure 6.16 A five unequal bandwidth sub-channel structure for the given example

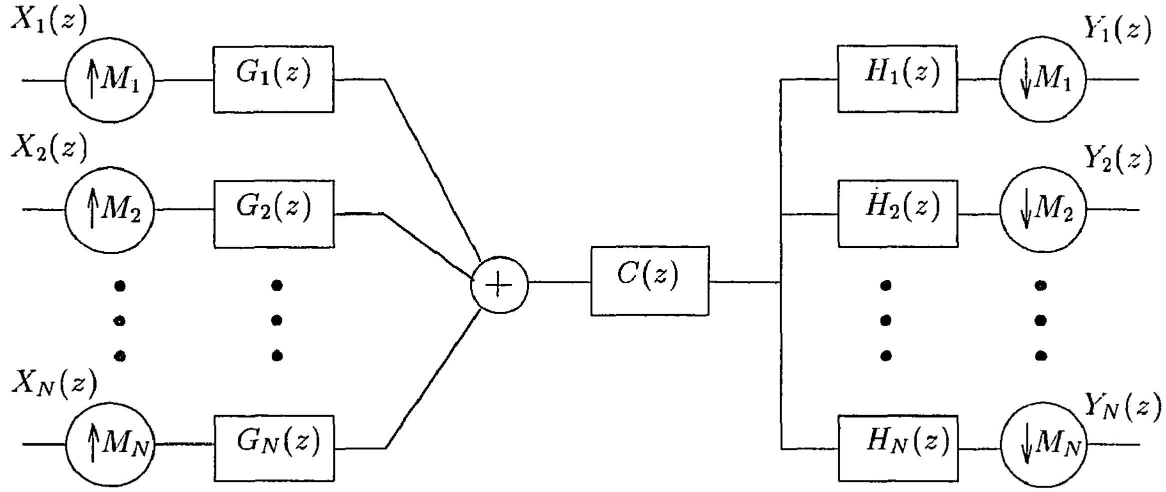

Figure 6.17 N-band realization of a DMT

6.5.3 Distortion in N-band Discrete Multitone Transceivers

The polyphase representation of a filter, introduced in Chapter 2,, is the ground for the study of distortion in N-band discrete multitone transceivers. We can easily trace the output of the k^{th} subchannel. Fig. 6.17 depicts an N-band realization of a DMT transceiver. This realization is general and it can be applied to both equal and unequal bandwidth sub-channel cases. Let $P_k^k(z)$ be the product filter of the synthesis filter $G_k(z)$, the analysis filter $H_k(z)$, and the channel $C(z)$. Therefore, the output $Y_k^k(z)$ of the k^{th} subchannel due to the input $X_k(z)$ of the k^{th} subchannel is given as

$$Y_k^k(z) = F_k(z)X_k(z) \tag{6.17}$$

where $F_k(z)$ is the 0^{th} polyphase component of the composite filter $P_k^k(z)$. The overall subchannel output $Y_k(z)$ due to the input $X_k(z)$ and all of the other inputs $X_j(z)$, where $1 \leq j \leq N, N \neq j$ is readily given as

$$Y_k(z) = F_k(z)X_k(z) + \sum_{j=1, j\neq k}^{N} Y_k^j(z) \tag{6.18}$$

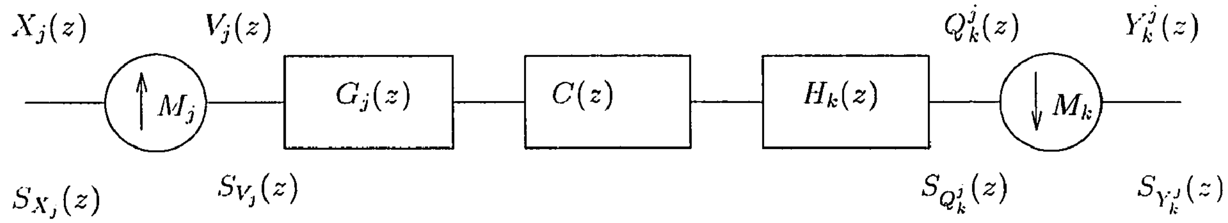

Figure 6.18 A generic branch for ICI calculation

where the first term is $Y_k^k(z)$. The second term is due to the influence of the other subchannels. This distortion is termed interchannel interference (ICI). We would like now to derive an expression for the energy of this distortion. Let us analyze one of the paths that contributes to ICI. We consider Fig. 6.18 for this analysis. Let $S_{X_j}(z)$ be the input power spectral density of the j^{th} subchannel, where $j \neq k$. The upsampler M_j at the j^{th} subchannel implies that

$$S_{V_j}(z) = \frac{1}{M_j} S_{X_j}(z^{M_j}) \tag{6.19}$$

The filters $G_j(z)$, $C(z)$, and $H_k(z)$ further set the following relation

$$S_{Q_k^j}(z) = S_{V_j}(z)G_j(z)G_j(z^{-1})C(z)C(z^{-1})H_k(z)H_k(z^{-1}) \tag{6.20}$$

so that

$$S_{Y_k^j}(z) = \frac{1}{M_k}\sum_{l=0}^{M_k-1} S_{Q_k^j}(z^{\frac{1}{M_k}} W^l) \tag{6.21}$$

where $W = e^{\frac{-j2\pi}{L}}$, L is the duration of the aggregate of filters $G_j(z)$, $C(z)$ and $H_k(z)$. Since the different subchannel inputs $X_j(z)$ are assumed to be uncorrelated, and white noise with equal energies $\mathcal{E}$, i.e $S_{X_j}(z) = \mathcal{E}$, we can easily express the total energy for the ICI distortion as

$$\sigma_{ICI}^2 = \sum_{j=1, j\neq k}^{N} \frac{1}{2\pi}\int_{-\pi}^{\pi} S_{Y_k^j}(e^{j\omega})\, d\omega \tag{6.22}$$

We derived a closed form expression for ICI. Similarly, we would also like to define the expression for the intersymbol interference (ISI) distortion caused by

$F_k(z)$ on the output $Y_k(z)$. $Y_k^k(z)$, given earlier by Eq. (6.17), can be written in time domain as

$$y_k^k(n) = \sum_{l=0}^{N_k^k-1} f_k(l)x_k(n-l) \tag{6.23}$$

where N_k^k is the number of taps of $F_k(z)$. We can rewrite Eq. (6.23) as a sum of the desired term plus ISI as

$$y_k^k(n) = f_k(D)x_k(n-D) + \sum_{l=0,l\neq D}^{N_k^k-1} f_k(l)x_k(n-l) \tag{6.24}$$

where D is an appropriate delay. The energy of the ISI distortion for a zero-mean input is derived as

$$\sigma_{ISI}^2 = E\left\{\left[\sum_{l=0,l\neq D}^{N_k^k-1} f_k(l)x_k(n-l)\right] \cdot \left[\sum_{l'=0,l'\neq D}^{N_k^k-1} f_k^*(l')x_k^*(n-l')\right]\right\} \tag{6.25}$$

where E is the expectation operator. We can still pursue this derivation as

$$\begin{aligned}
\sigma_{ISI}^2 &= E\left\{\sum_{l=0,l\neq D}^{N_k^k-1}\sum_{l'=0,l'\neq D}^{N_k^k-1} f_k(l)f_k^*(l')x_k(n-l)x_k^*(n-l')\right\} \\
&= \sum_{l=0,l\neq D}^{N_k^k-1}\sum_{l'=0,l'\neq D}^{N_k^k-1} f_k(l)f_k^*(l')E\left\{x_k(n-l)x_k^*(n-l')\right\} \\
&= \mathcal{E}\sum_{l=0,l\neq D}^{N_k^k-1} f_k(l)f_k^*(l) \\
&= \mathcal{E}\sum_{l=0,l\neq D}^{N_k^k-1} \mid f_k(l)\mid^2
\end{aligned} \tag{6.26}$$

The last equation utilizes the fact that samples of $x_k(n)$ and $x_k(m)$ are uncorrelated except when $n = m$ since they are assumed to be white sequences. Therefore, the total distortion at the k^{th} subchannel due to both ISI and ICI is simply the sum of σ_{ISI}^2 and σ_{ICI}^2 as

$$\sigma_D^2 = \sigma_{ISI}^2 + \sigma_{ICI}^2 \tag{6.27}$$

Fig. 6.19 illustrates the total distortion (ICI + ISI) for different family bases in a DMT transceiver using a CSA Loop1. It is clear from Fig. 6.19 that the

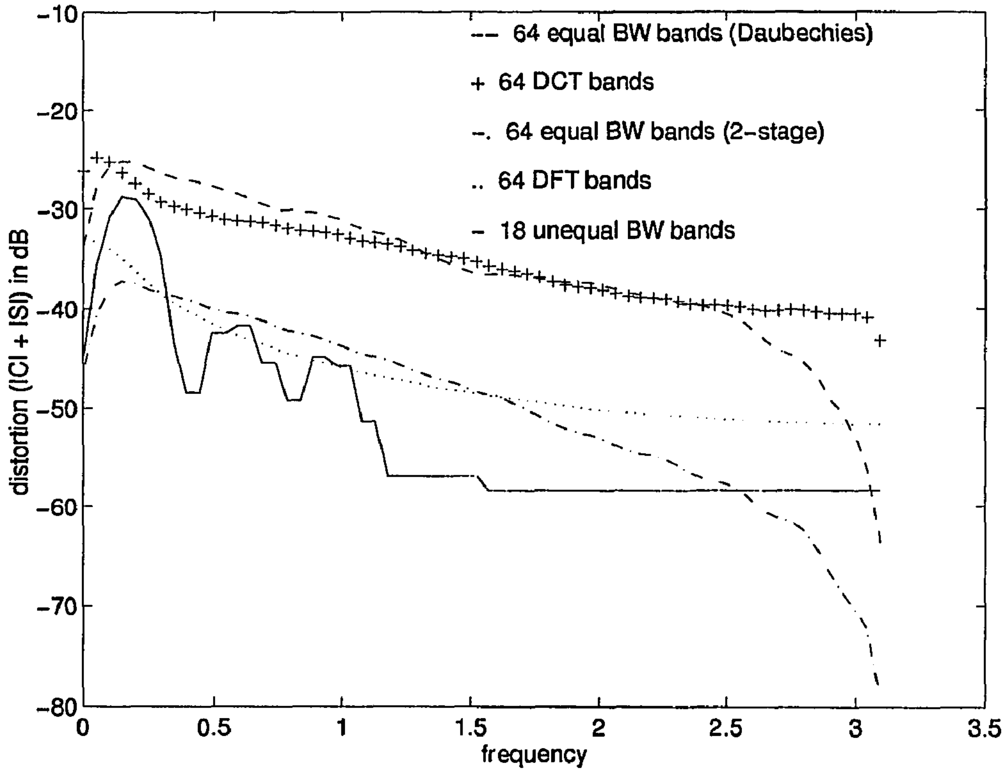

Figure 6.19 Distortion (ICI + ISI) for different family bases

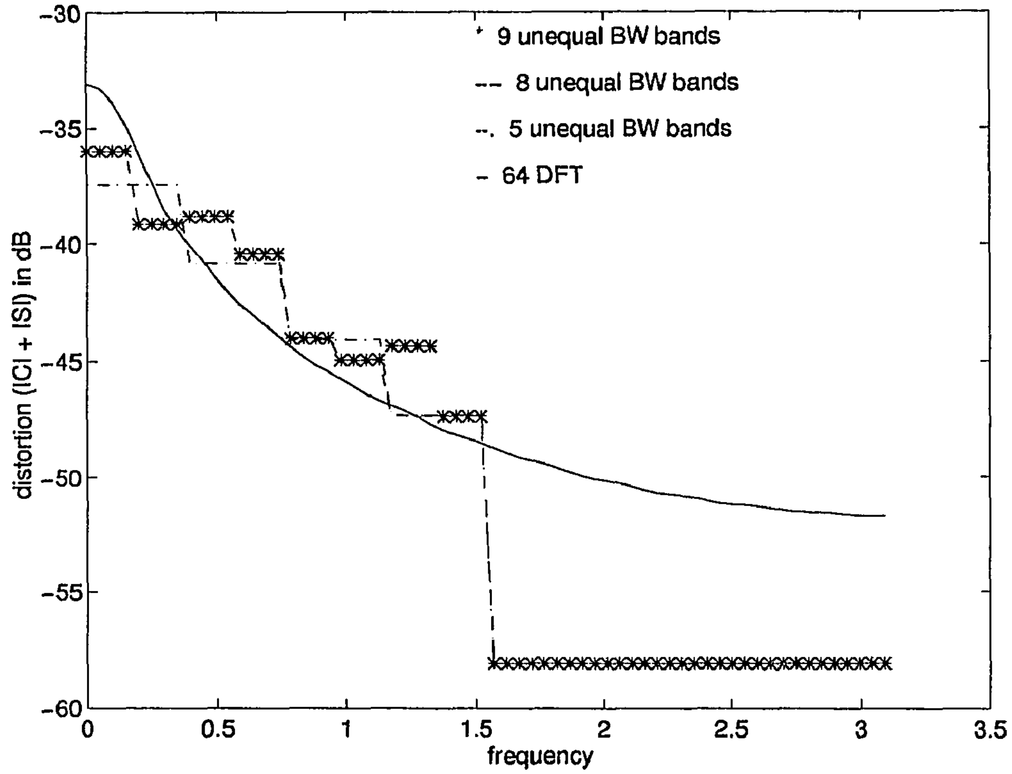

Figure 6.20 Distortion (ICI + ISI) for different unequal bandwidth splitting

unequal decomposition of the channel suffers the least from the aggregate ICI and ISI distortions. We also computed the distortions for different kinds of channel decompositions. Fig. 6.20 depicts the (ICI + ISI) distortions for several unequal bandwidth splitting of the channel. Furthermore, we included results for different DFT sizes in Fig. 6.21.

6.5.4 Discussions

Theoretically speaking, having more bands is better if the sub-channels are brickwall shaped. However, in practice, the sub-channels will have a finite roll-off due to the non-ideal basis functions. Therefore, significant interchannel interference or aliasing energy exists between sub-channels [2]. This fact naturally causes a performance degradation. The realization of DMT transceivers based on discrete-

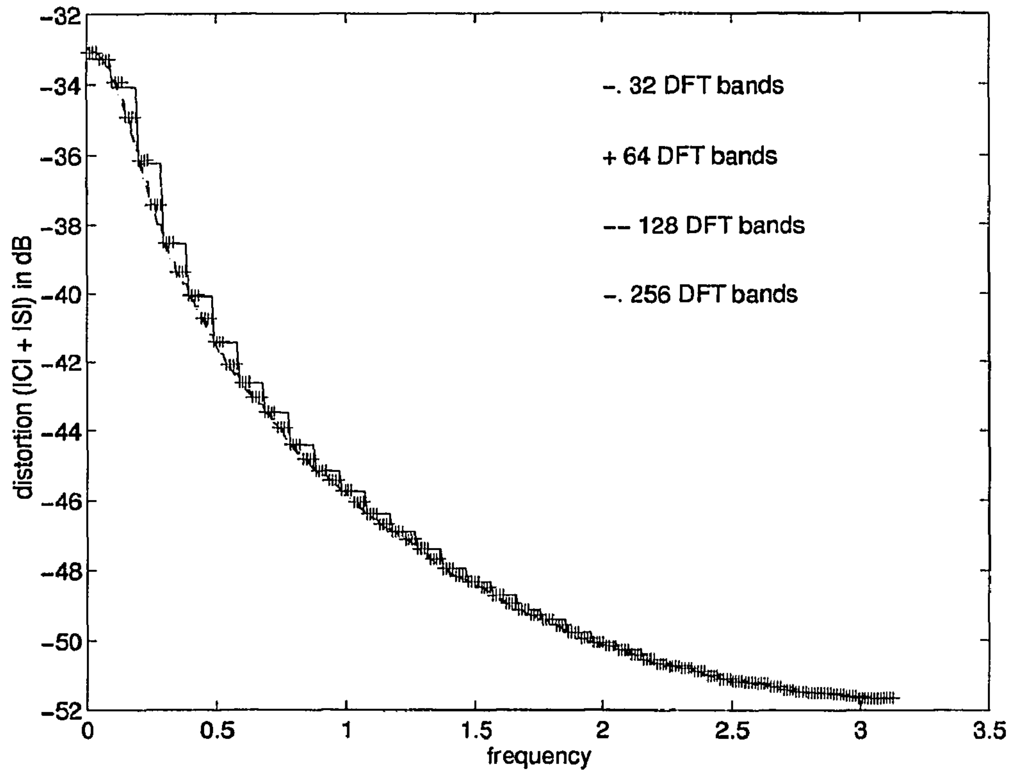

Figure 6.21 Distortion (ICI + ISI) for different DFT sizes

time subband/wavelet transform (DWT), a better alternate to the DFT based DMT, in order to alleviate the interchannel interference, was forwarded by Tzannes et. al.[39]. Nonetheless, the large number of sub-channels, namely 256 as suggested in the proposed standards, makes the aliasing or energy leakages from band to band quite large[2][37]. The proposed adaptive structuring of the channel offers the advantages of having orthogonal transform basis tailored to the unevenness of the channel. Therefore, a less number of sub-channels is necessary in order to get adequate performance. It is seen from Fig. 6.6 that the performance of the proposed sub-channel structuring algorithm is near optimal with significantly reduced system complexity over the existing techniques.

CHAPTER 7

CONTRIBUTIONS OF DISSERTATION AND FUTURE RESEARCH

The focus of this dissertation was on the theory, design and applications of the generalized linear transforms for information transmission. In particular, we showed the practical importance of time-frequency shaping of the transform bases. In order to achieve this goal, we extended the concept of classical uncertainty principle to its discrete-time counterpart by deriving a lower bound on the joint time-frequency spreads of functions. We showed that this bound is the same for both continuous and discrete-time functions if the latter have a certain degree of regularity. This bound can be lowered for the discrete-time case, if the regularity constraint is relaxed. Furthermore, we evaluated the trade-offs between localization in time and frequency for several proposed signal decomposition techniques. Block transforms have the best localization in time as expected since they have the shortest duration basis functions. On the other hand, they exhibit the worst localization in frequency domain as predicted by the uncertainty principle. In contrast, filter bank structures have sharper frequency responses. Therefore, their frequency spreads decrease at the expense of an increase in their time localizations. Since the filter banks can be utilized in two different types, direct and hierarchical, their time and frequency spreads can be monitored depending on the structure used. We found that direct structures offer the best time-frequency spread product followed by hierarchical ones with the fixed block transforms trailing at the end. We also evaluated the time and frequency spreads of a family of wavelet and scaling functions. Since the starting point of designing these analog functions is a two-band PR discrete-time filter bank, the time and frequency spreads of the generating filters should be monitored in such a way that a good time-frequency localized wavelet and scaling functions are obtained. In other words, a good time-frequency localized two-band PR discrete filter bank may not lead to a good time-frequency localized wavelet and scaling functions. This concept of optimally designing wavelet and scaling functions from a joint time and frequency localizations is an interesting topic for further research. As a design example of M-band perfect reconstruction filter banks, we proposed an efficient four-band linear phase PR multiplierless structure. This type of filters have great practical merits because of their computational efficiency.

The second main topic which we examined was that of subspectral modeling. We showed, both theoretically and experimentally, that subspectral modeling is superior to full spectrum modeling if performed before the rate change. The price paid for this performance improvement is an increase of computations. A few different signal sources were considered in this dissertation. It is shown that the performances of AR and ARMA techniques are comparable in subspectral modeling. The first is desired because of its simplicity. A coding algorithm of speech, namely CELP embedded in a filter bank structure, was also studied. We found that there were no improvements of subband CELP technique over the full band one. The theoretical reasonings of the experimental results were also given.

Our last contribution in this study was on the discrete multitone transceivers. We showed that the channel should not be divided into its sub-channels blindly. Rather, an intelligent, unequal bandwidth split should be performed for practical performance improvements. For this purpose, we proposed a smart algorithm for the decomposition of a channel into its sub-channels for the discrete multitone communications. This algorithm evaluates the unevenness and energy distribution of the channel spectrum in order to get an adaptive partitioning. We were able to achieve almost the same theoretical performance that is based on brickwall approximation of the channel by using this new splitting of the channel. Therefore, the best possible basis for the given channel response is used instead of using the same basis of DFT for any arbitrary channel. This adaptivity brings significant performance improvements. In fact, it was shown that an unequal bandwidth filter bank based DMT suffers much less from the combined interchannel and intersymbol interferences, as compared to the DFT based DMT. As a possible work continuation on this topic, we suggest a complete implementation of unequal bandwidth filter bank based DMT. Further assessments of the performance gain it brings as compared to the DFT based DMT in terms of BER are to be done.

APPENDIX A

Calculation of σ_ω for Gaussian

$$\sigma_\omega^2 = \frac{\frac{1}{2\pi}\int_{\pi}^{\pi}\omega^2|F(e^{j\omega})|^2 d\omega}{E} = \frac{K}{\pi}\int_0^{\pi}\omega^2 e^{-\omega^2/2\sigma^2}d\omega \tag{A.1}$$

Let $x = \omega/\sigma$ and integrate by parts to obtain

$$\begin{aligned}
\sigma_\omega^2 &= \frac{K\sigma^3}{\pi}\{[-xe^{-x^2/2}]_0^{\pi/\sigma} + \int_0^{\pi/\sigma} e^{-x^2/2}dx\} \\
&= \frac{K\sigma^3}{\pi}\sqrt{2\pi}erf(\pi/\sigma) - \frac{K\sigma^3}{\pi}(\pi/\sigma)e^{-\pi^2/2\sigma^2} \\
&= \sigma^2(1 - Ke^{-\pi^2/2\sigma^2}) = \sigma^2(1-\mu) \\
\sigma_\omega &= \sigma\sqrt{1-\mu} \qquad\qquad (A.2)
\end{aligned}$$

REFERENCES

1. A. N. Akansu, "Multiplierless suboptimal PR-QMF design," *Proc. SPIE*, vol. 1818, pp. 723–734, 1992.
2. A. N. Akansu and R. A. Haddad, *Multiresolution Signal Decomposition, Transforms, Subbands, Wavelets*, Academic Press, Inc., San Diego, California, 1992.
3. A. N. Akansu, R. A. Haddad, and H. Caglar, "The binomial qmf wavelet transform for multiresolution signal decomposition," *IEEE Transactions on Signal Processing*, vol. 41, pp. 13–19, January 1993.
4. A. N. Akansu and Y. Liu, "On signal decomposition techniques," *Optical Engineering*, vol. 30, pp. 912–920, July 1991.
5. A. N. Akansu and F. E. Wadas, "On lapped orthogonal transforms," *IEEE Transactions on Signal Processing*, vol. 40,no. 2, pp. 439–443, February 1992.
6. B. S. Atal, V. Cuperman, and A. Gersho, *Advances in Speech Coding*, Kluwer Academic Publishers, Boston, Massachussetts, 1991.
7. B. S. Atal and J. R. Remde, "Split-band APC system for low bit rate encoding of speech," *Proc. ICASSP*, pp. 599–602, 1981.
8. A. Benyassine and A. N. Akansu, "An evaluation of M-band orthonormal filter banks: Hierarchical and direct structures," *Proc. SPIE*, vol. 2094, pp. 1661–1670, 1993.
9. P. M. Cassereau, D. H. Staelin, and G. de Jager, "Encoding of images based on a lapped orthogonal transform," *IEEE Transactions on Communications*, vol. 37,no. 2, pp. 189–193, February 1989.
10. R. W. Chang, "High-speed multichannel data transmission with bandlimited orthogonal signals," *Bell Sys. Tech. J.*, vol. 45, pp. 1775–1796, December 1966.
11. J. S. Chow, J. C. Tu, and J. M. Cioffi, "A discrete mutitone transceiver system for HDSL applications," *IEEE Journal on Selected Areas In Communications*, vol. 9(46), pp. 895–908, August 1991.
12. J. M. Cioffi, "A multicarrier primer: A tutorial," November 1991.
13. L. Cohen, "Time-frequency distribution: a review," *Proc. IEEE*, vol. 77, pp. 941–981, 1989.

14. M. Copperi and D. Sereno, "9.6 kbit/s piecewise lpc residual excited coder using multiple-stage vector quantization," *Proc. ICASSP*, pp. 10.5.1–10.5.4, 1984.

15. I. Daubechies, "Orthonormal bases of compactly supported wavelets, variations on a theme," *Tech. Memo., AT&T Bell Labs*, 1989.

16. I. Daubechies, "The wavelet transform, time-frequency localization and signal analysis," *IEEE Trans. on Information Theory*, vol. 36, pp. 961–1005, September 1990.

17. I. Daubechies, "Orthonormal bases of compactly supported wavelets," *Communications in Pure and Applied Math*, vol. 41, pp. 909–996, 1991.

18. D. Gabor, "Theory of communication," *Journal of IEE*, vol. 93, pp. 429–457, 1946.

19. F. Itakura, "Line spectrum representation of linear predictive coefficients of speech signals," *J. Acoust. Soc. Am.*, vol. 57, S35(A), 1975.

20. N. S. Jayant and P. Noll, *Digital Coding of Waveforms*, Prentice Hall, Englewood Cliffs, New Jersey, 1984.

21. I. Kalet, "The multitone channel," *Proc. ICC*, pp. 1704–1710, 1987.

22. I. Kalet, "The multitone channel," *IEEE Transactions on Communications*, vol. 37, no. 2, pp. 119–124, February 1989.

23. S. Kay, *Modern Spectral estimation:Theory and Application*, Prentice Hall, Englewood Cliffs, New Jersey, 1988.

24. B. P. Lathi, *Modern Digital and Analog Communication Systems*, Holt, Rinehart, and Winston, Inc., Orlando, Florida, second ed., 1989.

25. E. Lee and D. Messerschmith, *Digital Communication*, Kluwer Academic Publishers, Boston, Massachussetts, 1989.

26. J. Makhoul, "Spectral linear prediction: Properties and applications," *IEEE Trans. on ASSP*, vol. 3, pp. 283–296, June 1975.

27. H. S. Malvar and D. H. Staelin, "The LOT: Transform coding without blocking effects," *IEEE Transactions on ASSP*, vol. 37,no. 4, pp. 553–559, April 1989.

28. F. Mintzer and B. Liu, "Aliasing error in the design of multirate filters," *IEEE Trans. on ASSP*, vol. 261, pp. 76–88, February 1978.

29. K. K. Paliwal and B. S. Atal, "Efficient vector quantization of LPC parameters at 24 bits/frame," *Proc. ICASSP*, 1991.

30. A. Papoulis, *Signal Analysis*, McGraw-Hill, New York, New York, 1977.

31. A. Peled and A. Ruiz, "Frequency domain transmission using reduced computational complexity algorithms," *Proc. ICASSP*, pp. 964–967, 1980.

32. S. Rao and W. A. Pearlman, "Analysis of linear prediction, coding and spectral estimation from subbands," *Preprint Submitted to IEEE Trans. on Information Theory.*

33. J. Roberts and R. Wiggins, "Piecewise linear predictive coding (PLPC)," *Proc. ICASSP*, pp. 470–473, 1976.

34. A. Ruiz, J. M. Cioffi, and S. Kasturia, "Discrete multiple tone modulation with coset coding for spectrally shaped channel," *IEEE Trans. on Communications*, vol. 40(6), pp. 1012–1029, June 1992.

35. M. J. T. Smith and T. P. Barnwell, "Exact reconstruction techniques for tree-structured subband coders," *IEEE Transactions on ASSP*, vol. 34, pp. 434–441, 1986.

36. F. K. Soong and B. H. Juang, "Line spectrum pair (LSP) and speech data compression," *Proc. ICASSP*, vol. 57, S35(A), pp. 1.10.1–1.10.4, 1984.

37. M. V. Tazebay and A. N. Akansu, "Adaptive subband transforms in time-frequency excisers for DSSS communications systems," *Preprint, Submitted to IEEE Transactions on Signal Processing*, 1994.

38. M. V. Tazebay, A. Benyassine, and A. N. Akansu, "Time-frequency localization in subband trees and progressive optimality," *Preprint, Submitted to IEEE Transactions on Signal Processing*, 1994.

39. M. Tzannes, M. Tzannes, and H. L. Resnikoff, "The DWMT: A multicarrier transceiver for ADSL using M-band wavelet transforms," *In ANSI T1E1.4 Committee Contribution*, March 1993.

40. P. P. Vaidyanathan, *Multirate Systems and Filter Banks*, Prentice Hall, Englewood Cliffs, New Jersey, 1993.